Department of Chemical Engineering

Modelling micro-scale coalescence and transport processes in liquid aerosol filtration

Ryan Mead-Hunter

This thesis is presented for the Degree of
Doctor of Philosophy
of
Curtin University

January 2012

Declaration

To the best of my knowledge and belief this thesis contains no material previously published by any other person except where due acknowledgement has been made.

This thesis contains no material which has been accepted for the award of any other degree or diploma in any university.

January 2012

Abstract

One of the methods most commonly applied to treat liquid aerosols is fibrous filtration. However, despite the prevalence of fibrous filter technology in industry, their behaviour is not yet fully understood and therefore much of the design and development work is based, by necessity, on trial and error type approaches. The reason for this lack of knowledge is primarily due to the nature of the material collected by the filter. In contrast to dust filtration, where solid particles are collected and adhere to the fibre, mist filters must contend with liquid droplets. These droplets by their very nature are able to spread over the fibre surface, merge with other droplets, coalesce into larger droplets, form pools within the filter and liquid bridges spanning multiple fibres, and ultimately drain from the filter itself. Thus the mechanisms controlling their behaviour are quite complex.

The majority of the studies pertaining to modelling mist filter behaviour have focussed on using empirically derived expressions to predict macro-scale filter properties, such as pressure drop and saturation. While usually effective when applied to the filters and operating conditions on which they were derived, these models tend not to work as well when applied to filters and liquids with different properties. Given that fibrous filters generally consist of a loosely packed, (near) random array of fibres, it is perhaps better to consider the behaviour at a smaller scale. Fibrous filters are known to exhibit behaviour similar to that of a series of capillaries and so were examined in terms of a system theoretical capillaries. Fibrous filters were also examined (in detail) at a smaller, more fundamental scale - that of a single fibre.

It has been found that, with a suitable calibration of the pressure drop, the equilibrium saturation of a filter can be determined using a capillary based model. In this model, a theoretical capillary was considered, and the equilibrium capillary rise height determined using a modification of the Washburn equation. The equilibrium saturation was then calculated as the portion of the filter geometry that falls below the level of the capillary rise height. The model was found to work well for glass-fibre filters using a variety of oils and flow velocities and is also applicable to stainless steel filter media. This model however is likely limited to filters with a thickness of less than 5mm.

The use of a capillary-based model however was found to only permit the direct determination of the equilibrium saturation. While for properties such as filtration efficiency, such coupled models were found likely to be inaccurate. Therefore, for more fundamental understanding of mist filter behaviour,

droplets on a single fibre were considered. This allowed the force required to move a coalesced liquid droplet along a fibre to be measured and the behaviour of the coalesced droplets to be observed. In order to quantify these parameters accurately it was necessary to develop a methodology using the atomic force microscope (AFM).

A theoretical model has been developed to allow the force required to move a coalesced liquid droplet from its stationary (stable) position on a fibre to be predicted. This model has been validated using a series of AFM measurements where different oils, fibre materials and fibre diameters were considered. The modelled and experimental data agree well with each other, though the surface roughness of the fibre was found to influence the force. While the model itself was developed for axisymmetric droplets, it was also found to work well for droplets which were displaced from the axisymmetric (rest) position. It was found, both theoretically and experimentally, that the force required to move a droplet decreases as the droplet displacement increases. This droplet displacement has been observed in filters as an effect of flow velocity. Demonstrating that the onset of drainage in mist filters may be influenced by filter face velocity, with droplets draining earlier when the velocity is higher.

It has also been found that, with a suitable modification, the theoretical model can be applied with some success to 'clamshell' shaped droplets (i.e. axially asymmetric droplets). This is however limited by the formulation of the original model and also the nature of the fibres. Oleophobic fibres were prepared by coating the fibre, which left the surfaces very rough. It has been found that much of the variation in the measured forces is due to the inhomogeneities in the fibre surfaces. It was found though, that the measured forces could be predicted well using a Bayesian regression model.

The force required to move a coalesced liquid droplet is therefore dependent on the properties of the oil and on the nature of the fibre surface. In general, the force required to move a droplet on an oleophillic fibre appears to be greater than that to move a droplet on an oleophobic fibre. However, the effects of the surface roughness may potentially act to reduce this difference. In fact some of the results imply that if the effects of contact line pinning are strong enough, it may negate this difference all together. So while as a general rule, oil may be drained more easily from oleophobic fibres than oleophillic ones, there will be cases where this may not be true.

The influence of particulate matter, such as soot, was also considered. It

was found that, at soot concentrations likely to be encountered in internal combustion engines that, the soot had very little effect on the force required to move an oil droplet along a fibre.

The force measurements have also provided important validation data, to aid the development of a computational fluid dynamics (CFD) solver for mist filters (or more generally droplet-fibre systems). The development of this solver has been described and validation tests run to determine how well the solver can model, droplet capture, the break-up of a liquid film under Plateau-Rayleigh instability and the movement of coalesced droplets. The break-up of the liquid film has been shown to be physically realistic and the solver does not allow unrealistically thick films to exist. Additionally, the force required to move a liquid droplet agrees well with the values predicted by the theoretical model. There still remains some mesh dependency issues pertaining to the capture of droplets, but these do not have an adverse effect on the performance of the solver on the simulation of a fibrous filter.

Ultimately, it has been found that it is possible to simulate the behaviour of a fibrous filter, capturing liquid aerosols, using CFD. The CFD solver has been validated using both existing theory and the data obtained during the AFM measurements. These measurements also revealed information about the behaviour of droplet-fibre systems and resulted in a model that can be used to predict the force required to move a liquid droplet along a fibre.

In summary, this work has:

- Conducted extensive full-scale mist filtration experiments, primarily to measure saturation, pressure drop and face velocity.
- Developed a capillary model for predicting filter saturation.
- Developed a method for droplet-fibre force measurements using the atomic force microscope.
- Conducted extensive single fibre droplet force measurements on both oleophillic and oleophobic systems using a range of fibre diameters, materials, oils and contaminants.
- Developed theoretical and statistical models for droplet-fibre forces.
- Developed a computational fluid dynamics solver to simulate droplet-fibre capture processes on the micro and macro scale.

Therefore, there can be no doubt that this work has provided a significant and novel contribution to the fields of interfacial science and gas-liquid separation.

Acknowledgements

Firstly, I would like to thank my principal supervisor, Associate Professor Ben Mullins, for his help and guidance in the completion of this thesis. The many meetings and conversations where we discussed modelling, further experiments and filtration theory (even those involving the phrase "You know what would be really good....") where invaluable in terms of the completion of this work.

Secondly, I would like to thank my co-supervisors, Dr Thomas Becker and Dr Andrew King, for their help with the experiments and simulations. Dr Becker was instrumental in training me to use the atomic force microscope, in the development of the methodology used in this thesis, and in the interpretation of the results. The section on computational fluid dynamics would not have been possible without the help of Dr King, who was of frequent help in running the simulations and sorting out all the issues associated with the solvers and with OpenFOAM itself.

I would also like to thank Emeritus Professor Roger Braddock for his help with the theoretical models and Dr Rebecca O'Leary for her help with the Bayesian regression models. Additionally, I would like to thank the Diplomarbeit (Tanja Bergen) and Studeinarbeit (Nina Merkel, Sara Schairer and Georg Ladenberger) students who were involved in various parts of the project.

The funding received from the Australian Research Council (ARC Linkage Grant LP0883877) and MANN+HUMMEL Gmbh is gratefully acknowledged.

Finally, I would like to thank Monica for her love and support through out the completion of this work.

Publications Arising from this Work

This thesis contains the following works:

Mead-Hunter, R., King, A.J.C., and Mullins, B.J. (2012) *Plateau-Rayleigh Instability Simulation*, Langmuir **28**(17), 6731-6735

Mead-Hunter, R., Bergen, T., Becker, T., O'Leary, R.A., Kasper, G. and Mullins, B.J. (2012) *Sliding/Rolling Phobic Droplets along a Fiber: Measurements of Interfacial Forces*, Langmuir **28**(7), 3483-3488

Mead-Hunter, R., Mullins, B.J., Becker, T. and Braddock, R.D. (2011) *Evaluation of the Force Required to Move a Coalesced Liquid Droplet along a Fiber*, Langmuir **27**(1), 227-232

Mead-Hunter, R., Mullins, B.J., Merkel, N., Braddock, R.D., Kampa, D. and Kasper, G. (2011) *The relationship between pressure drop and liquid saturation in oil-mist filters - predicting liquid saturation using a capillary-based model*, Separation and Purification Technology **Submitted**

Mead-Hunter, R., Bredin, A., King, A.J.C., Larcher, A.V., Becker, T. and Mullins, B.J. (2012) *The influence of soot nanoparticles on the micro/macro-scale behaviour of coalescing filters*, Chemical Engineering Science **Submitted**

Mead-Hunter, R., Becker, T., King, A.J.C., Braddock, R.D. and Mullins, B.J. (2012) *Spiders Pulling Droplets: droplet sliding forces on spider silk and other fibres*, Nature **Submitted**

Mead-Hunter, R., Mullins, B.J. and King, A.J.C. (2011) *Development and Validation of a Computational Fluid Dynamics (CFD) Solver for Droplet-Fibre Systems* MODSIM, Perth, WA, Australia

Mullins, B.J., Mead-Hunter, R., Merkel, N., Braddock, R.D., Kampa, D. and Kasper, G. (2009) *Modelling liquid saturation in filters collecting liquid aerosols*, 18th World IMACS/MODSIM, Cairns, Australia, 2009

Mead-Hunter, R., King, A.J.C. and Mullins, B.J. *Computational Fluid Dynamics (CFD) simulation of coalescing filters*, Journal of Aerosol Science, **In-Prep**

Contents

List of Figures

List of Tables

Nomenclature

α	packing density (solidity)
α_θ	half the angle between cantilever arms
α_ϕ	relaxation factor
α_l	fluid volume fraction
α_{tube}	limit liquid packing density
α_{wet}	wet fibre packing density
β	angle of the fibre to the horizontal
$\Gamma_i(\omega_f)$	imaginary component of the hydrodynamic function
γ	surface energy
ΔP	pressure drop
ΔP_E	equivalent pressure drop
ΔP_l	Laplace excess pressure
ΔP_s	"pseudo"-steady state pressure drop
ΔP_0	pressure drop across a clean filter
Δt	time-step
Δx	length interval
ϵ	lateral in-plane bending
ϵ_f	relative permittivity of the fibre
ϵ_p	porosity
ϵ_0	relative permittivity of a vacuum
η_D	single fibre efficiency due to diffusion
η_{DR}	single fibre efficiency due to the combined effects of interception and diffusion
η_F	total single fibre efficiency

η_G	single fibre efficiency due to gravitational settling
η_I	single fibre efficiency due to impaction
η_R	single fibre efficiency due to interception
η_T	total filter efficiency
η_q	single fibre efficiency due to electrostatic attraction
θ	contact angle
θ_e	equilibrium contact angle
θ_i	inflection angle
θ_r	arc angle
λ	mean free path
μ	viscosity
μ_g	gas viscosity
ν	kinematic viscosity
ξ	ratio of pressure drops
ρ	density
ρ_g	gas density
ρ_p	particle density
ρ_r	residual term
ρ_s	sphere density
σ	interfacial (surface) tension
σ_{LV}	liquid-vapour interfacial tension
σ_{SL}	solid-liquid interfacial tension
σ_{SV}	solid-vapour interfacial tension
τ	simplification term
τ_a	advancing line tension

τ_r	receding line tension
υ	Poisson ratio
υ_f	resonance frequency
ϕ	solution
ϕ^n	under-relaxed solution
ϕ^{new}	solution obtained from the algorithm
ϕ_x	angle of the fibre from the x axis
ψ	angular position of the contact line around the fibre
Ω	filtration surface area
ω	equivalency factor
ω_f	resonance frequency
ω_t	radial resonance frequency of a cantilever
A	a filter geometry dependent constant
A_c	cross-sectional area of a capillary
A_f	filter area
a	simplification term
a_i	modified value of a
Bo	Bond number
b_c	cantilever width
b_l	width of a single cantilever arm
C	length of the wetted perimeter
C_D	drag coefficient
Ca	Capillary number
C_c	Cunningham correction factor
C_d	diffusional efficiency correction factor

C'_d	diffusional efficiency correction factor
C_r	interception efficiency correction factor
c	Courant number
c_f	correction to capillary radius
D_p	droplet diffusion coefficient
Dr	Drainage rate term
d	distance from the tip centre to the end of the cantilever
d_d	droplet diameter
d_f	fibre diameter
d_{fwet}	wet fibre diameter
dZ	thickness of the filter layer, j, in flow direction
E	Young's modulus
F_b	boundary forces
F_d	drag force
F_k	thermal diffusive force
F_l	force per wetted length
F_m	force required to move a droplet
F_r	restoring force
F_t	force acting on the cantilever
f	proportion of the fibre surface not covered by liquid
f_x	fibre replicate, where x may take a value from a to v
G_s	gravitational settling term
G	centre of mass
$\boldsymbol{G}$	vector with Gaussian random number components
g	acceleration due to gravity

h	length of the moment arm
h_c	height
h_r	fibre radius
h_t	film thickness
J_s	mass moment of inertia
j	designates a theoretical layer within a filter
Kn	Knudsen number
K_1	a constant
Ku	Kuwabara hydrodynamic factor
k	permeability constant
k_ϕ	torsional spring constant
k_B	Boltzmann constant
k_n	normal spring constant
k_s	spring constant
k_{yT}	torsional stiffness
$\overline{L}$	reduced wetted length
L_c	cantilever length
L_f	length of the fibre
l	wetted length
l_t	tip length
M	added mass
M^*	effective mass of a cantilever
m_b	mass of a beam
m_{liq}	collected liquid mass
N	number of peaks

N_l	number of layers of filter media
N_R	ratio of droplet diameter to fibre diameter
n	number of iterations
n_d	reduced droplet diameter
n_r	reduced radius
Pe	Peclet number
P_0	pressure acting on the liquid within the capillary
P_a	pressure acting on the liquid surface
P_e	filter penetration
Q	volumetric flow rate
Q_f	quality factor
Q_t	quality factor of the torsional vibration
q	the charge on a particle
Re	Reynolds number
R_1, R_2	principle radii of curvature
R_q	root mean square roughness
r	droplet displacement distance
r_c	capillary radius
r_f	fibre radius
S	filter saturation ratio
S_α	phase fraction source term
S_e	saturation
S_{Fe}	equilibrium filter saturation
S_m	momentum source term
S_{Mx}, S_{My}, S_{Mz}	momentum sources in the x, y and z directions

$S_{ni,j}$	spectral intensity
S_p	spreading coefficient
S_t	Stokes number
s_{lat}	lateral signal sensitivity
T	temperature
Ts	total signal
t	time
t_c	cantilever thickness
U_r	compression velocity
U_0	filtration velocity
u	velocity
u'	interstitial velocity (in a filter)
u_p	velocity of a particle
u_t	tip velocity
u_0	gas velocity at the filter face
$\overline{V}$	reduced volume
V_{cell}	volume of a cell
V_{cs}	volume of a slice through a cylinder
V_{oil}	volume of oil
V_{void}	volume of void space
v_0	superficial fluid velocity
W	width of the test filter
w	width of the cantilever arm at the midpoint
X_E	distance the spring has moved from its equilibrium position

x	height of liquid in the x direction, also an axis in the Cartesian coordinate system
x_∞	equilibrium capillary rise height ($t = \infty$)
x_a	distance from the axisymmetrical rest position to the droplet mass centre
x_b	height of the capillary that is immersed
x_d	distance between centroids of two droplets
x_2	droplet radius
Z	filter thickness
z_A	z component of the position vector r_a
z_i	peak height
$(1 - \epsilon_p)$	void space or packing density
$(\bigtriangledown \bullet \rho v)$	mass flux divergence
$[\bigtriangledown \bullet \tau]$	viscous force
$\bigtriangledown p$	pressure force

1 Introduction

The term aerosol is used to describe a kind of colloid, where the dispersion medium is a gas and the dispersed phase consists of solid or liquid "particles". A liquid aerosol is then, an aerosol consisting of liquid droplets suspended in a gas; examples of which include fogs and mists. Industrially, such mists are commonly generated by manufacturing and automotive industries, e.g oil mists (i.e. liquid aerosols where oil is the liquid) are relatively common, and need to be treated to prevent ill effects to people, the environment and quite often the process itself.

Oil-mists typically consist of a broad, poly-disperse distribution of fine liquid droplets in a gas; often air. They are generated in many different processes, generally as the result of frictional or shear forces, though also via evaporation-condensation processes. Common examples are engine crank cases, air-compressors and gas cleaning operations.

The health impacts of oil-mists are numerous and well documented, with exposure limits of $5\text{mg}/m^3$ imposed in Australia and numerous other countries (Pohanish, 2002). The short term effects include irritation of the eyes, nose and throat, headaches, nausea and pneumonia. Long term exposure can lead to further effects, including, chronic bronchitis, pulmonary fibrosis and significant dermatological conditions (Pohanish, 2002). A key reason for the health impacts of oil-mists is due to the very small size (typically less than 2.5 μm diameter) of the oil droplets they contain. These particles are small enough to penetrate deep within the lung tissue and may not be exhaled.

In metal cutting processes, metal working fluids are used to draw heat away from the surface of the metal and the cutting tool, and to wash away metal shards and debris (Gunter and Sutherland, 1999). In these operations, it is common for metal working fluids to be aerosolised (Thornburg and Leith, 2000), this forms a mist which is typically drawn into an extraction line/fume hood and is then removed from the building. However in cold climates, fac-

tories typically recirculate the air in an effort to reduce heating costs. The drawback here is that the workers in such a factory will be exposed to an ever increasing concentration of oil-mist and the many associated detrimental health effects. The extracted air then needs to be treated to remove the oil (metalworking fluid) droplets, before it can be recirculated through the heating system.

The lubricating oil in internal combustion engines may be aerosolised by the movement of the pistons, these mists may then be drawn out in the crankcase exhaust. This is a significant issue in turbo-charged diesel engines, where crankcase gases are re-circulated in order to reduce VOC emissions. The recirculated gases will contain an oil-mist and if untreated, oil will be fed back through the air intake into the turbo-charger. This has the potential to induce accelerated wear in the turbocharger, which may be expensive and time consuming to replace, particularly if the vehicle is in use in a remote area (e.g. mine sites, long haul truck routes). Thus the crankcase gases must be treated to remove the aerosolised oil, which may then be returned the the oil sump.

In natural gas fields, the extracted gas may contain oil droplets/oil-mists, the presence of which can have significant and detrimental effects on both transmission pipelines and compressors (Li et al., 2009). This is an important issue as the centrifugal compressors used in natural gas fields, would be costly to replace (especially once the costs of lost production are considered).

It is therefore critical that oil-mists be treated to prevent harm to the environment, processes, equipment and peoples health. There are a number of technologies available to remove oil particles from gas streams. These include cyclones, scrubbers, membranes and fibrous filters. However, given the small sizes of the oil droplets in mists and the high separation efficiencies required, fibrous filters are often the best option (Agranovski and Whitcombe, 2001).

Understandably then, the most common method used in the treatment of

oil-mists is fibrous filtration; with filters of various shapes, sizes and properties being employed to capture and separate the oil from the gas is vitally important. This serves the purpose of cleaning the gas, so that it is safe to release into the environment, or to be returned to the process. Additionally, the collected oil may be recovered for reuse or disposal. Given the finite nature of oil resources, the ability to remove oil from the gas, oil-mist filtration not only serves the requirement to clean the gas but also aids in the conservation of the oil.

However, despite the prevalence of gas-oil separators in industry, relatively little is known about the mechanisms governing the behaviour of fibrous filters collecting oil-mists. The majority of work on fibrous filters thus far has focussed on dust filtration. The ability of oil to coalesce into larger droplets and liquid pools and its ability to subsequently move around within the filter under the influence of air flow and gravity, make describing the behaviour of oil-mist filters difficult; with most of the design and development work based on a trial and error approach. If the mechanisms in place can be better understood and the behaviour modelled however, steps could then be taken towards optimising the design of fibrous filters used in the treatment of oil-mists.

The filtration of oil-mists can then be seen to be important to the process, automotive and manufacturing industries, as well as being an important tool in environmental protection and public health.

This work will explore the micro-scale processes of coalescence and liquid transport that take place within these filters.

This work aims to provide a significant contribution to the advancement of fundamental and theoretical knowledge of mist filtration. It is hoped that this work will ultimately lead to the development of improved tools for the design and optimisation of such filter systems.

2 Background and Literature Review

Filtration is one of the most common separation techniques employed in chemical/process engineering. Whether it be to separate solids from a liquid or gas or to separate a liquid from a gas, or even a liquid from a liquid, all filtration involves the use of some form of medium that is permeable to certain components of a mixture. When it comes to gas filtration, which accounts for approximately 16% of all filtration investment (Sutherland, 2008), fibrous filter media are commonly used.

The term aerosol filtration refers to gas filtration where the component captured by the filter is the media dispersed within the gas. Liquid aerosol filtration then refers to the filtration of an aerosol consisting of a dispersed phase made up of liquid droplets. Liquid aerosol filters are also referred to as mist filters or coalescing filters.

2.1 Aerosol Filtration

Fibrous filters are filters that are made up of fine fibres that are arranged in such a way that the majority of the fibres are perpendicular to the direction of the air flow (Hinds, 1999). These filters may be made from glass, cellulose, stainless steel or plastic (polymer) fibres and generally operate at relatively low air velocities (Hinds, 1999). A typical fibrous filter is shown in Figure 2.1. It is important to remember that the traditional idea of a filter working as a microscopic sieve, as in the case of filtering solid particles from a liquid, does not apply to aerosol filtration (Hinds, 1999) or indeed most filtration operations.

As oil mist droplets are captured by the filter fibres, they begin to coalesce and form larger droplets on the fibres. The collected droplets act to impede the flow of air, leading to an increase in pressure drop through the filter and a drop in overall efficiency (the number of particles collected divided by the number of particles entering) (Letts et al., 2003). This effect is in complete contrast to filters collecting solid dust (Agranovski and Shapiro,

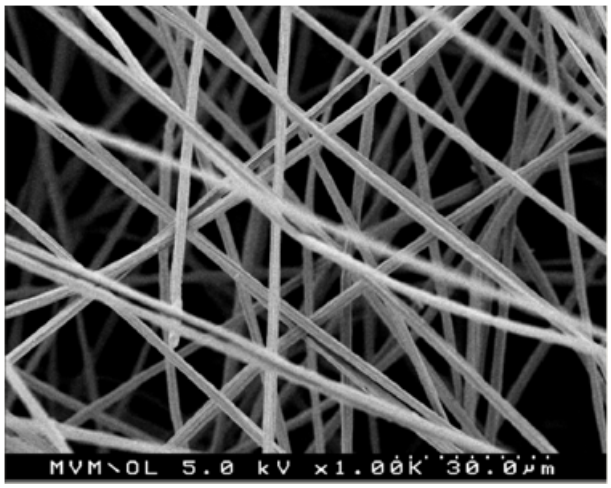

Figure 2.1: A Scanning Electron Microscope (SEM) image of a fibrous filter (Courtesy of KIT (Germany) MVM Particle Measurement Laboratory)

2001), which increase in efficiency during loading, as the collected particulate matter is highly porous and therefore improves filtration efficiency. This is because in dust filtration the majority of dust collection occurs at the filter face and the collected dust particles are able to aid in the collection of further dust particles. Liquid droplets, on the other hand, are obviously non-porous, and therefore can be said to behave like large diameter filter fibres; as generally, filtration efficiency decreases with increased fibre diameter.

After a sufficiently long period of operation, the coalesced droplets will become quite large (in relation to the diameter of the fibres) and will reside predominantly at fibre intersections or along the lengths of the fibres (Raynor and Leith, 2000). These droplets will continue to increase in size until the gravitational force exceeds the adhesive/frictional forces and the droplets move down the fibres, wetting other fibres in the process (Contal et al., 2004). Many of the accumulated droplets will drain down the filter in this way, while some will be retained on the fibres, and others may be re-introduced into the passing air stream (Agranovski and Braddock, 1998b; Agranovski et al., 2002; Letts et al., 2003).

Mist filters will entrain oil during the early stages of operation (Raynor and Leith, 2000). At this point there is no effective model with which to characterise their behaviour. It is known from observation that (generally) there will be an increase in pressure drop and a decrease in efficiency during loading and that this will be followed by the establishment of a "pseudo"-steady state, where the efficiency and pressure drop will cease to change with time (Contal et al., 2004). This is significant as in industry these filters will spend upwards of 99% of their operating life in this entrained/saturated condition. A full description of filter theory is presented in the following sections.

The observed reduction in the efficiency of mist filters may be caused by the increased (interstitial) air velocity through the filter; which occurs as liquid is being accumulated. This subsequently induces a decrease in the capture of small droplets by Brownian diffusion (Raynor and Leith, 2000). Given that diffusion is the most significant form of transport of particles with a diameter of less than 0.1μm through a gas (Hinds, 1999), it seems reasonable that an increase in velocity through the filter would reduce the effects of diffusion. Though, conversely, this increase in interstitial velocity may increase the capture of droplets via impaction.

The issues of reduced efficiency and increased pressure drop exist as there is a significant difference in the initial rate at which a filter will become oil-entrained and the rate at which the collected droplets will drain from the fibres. In fact, drainage does not commence until a certain level of saturation occurs. This represents the establishment of the "pseudo"- steady state; where drainage will commence, and the rate of drainage will (typically) be the same as the rate of entrainment. At this point and beyond, the saturation of the filter will remain constant, provided the operating conditions (liquid aerosol concentration, flow velocity, temperature) are unchanged. This is the "steady-state" saturation and will result in a regime where fluid will be retained indefinitely within the filter (Raynor and Leith, 2000).

The "steady-state" or equilibrium saturation, is defined as the volume of void space in the filter occupied by collected oil, such that,

$$S_e = \frac{V_{oil}}{V_{void}}, \tag{2.1}$$

where, $V_{void} = (1 - \alpha)$ and α is the filter packing density or 'solidity'.

Liquids collected by fibrous filters may also be subject to evaporation. The droplets collected on filter fibres can saturate the passing air stream with vapour from the collected oil (Cooper and Leith, 1998). Evaporation of accumulated oil from the filter is dependent on the concentration of vapour in the air stream entering the filter and on the volatility (vapour pressure) of the liquid components (Raynor and Leith, 2000).

Furthermore, it is seen that oil droplets can be forced through the filter, resulting in droplets forming on the "clean" gas side of the filter. This can result in oil becoming re-entrained in the air stream from the rear of the filter (Raynor and Leith, 2000).

It has been observed that re-entrainment of oil droplets into the air stream presents a considerable problem in high efficiency filters used industry (Mullins et al., 2006). This is a problem as larger droplets $>1000\mu$m, will have a mass equivalent to many small droplets ($<1.0\mu$m) the typical order of particle size which the filter is collecting. Re-entrainment of large droplets appears to be directly proportional to filter saturation and face velocity.

The clogging (i.e. the saturation of the filter by collection of aerosol droplets) behaviour of mist filters during aerosol loading may be separated into a number of stages (Contal et al., 2004; Frising et al., 2005; Charvet et al., 2008; Charvet et al., 2010).

Contal et al. (2004) described the clogging behaviour of fibrous filters by

liquid droplets in four stages, while Charvet et al. (2010) use three stages.

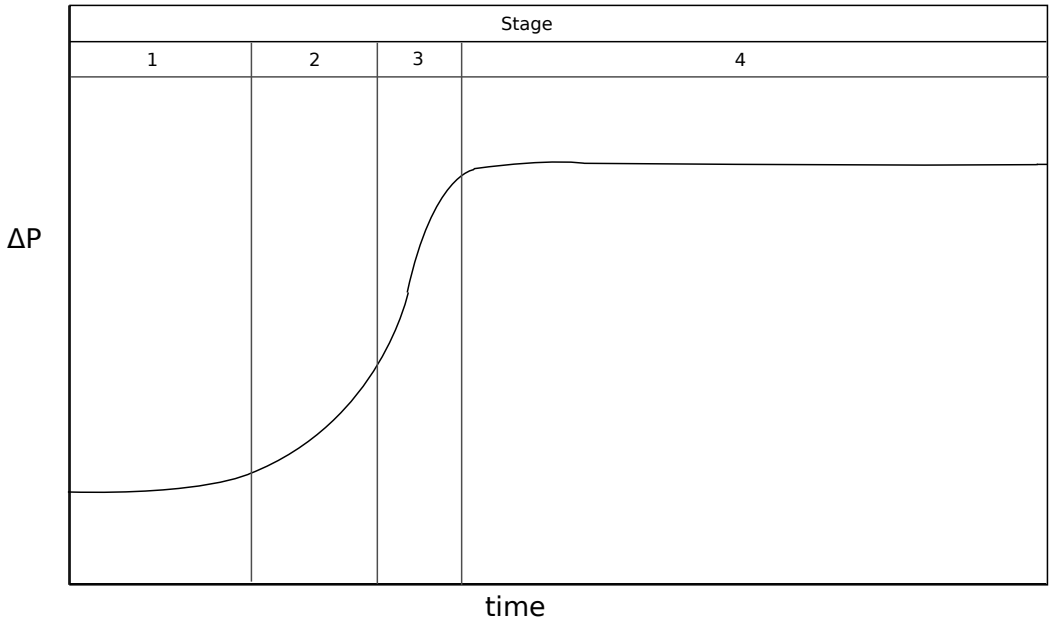

Figure 2.2: Pressure profile of a typical mist filter

Stage 1: Droplets are deposited around the fibres, supposedly leading to an increase in the 'friction' area; which in turn causes a rise in the pressure drop (Contal et al., 2004). The collection of droplets also leads to a decrease in fibre collection area and therefore an increase in filter penetration (Contal et al., 2004). This corresponds to the beginning of the pressure drop profile as given in Figure 2.2, where the gradient is small. Charvet et al. (2010) consider this stage (also their Stage 1) as 'static' filtration, as it is assumed that the collected oil is stationary within the filter.

Stage 2: During this stage there is a change in the evolution of the pressure drop. In this stage filter penetration increases exponentially. Contal et al. (2004) attribute these effects to both a reduction in the specific area and the collection area caused by droplets coalescing and the re-distribution of collected liquid within the filter. This can also be seen in Figure 2.2.

Stage 3: Pressure drop in this stage increases exponentially due to an increase in flow resistance. This increased flow resistance leads to an increase in interstitial velocity, which in turn has the effect of reducing penetration (of larger particles) (Contal et al., 2004). This is due to the increased capture of droplets by impaction (Contal et al., 2004). This is shown on Figure 2.2, also; though it should be noted, that unless filter penetration (or efficiency) is continuously measured the distinction between stages 2 and 3 is only arbitrary. Charvet et al. (2010) consider Stage 2 and 3 as given by Contal et al. (2004) to be their Stage 2 and term this 'dynamic' filtration, as the collected oil is presumed not to be stationary within the filter and may coalesce into droplets and form liquid bridges and pools.

Stage 4: This stage represents the end of the clogging period and liquid bridges and films form through the full thickness of the filter (Contal et al., 2004). This stage is characterised by the establishment of a"pseudo"-steady state where drainage and collection rates appear to be the same and the filter efficiency and pressure drop remain constant. This stage corresponds the part of the pressure drop profile has a zero gradient. Charvet et al. (2010) consider the establishment of the "pseudo"-steady state as their Stage 3.

2.2 Fluid Flow through Filters

The flow through filters may be modelled by using the equations of motion and continuity. The equations are derived from mass and momentum balances performed over a unit volume of fluid. The continuity equation (Equation 2.2) and the momentum equation (Equation 2.3) expressed in vector notation are given as,

$$\frac{\delta\rho}{\delta t} = -(\bigtriangledown \bullet \rho v), \tag{2.2}$$

where ρ is the density of the fluid, t is time, v is the velocity vector and $(\bigtriangledown \bullet \rho v)$ is the vector operator indicating mass flux divergence and,

$$\rho\frac{Dv}{Dt} = - \bigtriangledown p - [\bigtriangledown \bullet \tau] + \rho g, \tag{2.3}$$

where $\bigtriangledown p$ is the pressure force acting on the element, $[\bigtriangledown \bullet \tau]$ is the viscous force acting on the element and g is the acceleration due to gravity.

In the case of constant viscosity and density (this may be assumed when dealing with filtration) Equation 2.3 may be expressed as,

$$\rho\frac{Dv}{Dt} = - \bigtriangledown p - [\mu \bigtriangledown^2 \bullet v] + \rho g. \tag{2.4}$$

Equations 2.2 and 2.4 are the Navier-Stokes equation (Bird et al., 2007), which are fundamental to filtration theory. This will be discussed further in Section 2.8.

Flow through porous media may be described through the use of channel theory and cell model theory. Channel theory includes Darcy's law and the Kozeny-Carmen equation and cell model theory covers the Davies equation, the Kuwabara model and drag model theory.

When considering flow through porous media, the equations of continuity and motion may be changed to reflect the fact that the unit volume of fluid now exists within a porous space. Such that,

$$\epsilon_p \frac{\delta \rho}{\delta t} = -(\bigtriangledown \bullet \rho v_0), \tag{2.5}$$

$$v_0 = \frac{k}{\mu} \bigtriangledown p = \rho g, \tag{2.6}$$

where ϵ_p is the porosity of the media, v_0 is the superficial fluid velocity through the media, μ is the viscosity of the fluid and k is the permeability constant.

Equation 2.5 is also known as Darcy's law and is usually limited to cases where the Reynolds number is less than 1. This is often the case in fibrous filters, where the turbulence effects associated with higher Reynolds numbers are not realised. However, for heavily saturated filters, values of Reynolds number may be much greater then 1. So Darcy's law may be applied to filters that are not in a heavily saturated condition. However, given its origin in packed bed theory; the use of Darcy's law (and other channel theory equations) is only appropriate when the filter medium consists of a tight structure and has a high packing density (Hutten, 2007).

As the filter media which will be studied in this work typically have a loose structure and a low packing density it is more appropriate to model the flow through the filter in terms of cell model theories. These theories are based on flow past a single fibre (the Davies equation and drag model theory) or past an array of fibres (the Kuwabara model). The Davies equation may be expressed as,

$$\frac{\Delta P d_f^2 A_f}{\mu Q Z} = 64(1-\epsilon_p)^{1.5}[1+56(1-\epsilon_p)^3], \tag{2.7}$$

where ΔP is the pressure drop, A_f is the filter area, d_f is the fibre diameter, Q is the volumetric flow rate and $(1-\epsilon_p)$ is the packing density; which may also be expressed as α.

Equation 2.7 includes empirically-derived corrections to α which account for fibres not perpendicular to the flow direction. The equation may be re-written to predict the pressure drop across a dry filter for a given flow, (see Section 2.5.1 and Equation 2.19).

The drag model theory is, as the name implies, based on the drag forces acting on a fibre subject to fluid flow;

$$F_d = \frac{1}{2}\rho u^2 A C_D, \tag{2.8}$$

where F_d is the drag force, u is the velocity and C_D is the drag coefficient.

Several methods have been proposed for the determination of the drag coefficient and these are all functions of the Reynolds number;

$$Re = \frac{u d_f \rho}{\mu}. \tag{2.9}$$

The drag coefficient for a filter will differ from that of a single fibre, as neighbouring fibres will influence the flow around any given fibre. It is for this reason that the drag coefficient derived by Lamb (1932), which is for an isolated fibre, is inaccurate for fibrous filters.

Other attempts to determine the drag coefficient for filters have been made

by examining model systems; where the drag coefficient is determined for an array of equally spaced fibres (White, 1946; Chen, 1955). While more accurate than Lamb's equation, as they account for the influence of neighbouring fibres, to some extent, they are still not ideal as they do not account for the randomly distributed nature of fibres in a fibrous filter.

The Kuwabara model (Equation 2.10) deals with the flow past an array of cylinders that are situated perpendicular to the direction of the flow. In this model, two concentric circles are used to indicate the cylinder (fibre) and the flow field around the cylinder. It is assumed that at the outer circle the vorticity equals zero (Kuwabara, 1959). It is also assumed that there is no 'slip', hence

$$\frac{\Delta P d_f^2}{\mu v_0 Z} = \frac{32\alpha}{-ln\alpha + 2\alpha - \frac{\alpha^2}{2} - \frac{3}{2}}. \tag{2.10}$$

The Kuwabara model is perhaps the most commonly used model to describe air flow through a filter. When the denominator of the Kuwabara number is divided by two, the Kuwabara hydrodynamic factor, Ku, results; this factor has been extensively utilised in the development of other pieces of fibrous filter theory (see Section 2.5.3).

$$Ku = -\frac{1}{2} ln\alpha - \frac{3}{4} + \alpha - \frac{\alpha^2}{4} \tag{2.11}$$

2.3 Aerosol Droplet/Particle Capture Mechanisms

There are five collection mechanisms by which an aerosol droplet (or particle) may be captured by a fibre (Hinds, 1999). These are interception, impaction, diffusion, gravitational settling and electrostatic attraction. All bar electro-

static attraction are mechanical processes. These processes are illustrated in Figure 2.3.

Droplet (particle) capture by interception occurs when the droplets either have insufficient inertia to deviate from the streamline or are not subject to diffusive motion (Hutten, 2007). In such cases, the droplet will follow a streamline in the carrier gas. A droplet is intercepted when it passes within one particle radius of a fibre. The particle hits the fibre and owing to its finite size is captured (Hinds, 1999). So for a particular droplet size, certain streamlines will result in droplet capture and others will not.

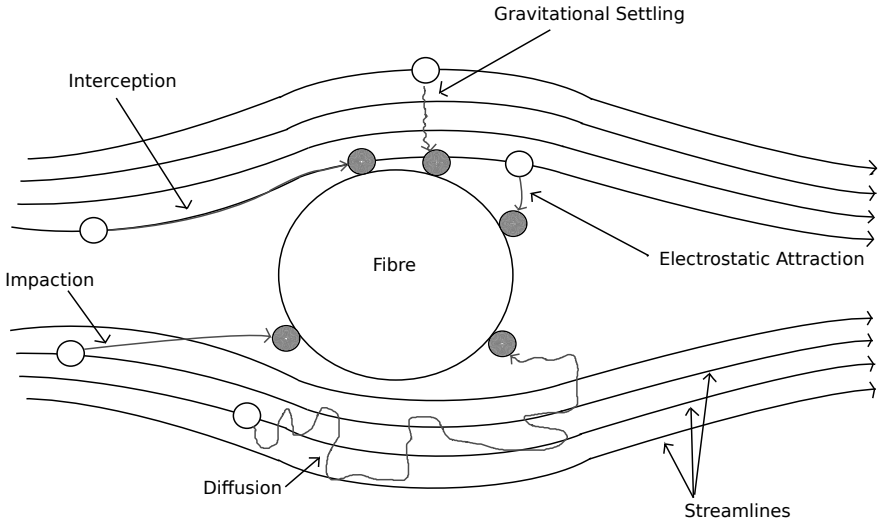

Figure 2.3: Diagrammatic representation of the mechanisms of particle capture

Capture by impaction occurs when a droplet, due to its inertia, is not able to adjust its direction with the abruptly changing streamlines that occur near the fibre (Hinds, 1999). This results in the droplet colliding with the fibre and being collected. Capture by the mechanisms of impaction and interception are generally more significant for particle sizes greater than 500 nm.

The capture of droplets by diffusion occurs due to the influence of Brownian motion over small droplets (particles). This motion is sufficient to significantly increase the chances of a droplet hitting a fibre whilst travelling past it on a non-intercepting streamline (Hinds, 1999). Typically, this mechanism is only significant for particles smaller than 500nm in diameter.

Gravitational settling is a less significant capture mechanism when dealing with small droplets. Unless the droplets involved are large and the velocities small, this method of capture is less significant than impaction (Hinds, 1999). In terms of developing equations for filter efficiency, collection efficiency due to gravitational settling is considered negligible and is generally not included in efficiency equations provided in the literature. The efficacy of gravitational settling is also highly dependent on filter orientation and face velocity.

The final capture method discussed here, electrostatic deposition, can be a significant factor in terms of particle capture mechanism(Hinds, 1999). It is however difficult to quantify as the charge on the fibres and the particles is often unknown. Increasing the number of elementary charges on either a fibre or a particle will generally increase the collection efficiency (Hinds, 1999). It is unlikely that electrostatic effects are significant in oil-mist filters, since the filter is typically fully wetted with aerosol and most oils are poor conductors.

2.4 Wetting and Contact Angles

In most cases when a liquid aerosol is captured by a filter fibre it will spread out to "wet" the fibre. The dynamics of wetting (with respect to interfacial science) has received significant attention (deGennes, 1985; Semal et al., 1999) and remains of interest today (Seveno et al., 2009). However, previous work has predominantly focussed on droplets on flat surfaces, with comparatively little work done on cylindrical elements (such as fibres).

Considering first a droplet on a flat plate (which when in equilibrium will take on the shape of a spherical cap), that such a droplet will have a contact angle that can be defined by Young's equation (McHale et al., 2001),

$$cos\theta_e = \frac{(\sigma_{SV} - \sigma_{SL})}{\sigma_{LV}}, \tag{2.12}$$

where θ_e is the equilibrium contact angle, σ_{SV} the solid-vapour interfacial tension, σ_{SL} the solid-liquid interfacial tension and σ_{LV} is the liquid-vapour interfacial tension.

This equation is obviously only applicable when $\theta > 0$ and will not apply in the case where the liquid completely wets the surface and forms a thin film.

Droplet or film formation on a flat plate may be predicted from the spreading coefficient (Brochard, 1986).

$$S_p = \sigma_{SV} - \sigma_{SL} - \sigma_{LV} \tag{2.13}$$

When $S_p < 0$ there will be partial spreading, resulting in the formation of a spherical cap (if gravity is negligible) and will therefore have a contact angle that may be determined from Youngs equation.

When $S_p > 0$ there will be total wetting and therefore film formation. It

should be noted that the liquid may not necessarily spread out to a monomolecular layer (Brochard, 1986). The thickness of the film does in fact represent a competition between the spreading coefficient and long range forces.

If a liquid droplet is small enough the effects of gravity may be considered negligible; and when it is in equilibrium with the surface its Laplace excess pressure will be constant (Carroll, 1976). Such that:

$$\Delta P_l = \sigma \left(\frac{1}{R_1} + \frac{1}{R_2} \right) = K_1 \tag{2.14}$$

Where ΔP_l is the Laplace excess pressure, R_1 and R_2 are the principle radii of curvature, σ is the interfacial (surface) tension and K_1 is a constant.

The concept of disjoining pressure was introduced by Derjaguin in 1936 (Adamson and Gast, 1997) to account for the fluid-solid interactions. Derjaguin and Churaev (1974) went on to suggest that the stability of thin liquid films and droplets on fibres be studied in terms of a competition between adhesion and capillarity. The equilibrium liquid arrangement on the fibre is then determined when the Laplace excess pressure and the disjoining pressure balance each other out. Such that there exists an equilibrium, where the Laplace pressure, that is trying to spread the droplet along the fibre, will be counteracted by the Disjoining pressure, which attempts to form discrete droplets.

In terms of droplets on fibres some work on wetting has been completed (Carroll, 1976; McHale et al., 1997; Bauer and Dietrich, 2000 and McHale et al., 2001). This work has focussed on describing the profile of axisymmetrical droplets and methods to accurately determine contact angles.

Carroll (1976) derived an expression for the profile of a barrel droplet and used this to express the Laplace excess pressure in terms of droplet geometry;

$$\Delta P = \sigma \left(\frac{1}{R_1} + \frac{1}{R_2} \right) = \frac{2\sigma}{d_f} \left(\frac{n_d - cos\theta_e}{n_d^2 - 1} \right), \tag{2.15}$$

where d_f is the fibre diameter and n_d is the reduced droplet diameter. Which is defined by the relation;

$$n_d = \frac{d_d}{d_f}, \tag{2.16}$$

where d_d is the droplet diameter.

Equation 2.15 expresses droplet shape as purely a function of Laplace excess pressure (i.e. vapour-liquid interactions) and does not take into account adhesive forces (i.e. solid-liquid interactions). This implies that the droplet outer surface may be treated as a surface of constant curvature. However this is not accurate as it has been documented (deGennes, 1985; Quere et al., 1988; Bacri et al., 1988 and others) that the contact angle of a droplet on a fibre differs from the contact angle of the same droplet on a flat plate, as there exists a transition zone between the apparent droplet edge and the film.

The convex surfaces of a fibre indicate that there will be positive curvatures on any coating films that develop; leading to a positive Laplace excess pressure acting on the film-air surface (Niemark, 1999). The Laplace pressure will generally try to spread a liquid over a surface. In the case of a fibre, where the film radius at the solid-liquid interface is different from that at the liquid-vapour interface, this pressure will act to force the liquid out of the film and in doing so introduce an instability. Here the liquid surface tension will act to minimise the free surface area, hence creating the instability (Yarin and Oron, 1993). This instability will cause the liquid film to undulate and break up into an array of droplets. This was first observed by Plateau (1873) who demonstrated that all axisymmetric wavelengths greater than the liquid cylinder (film) circumference will be unstable. Of all the possible wavelengths, the fastest mode will predominate (Rayleigh, 1892). This

is the commonly known phenomena, of Plateau-Rayleigh instability and for a thin film on a fibre the predominating wavelength will be $2\pi\sqrt{2}r$ (Quere, 1999).

Therefore the thickest possible film that could exist, on a thin cylindrical fibre, would be when the wavelength was equivalent to the circumference of the liquid cylinder coating the fibre. Such that:

$$2\pi\sqrt{2}r = 2\pi(r + h_t) \tag{2.17}$$

Mullins and Kasper (2006) show that this imposes a limit on the film thickness, h_t, of:

$$h_t = r(\sqrt{2} - 1) \tag{2.18}$$

With regards to fibrous filtration, it should also be remembered that the onset of Plateau-Rayleigh instability will also be influenced by the presence of overlapping and intersecting fibres as well as air flow through the filter. This implies that the maximum film thickness may in fact be less than indicated by Equation (2.18).

2.4.1 Fibre Wetting

The manner and degree by which a fibre may be wetted is dependent upon the properties of the fibre and the liquid droplets it collects. The collected droplets form one of the two principle types, either clamshell droplets or barrel droplets (Roe, 1975). Clamshell droplets have a contact angle of 90° or greater and display axial asymmetry (Mullins et al., 2006). While barrel droplets have a contact angle between 0° and 90°, are generally regarded as axisymmetric and posses a higher interfacial energy (Mullins et al., 2006).

When a droplet is captured on a wettable fibre, the droplet spreads onto the fibre surface, thereby 'wetting' it. This behaviour leads to the formation

of a thin film on the fibre, which almost immediately forms into regularly spaced barrel droplets upon the complete wetting of the fibre (via Plateau-Rayleigh instability) (Mullins and Kasper, 2006). It was suggested by Roe (1975) that in the section of the fibre between the barrel droplets there will exist an infinitesimally thin film. This film was indirectly observed by Mullins et al. (2006) where it was found that the barrel droplets will increase in size by absorbing aerosol particles without causing a detectable increase in the thickness of the film. Furthermore, Mullins and Kasper (2006) observed that if an aerosol droplet impacted this film it would be transported to the closest droplet.

In the case of non-wettable fibres, the captured droplets do not spread along the fibre, but remain as distinct droplets with high contact angles (Agranovski and Braddock, 1998a). These droplets initially appear as a 'cap' and as further droplets are captured, coalesce into larger clamshell droplets (Mullins et al., 2005). The collected droplets will continue to grow in size, either by capturing more droplets or by coalescing with neighbouring droplets, until they leave the fibre (Mullins et al., 2005). This will occur when either the droplet has accumulated sufficient mass that the gravitational forces over come the adhesion forces, or when the velocity of the passing air stream is of sufficient velocity to cause the droplet to blow off the fibre. A diagrammatic representation of barrel and clamshell shaped droplets on wettable and non-wettable fibres is shown in Figure 2.4. It should be noted that there will be a slight difference between the advancing (θ_A) and receding (θ_R) contact angles.

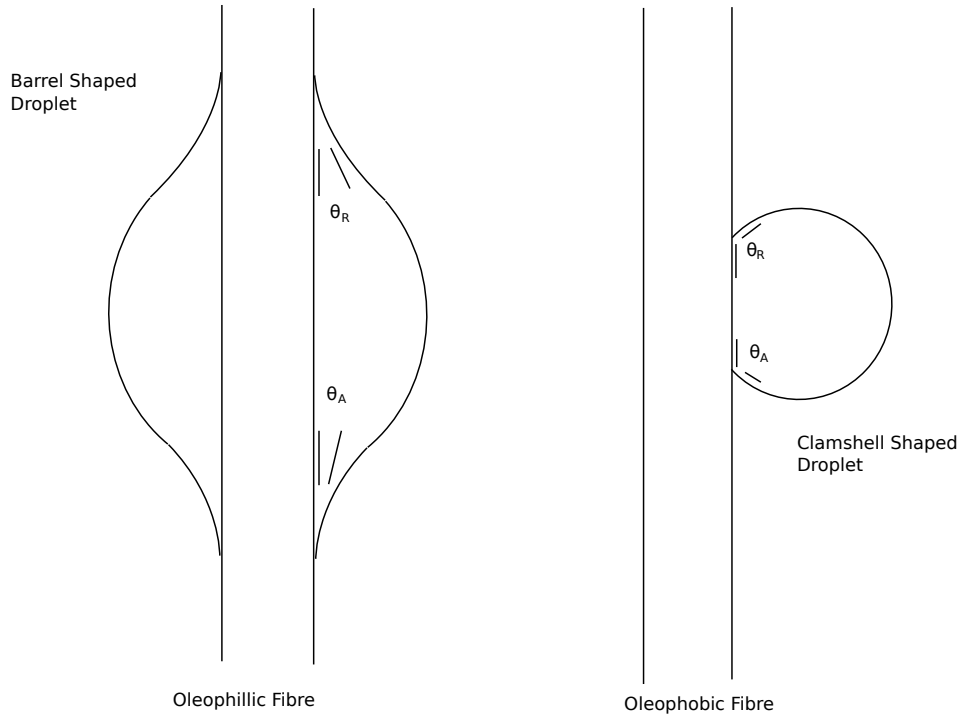

Figure 2.4: Diagrammatic representation of barrel and clamshell shaped droplets on wettable (oleophillic)and non-wettable (oleophobic) fibres

In operation, the mist droplets will coalesce very rapidly with ongoing filtration, forming large (tens of microns in diameter) droplets. The shape of these droplets will be determined in part by the wettability of the fibres, by gravitational and frictional forces and by the interfacial or surface energy of the fibre-liquid and liquid-vapour interfaces (Mullins et al., 2003).

2.4.2 Contact Angles on Fibres

One of the most difficult challenges faced during research into wetting behaviour in fibrous filters is the accurate determination of the contact angle. In the case of a liquid droplet on a flat plate, the equilibrium contact angle

is as defined by Equation 2.12. On a cylindrical element however it is not quite so simple, as there is a well documented (deGennes, 1985; Quere et al., 1988; Bacri et al., 1988) transitional zone between an axisymmetric droplet and the thin film that exist on such elements. Hence, the contact angle of coalesced droplets on filter fibres is difficult to measure as there is a high degree of curvature at the interface.

2.5 Modelling

Given the complex nature of fibrous liquid aerosol filters and the many variables involved (fibre diameter, packing density, filter face velocity, fibre material, liquid properties etc) accurate modelling of filter behaviour is difficult. The models currently available are predominantly empirically derived and apply only to specific liquids on a particular fibre type over a narrow range of diameters and packing densities. Other models only deal with the filter in its clean (unloaded) state, or in its saturated/entrained state. Thus, there are no models currently available that allow the prediction of the transition points and therefore there is no way to create a fully optimised filter design.

2.5.1 Pressure Drop

Several models for filter pressure drop have been proposed; however these only account for either pressure drop across the dry filter, or the pressure drop over the filter once it has reached the "pseudo"-steady state. For a dry (clean) filter Equation 2.7 can be rearranged to give,

$$\Delta P_0 = \frac{u_0 \mu_g Z}{d_f^2}[64\alpha^{1.5}(1 + 56\alpha^3)] \tag{2.19}$$

(Davies, 1952). Where ΔP_0 is the pressure drop across a clean filter, u_0 is the gas velocity at the filter face, μ_g the gas viscosity, Z the filter thickness, d_f the fibre diameter, α is the filter solidity or packing density and the term in the

square brackets is an empirical correction to account for non-perpendicular fibres.

Or alternatively, once the "pseudo"-steady-state has been established;

$$\Delta P_s = \Delta P_0 \left[1.09 \left(\alpha_f \frac{Z}{d_f} \right)^{-0.561} \left(\frac{U_0 \mu - l}{\sigma_{LV} cos\theta_c} \right)^{-0.477} \right] \tag{2.20}$$

(Liew and Conder, 1985). Where ΔP_s is the "pseudo"-steady state pressure drop, ΔP_0 the pressure drop across a clean filter, α_f the clean filter packing density (dimensionless), Z is the filter thickness, U_0 the filtration velocity, d_f is the mean fibre diameter, σ_{LV} is the liquid surface tension, θ_c the contact angle and μ_l is the liquid viscosity.

There is currently no model which can accurately predict filter pressure drop behaviour during loading (of a broad range of filter types) and therefore no way of predicting the location of the transition points.

A modification of the Davies pressure drop model has been found to give satisfactory results for early filtration stages (Frising et al., 2005). In this model the fibre diameter term (d_f) and fibre packing density (α) have been replaced by the wet fibre diameter (d_{fwet}) and wet fibre packing density (α_{wet}) such that the model becomes;

$$\Delta P = u_0 \mu_g L \frac{64 \alpha_{wet}^2 (1 + 56 \alpha_{wet}^3)}{d_{fwet}^2}, \tag{2.21}$$

where ;

$$\alpha_{wet} = \alpha_f + \frac{m_{liq}}{\Omega \rho_l L}, \tag{2.22}$$

$$d_{fwet} = d_f \sqrt{1 + \frac{m_{liq}}{\Omega \rho_l Z \alpha_f}}, \tag{2.23}$$

and u_0 the gas velocity at the filter face, m_{liq} the collected liquid mass, Ω the filtration surface area and ρ_l is the liquid density (Davies, 1973).

This model, however requires that the liquid perfectly wets the fibres and that the liquid is distributed uniformly through the filter (Frising et al., 2005). It is therefore only appropriate for the early stages of filtration (i.e. when depth filtration is occurring, Contal's stage 1 (Contal et al., 2004)).

2.5.2 Saturation

Currently only one (accurate) model has been developed to allow the prediction of steady state filter saturation, this is the model developed by (Raynor and Leith, 2000). This model utilises three dimensionless terms, the Bond number (Bo), the Capillary number (Ca) and a Drainage rate term (Dr), to predict the equilibrium filter saturation (S_{Fe}).

The Bond number is used to describe the liquid transport through the filter and is given as;

$$Bo = \left(\frac{\rho_l g d_f^2}{\sigma}\right) \times 10^5, \tag{2.24}$$

where ρ is the fluid density, g is the acceleration due to gravity, d_f is the fibre diameter and σ is the surface tension of the liquid.

The Capillary number is used to describe re-entrainment or blow off from the filter and is given as;

$$Ca = \left(\frac{\mu_g u_0}{\sigma}\right) \times 10^5, \tag{2.25}$$

where μ_g is the gas viscosity and u_0 is the filter face velocity.

The drainage rate from the filter was assumed (by Raynor and Leith (2000)) to be controlled by a dimensionless Drainage rate term; given as

$$Dr = \left(\frac{\mu_l D}{\sigma Z W}\right), \tag{2.26}$$

where μ_l is the liquid viscosity, Z is the filter thickness, W is the width of the test filter in the direction perpendicular to the flow and to gravity (Raynor and Leith, 2000).

The equilibrium saturation is then,

$$S_{Fe} = \frac{\alpha^{0.39}}{Bo^{(0.47+0.24ln(Bo))}Ca^{0.11}} \times exp(-0.04 + 6.6 \times 10^5 Dr) \tag{2.27}$$

(Raynor and Leith, 2000). This model is however only applicable to glass fibre filters with a packing density between 0.026 and 0.035; a thickness of approximately 88mm; with fibre diameters of 3 to 8 microns and only when collecting di-ethyl-hexyl-sebacate (Mullins et al., 2006). In addition to this, the model does not adequately account for variations in the filter face velocity. It has been shown that the relationship between saturation and velocity is far more significant than the $Ca^{0.11}$ term in the model implies (Frising et al., 2005). This is discussed further in Chapter 4.

2.5.3 Single Fibre Efficiency

Given the complex random structure of fibrous filters it has proven difficult to develop comprehensive models that may be applied over all possible structures. Therefore the capture efficiency of fibrous filters is examined at a simpler (elementary) level; that of the collection of droplets by a single fibre. Utilising this approach, where a single fibre situated perpendicular to the flow direction is considered, a number of authors (Chen, 1955; Stechkina et al., 1969; Yeh and Liu, 1974 and others) have developed a series of semi-

empirical equations that predict the capture efficiency of a single fibre on the basis of individual capture mechanisms (see Section 2.3). These equations are collectively known as the Single Fibre Efficiency (SFE) theory.

Given the semi-empirical nature of these equations there are a number of variations in the formulae which have been proposed by authors to improve the accuracy of the predicted efficiency for the filters they have been using.

Given that the flow rates through fibrous filters are typically quite low, the flow field remains laminar and as such under a laminar flow regime the distortion of the flow caused by an individual fibre will influence the flow around neighbouring fibres (Hinds, 1999). The single fibre theory accounts for this effect via the inclusion of the Kuwabara hydrodynamic factor (Ku), discussed in Section 2.2, in equations for efficiency by inertial impaction, interception and diffusion. The single fibre efficiency is a function of the different efficiencies of each of the collection mechanisms available. The mechanical single fibre efficiencies can be combined as long as each acts independently and is less than 1 (Hinds, 1999).

The single fibre efficiency due to interception, η_R, (based on the Kuwabara flow field) is given by (Lee and Liu, 1982) as;

$$\eta_R = \frac{1 + N_R}{2Ku}\left[2ln(1 + N_R) - 1 + \alpha + \left(\frac{1}{1 + N_R}\right)^2\left(1 - \frac{\alpha}{2}\right) - \frac{\alpha}{2}(1 + N_R)^2\right], \tag{2.28}$$

where N_R is the ratio of aerosol particle/droplet diameter to fibre diameter.

Several investigators have offered simplifications of Equation 2.28; all however have their limitations. Lee and Liu (1982) proposed the following expression;

$$\eta_R = \frac{1 - \alpha}{Ku}\frac{N_R^2}{1 + N_R}. \tag{2.29}$$

This approximation requires that N_R is small. Lee and Liu (1982) found that this approximation was superior to those offered by other investigators when α becomes large. This is because the approximation offered by Stechkina (1966) ignores all terms involving α, such that;

$$\eta_R = \frac{1 + N_R}{2Ku}\left[2ln(1 + N_R) - 1 + \frac{1}{(1 + N_R)^2}\right]. \tag{2.30}$$

This equation is therefore limited to small values of α, as well as requiring that N_R is small. Other authors have offered their own simplifications of Equation 2.28 also omitting α which also suffer in accuracy and are subject to the same limitations as Equation 2.30.

Based on their experimental results, Lee and Liu (1982) added a coefficient to their approximation, giving

$$\eta_R = 0.6\left(\frac{1 - \alpha}{Ku}\right)\frac{N_R^2}{1 + N_R}. \tag{2.31}$$

The single fibre efficiency due to impaction, η_I, may be determined from the following equation; developed by Stechkina et al. (1969),

$$\eta_I = \frac{S_t}{4Ku^2}[(29.6 - 28\alpha^{0.62})N_R^2 - 27N_R^{2.8}]. \tag{2.32}$$

Where S_t is the Stokes number which is found using,

$$S_t = \frac{\rho_p d_p^2 C_c u'}{18\mu_g d_f}, \tag{2.33}$$

where ρ_p is the particle density, d_p the particle diameter, u' is the interstitial velocity and C_c is the Cunningham correction factor;

$$C_c = 1 + \frac{2.52\lambda}{d_p}. \tag{2.34}$$

It should be noted that Equation 2.32 is only valid for values of N_R which are less than 0.4. If the value of N_R is greater than 0.4 then N_R should be set as 0.4 for the calculations (Raynor and Leith, 2000).

The single fibre efficiency by diffusion, η_D, can be described by the expression developed by Lee and Liu (1982),

$$\eta_D = 1.6 \left(\frac{1-\alpha}{Ku} \right)^{\frac{1}{3}} Pe^{-\frac{2}{3}}, \tag{2.35}$$

where, Pe, is the Peclet number, defined as;

$$Pe = \frac{u' d_f}{D_p}, \tag{2.36}$$

with D_p, the droplet diffusion coefficient;

$$D_p = \frac{k_B \, TC_c}{3\pi\mu d_p}, \tag{2.37}$$

and k_B is the Boltzmann constant.

More generally the single fibre efficiency of diffusional capture is expressed as;

$$\eta_D = APe^{-\frac{2}{3}}, \tag{2.38}$$

where A is a constant dependent on the filter parameters used (Cheng et al., 1990).

Equation 2.38 (used with the appropriate value of A) is generally preferred over Equation 2.35 as it has been demonstrated that the diffusional deposition efficiency is independent of α (Chen, 1955; Cheng et al., 1990). The

values for A as given by Cheng and Yeh (1980) are 1.5 to 2 for real filters and 2.7 for regular screen or mesh. Hinds (1999) gives the value of A simply as 2, without differentiating between filter parameters. Thus care must be taken when choosing an expression for diffusional capture efficiency, with a value of A being chosen based on the nature of the filter.

Gravitational setting is described by the dimensionless term G_s (Hinds, 1999),

$$G_s = \frac{\rho_g d_p^2 C_c g}{18 \mu_g U_0}. \tag{2.39}$$

With the single fibre efficiency (of a vertically oriented filter) by gravitational settling, η_G, being described as;

$$\eta_G \approx -G_s(1 + N_R). \tag{2.40}$$

The efficiency due to gravitational settling will have the effect of decreasing the overall fibre efficiency (Hinds, 1999). In comparison to other mechanisms, η_G is small unless the particle size is large and the velocity low.

In the case of electrostatic deposition, Brown (1993) determined a function for single fibre efficiency by electrostatic attraction, η_q, from experimental results. This term applies to a neutral fibre that is collecting a charged particle, such that;

$$\eta_q = 1.5 \left[\frac{(\epsilon_f - 1)}{(\epsilon_f + 1)} \frac{q^2}{12 \pi^2 \mu_g U_0 \epsilon_0 d_p d_f^2} \right]^{\frac{1}{2}}, \tag{2.41}$$

where ϵ_f is the relative permittivity (dielectric constant) of the fibre, ϵ_0 is the permittivity of a vacuum and q is the charge on the particle.

Electrostatic deposition is not a mechanism that occurs in a significant way

in oil mist filters as the oil droplets are typically uncharged (Hinds, 1999). Alternatively if charged fibres were to be used; they would lose their charge once exposed to an organic liquid aerosol, such as oil mist (Hinds, 1999).

The total single fibre efficiency, η_F, is a function of single fibre efficiencies of each of the different capture mechanisms. In their work, Lee and Liu (1982), considered only the mechanisms of diffusion and interception. They go on to make the assumption that one of these mechanisms is predominant and that the influence of the other is minor. Therefore the total single fibre efficiency is the sum of the efficiencies of the two mechanisms, such that;

$$\eta_F = \eta_D + \eta_R. \tag{2.42}$$

Giving:

$$\eta_F = 1.6 \left(\frac{1-\alpha}{Ku}\right)^{\frac{1}{3}} Pe^{-\frac{2}{3}} + 0.6 \left(\frac{1-\alpha}{Ku}\right) \frac{N_R^2}{1+N_R}. \tag{2.43}$$

Equation 2.43 applies to a continuous flow regime, which would be indicated by a small (negligible) Knudsen number, Kn,

$$Kn = \frac{2\lambda}{d_f}, \tag{2.44}$$

where λ is the mean free path of the carrier gas. In their work Payet et al. (1992) found a discontinuity of the fluid around the fibre, and therefore added a correction for slip flow.

Liu and Rubow (1990) proposed the following correction,

$$\eta_F = 1.6 \left(\frac{1+\alpha}{Ku}\right)^{\frac{1}{3}} Pe^{-\frac{2}{3}} C_d + 0.6 \left(\frac{1-\alpha}{Ku}\right) \frac{N_R^2}{1+N_R} C_r, \tag{2.45}$$

where;

$$C_d = 1 + 0.388Kn\left(\frac{(1-\alpha)Pe}{Ku}\right)^{\frac{1}{3}} \tag{2.46}$$

$$C_r = 1 + \frac{1.99Kn}{N_R}. \tag{2.47}$$

It was observed by Payet (1991) that the single fibre efficiency given by the corrected equation of Liu and Rubow (1990) may be greater than 1 for low Peclet numbers. She went on to propose a further correction to the diffusion efficiency term, such that,

$$\eta_D = 1.6\left(\frac{1-\alpha}{Ku}\right)^{\frac{1}{3}} Pe^{-\frac{2}{3}} C_d C'_d, \tag{2.48}$$

where;

$$C'_d = \frac{1}{1 + 1.6\left(\frac{1-\alpha}{Ku}\right)^{\frac{1}{3}} Pe^{-\frac{2}{3}} C_d}. \tag{2.49}$$

The fibre efficiency term then becomes;

$$\eta_F = 1.6\left(\frac{1+\alpha}{Ku}\right)^{\frac{1}{3}} Pe^{-\frac{2}{3}} C_d C'_d + 0.6\left(\frac{1-\alpha}{Ku}\right)\frac{N_R^2}{1+N_R} C_r. \tag{2.50}$$

In addition to diffusion and interception, Raynor and Leith (2000) also consider droplet collection via impaction and offer their own expression for the total single fibre efficiency,

$$\eta_F = \eta_R + \eta_I + \eta_D - \eta_D(\eta_R + \eta_I). \tag{2.51}$$

Where the final term is a correction allowing for the fact that each mechanism is not truly 100% independent of the others. Alternatively, Hinds (1999), offers a term which takes into account the interaction between the interception and diffusion mechanisms;

$$\eta_{DR} = \frac{1.24 N_R^{\frac{2}{3}}}{(KuPe)^{\frac{1}{2}}}. \tag{2.52}$$

The single fibre efficiency is then determined from;

$$\eta_F = 1 - (1 - \eta_R)(1 - \eta_I)(1 - \eta_D)(1 - \eta_{DR})(1 - \eta_G). \tag{2.53}$$

The formula used to determine single fibre efficiency should be chosen on the basis of the droplet capture mechanisms that are taking place and their predominance. Captured droplets on the filter are capable of collecting droplets from the air stream, and it has been shown that these droplets can span several fibres and restrict the local air flow (Liew and Conder, 1985).

2.5.4 Filter Efficiency and Penetration

The efficiency of the filter, and hence the penetration, may found using an expression utilising, η_F. The penetration, P_e, of a filter medium may be defined as the number of particles crossing (or passing through the filter) over the number of particles collected by the filter. Thus the penetration is simply,

$$P_e = 1 - \eta_T. \tag{2.54}$$

Assuming that the filter saturation ratio, S, does not vary with distance

through the filter, the total efficiency of a filter, η_T, may be determined using;

$$\eta_T = 1 - exp\left[\frac{-4\alpha\eta_F Zf}{\pi(1-\alpha)(1-S)d_f}\right]. \tag{2.55}$$

Where the proportion of the fibre surface not covered by liquid, f, is:

$$f = 1 - \frac{d_d}{x_d}, \tag{2.56}$$

and the droplet diameter, d_d, is approximately;

$$d_d = \left[\frac{3S(1-\alpha)d_f^2 x_d}{2\alpha}\right]^{\frac{1}{3}}. \tag{2.57}$$

With the distance between the fattest point on the collected droplets, x_d, being approximately;

$$x_d = 5\left[\frac{S(1-\alpha}{\alpha} + 1\right]^{\frac{1}{2}} d_f. \tag{2.58}$$

The filter saturation ratio may, however vary through the filter or may be unavailable. Hinds (1999) presents an expression for total efficiency that does not involve the saturation ratio, such that;

$$\eta_T = 1 - exp\left(\frac{-4\alpha\eta_F Z}{\pi d_f}\right). \tag{2.59}$$

This expression does not however have its origins in dust filtration and as such does not deal with (saturated) mist filters.

The single fibre efficiency is determined using the individual efficiencies of the predominating capture mechanisms that are in play in the system. These are determined on the basis of the physical properties of the aerosol, so for

an oil-mist, with a typical particle size distribution (1nm-1000nm), the single fibre efficiency should be determined using the mechanisms of interception, impaction and diffusion if electrostatic effects can be ignored.

Several penetration models are offered in the literature which posses variable accuracy and are usually dependent on the packing density of the test filters used by the authors and the particular aspect of filter behaviour they held responsible for the increase in penetration of the filter. Raynor and Leith (2000) used low packing density filters (0.016-0.054) and offer the following;

$$P_e = exp\left[-\frac{4\eta_F \alpha Zf}{\pi(1-\alpha)(1-S_e)d_f}\right]. \tag{2.60}$$

The packing density of the filter has a strong influence on the distribution of liquid within the filter. Liew and Conder (1985) show photographs of two filter media of different packing density under an incident light microscope in the entrained state. These show that for the low packing density (0.004) filter there are single large droplets where two or more fibres intersect (Liew and Conder, 1985). For the higher packing density filter the liquid does not exist as discreet droplets but as pools or patches spanning several fibres (Liew and Conder, 1985). Payet et al. (1992) go on to suggest that for filters with a packing density of less than 0.04 the spaces between fibres are large, so the liquid exists as droplets and for packing densities over 0.04 fibres are closer together than the diameter of collected droplets, so irregular pools or patches form.

Payet et al. (1992) offered the following model for filter penetration,

$$P_e = exp\left[-\frac{4\eta_F \alpha(1-S_e(1-\alpha))Z}{\pi[1-\alpha(1-S_e(1-\alpha))]d_f}\right], \tag{2.61}$$

where the packing density term has been modified to take into account the decrease in the collection surface caused by the formation of liquid bridges

at fibre intersections. The filters used by Payet et al. (1992) had a packing density of 0.08; so by their description irregular pools and patches of liquid appear on the filter and hence a correction is made to account for the decrease in collection area.

As well as causing a decrease in the collection area of filters, the clogging process also causes an increase in the effective fibre diameter of the filter fibres. Gougeon et al. (1994) hold this effect responsible for the increase in penetration and offer the following expression for filter penetration;

$$P_e = exp\left[-\frac{4\,\eta_F \alpha_f\, d_{fwet}}{\pi(1-\alpha_f)\, d_f}\right], \tag{2.62}$$

where the wet fibre diameter, d_{fwet}, is as defined by Davies (1973).

None of these models however, can accurately describe filter penetration during clogging and over a range of pressure drops (Frising et al., 2005).

2.5.5 Capillarity and Capillary Rise Modelling

The capillary effects that occur within textiles and other media have been a topic of recent studies (Mullins et al., 2007a). In some cases involving media where the void space is relatively low it has been possible to describe capillarity with the use of hydraulic conductivity equations commonly used in soil physics (Mullins et al., 2007a). The study of fibrous, porous material has however been limited.

Some of this work has made use of the Lucas-Washburn model (used commonly in industry) to predict capillary rise (Mullins et al., 2007a). However there exists very little information in the literature on the application of this model to fibrous filters or the relationship between capillary radius and a readily measurable filter parameter (e.g. fibre diameter or packing density).

The capillary models used with porous materials are generally based on ex-

pressions for a single capillary tube (Hyvaluoma et al., 2006). So in order to apply such a model to a fibrous filter, a mean or equivalent capillary radius needs to be determined.

Mullins et al. (2007a) found that (for the filters examined) a well defined relationship between capillary radius, r_c, and the packing density over fibre radius, α/r_f, exists, such that;

$$r_c = Aln\left(\frac{\alpha}{r_f}\right) - B, \tag{2.63}$$

where A and B are media specific constants.

Therefore there is a potential for the saturation of a filter to be predicted on the basis of capillary theory.

2.5.6 Other Models

In contrast to the pressure drop and saturation models mentioned in Sections 2.5.1 and 2.5.2, Frising et al. (2005) proposed a model that does not deal with the filter as a whole, but divides it into layers. The model presented then deals with pressure drop and filter penetration in terms of a given filter layer, j. The model also incorporates different equations for each of the four stages presented by Contal et al. (2004).

The model for penetration is of the form,

$$P_e = exp\left(-\frac{4\,\alpha_f}{\pi\,d_f}dZ\right), \tag{2.64}$$

with dZ describing the thickness of the filter layer, j. The model introduces additional terms to this equation based on the change in packing density that occurs as the filter becomes clogged with liquid.

The pressure drop equations are based on a modified version of the Davies

pressure drop equation (Equation 2.19).

$$\Delta P = 64\,\mu\, U_0\, dZ \frac{(\alpha + \alpha - l)(\alpha + \alpha_l)^{0.5}}{d_{fwet}^2}(1 + 16(\alpha + \alpha_l)^{2.5}) \qquad (2.65)$$

Where α_l is the liquid packing density and the d_{fwet} term is as defined by Davies (1973). This equation is given as the pressure drop for the first stage. The equation for subsequent stages is of this form with an additional factor to account for the increase in velocity through the filter that occurs as it clogs. This correction also incorporates the change in packing density that occurs due to the presence of collected liquid.

This model is based on the assumptions that the packing density and fibre distribution are constant throughout the filter, that all the fibres in the filter are of the same diameter and that the liquid perfectly wets the fibres (Frising et al., 2005). One issue to arise from the work by Frising et al. (2005) is their assumption of film flow. In their work, Frising et al. (2005) have stated that a 'liquid tube forms around the fibre at the beginning of filtration. They go on to define a packing density term for this liquid tube, α_{tube}, which they describe as the limit liquid packing density . This packing density term is used in the additional terms for stages two and three. Thus the pressure drop and penetration models are somewhat dependent upon α_{tube}, for the stages between where clogging begins and the establishment of the "pseudo"-steady state.

In a paper by Mullins and Kasper (2006) the idea of the 'liquid tube is refuted. They show that continuous liquid films, as implied by the liquid tube concept, cannot exist without the presence of droplets. As a film existing on a single filter fibre will be broken up by Plateau-Rayleigh instability (Mullins and Kasper, 2006); see Section 2.4 . Therefore in using the packing density of the liquid tube in their model (or any other parameter relating to this liquid tube) Frising et al. (2005) have introduced a source of error into

their model, which may go some way to explaining the significant deviation between their experimental results and the values obtained from their model.

While there is some merit in using different equations to describe each of the different stages in the filtration, there still exists the problem of determining the location of the transition points. So while one might be able to examine a set of experimental results to see what parts correspond to each stage, one cannot use the model equations to predict when the transition between the stages occur (for new filters which have not been measured).

Charvet et al. (2010) also considered modelling filter behaviour, by dividing the filter into a number of theoretical layers. Though they also pointed out that a thin filter (0.34mm thick in their work) could be modelled without considering individual theoretical layers. The model presented is essentially a simulation and is solved layer by layer and in an iterative fashion, calculating the single fibre efficiency at each layer and the particle size distribution of the aerosol that penetrates the previous layer. Based on the amount of aerosol collected by each layer it is possible to calculate a new packing (or more correctly bulk-) density, for each layer for use in the single fibre efficiency equations, by using Equation 2.22 and also a new interstitial velocity, which can then be used in the next iteration.

There is, however some significant variation between the experimental and modelled values presented by Charvet et al. (2010), particularly at the beginning of clogging. This perhaps demonstrates the difficulties associated in selecting the appropriate variation of the single fibre efficiency equations and is a reminder that they are semi-empirical in nature and so do not work perfectly.

2.6 Colloid Aerosols

In the literature, the term colloid aerosol has previously been applied to describe a system of small solid particles dispersed within a carrier gas (Berry

et al., 1989; Ryu et al., 2007). This system is simply an aerosol, describing it as a colloid aerosol provides no further information about its composition or properties. Therefore it is proposed that the term colloid aerosol be used to describe a system in which the particles that make up the dispersed phase are themselves a colloid. Thus the oil-soot system (as occurs in aerosols generated from diesel engine crankcases), which when aerosolised form small oil droplets which contain soot particles, can be said to form a colloid aerosol. It is this definition that will be used in this work.

The majority of research into oil mist filtration has focussed on aerosols made up of dispersions of di-ethyl-sebacate (DES), di-ethyl-hexyl-sebacate (DEHS), geraniol, di-octyl-phthalate (DOP) or laboratory grade light mineral oils. Few studies have been performed using multi-component lubricating oils and even fewer involving the capture of aerosols in which the dispersed phase consists of both solid and liquid particles.

In many situations oil-mist filters are called upon to filter oil mists which also contain solid particulate matter. It is believed that the interactions between solid particles and liquid droplets have a significant influence on filter behaviour, especially in terms of pressure drop and efficiency (**?**Frising et al., 2005). To date only two studies have been carried out that look at the simultaneous capture of solid and liquid aerosol mixtures (Mullins et al. (2004); Frising et al. (2004)). This is important; especially in the case of crank case oil mist filters, as through out its life lubricating oils will become soot-laden and this may influence the behaviour of oil mist filters. It is believed that fibrous filters will become clogged with solid particulate matter, such as soot in the case of diesel crankcase filters, and dust, metal particles in most other applications, and that this will result in a significant increase in pressure drop.

The soot dispersed within the oil will essentially form a lyophobic colloid. When through heat and frictional forces this mixture becomes aerosolised, the result will be an aerosol made up of oil droplets that contain soot particles. This differs from many natural or anthropogenic aerosols which have a

single particle (nucleus) at the core. Therefore each oil particle in the aerosol is a small colloidal suspension.

2.7 Atomic Force Microscopy

A technique which has previously been applied to surface and fibre wetting studies is atomic force microscopy. The atomic force microscope (AFM) is a form of scanning probe microscope (SPM) which is a development of the scanning tunnelling microscope (STM), originally developed by Binnig et al. (1981). The original STM was limited to measuring only samples that were capable of conducting electricity, but subsequently led to the development of instruments that could measure a variety of physico-chemical interactions that occur between a measuring tip and a sample (Leite and Herrmann, 2005). Atomic force microscopy has been applied to a wide range of sample surfaces to allow the imaging (down to the subnanometer scale) of structural and dynamic features; as well as being used to measure inter and intra molecular forces.

2.7.1 Basic Principles

Atomic force microscopy makes use of a small probe or tip attached to end of either a rectangular or a V-shaped cantilever. The tip is small (nano-scale) and is placed in contact or near contact with a sample surface. As the tip is moved over the sample surface the cantilever is subject to deflection forces, as it follows the topography of the sample or variations in the interaction forces between the cantilever tip and the sample (Leite and Herrmann, 2005).

The original AFM, as developed by Binnig, Quate and Gerber in 1986, measured the deflection of the cantilever using an STM (Binnig et al., 1986). In this early example, the AFM cantilever had to be conductive so that its deflection could be measured by the STM. Meyer and Amer (1988) implemented a new method to measure the movement of the cantilever, whereby a

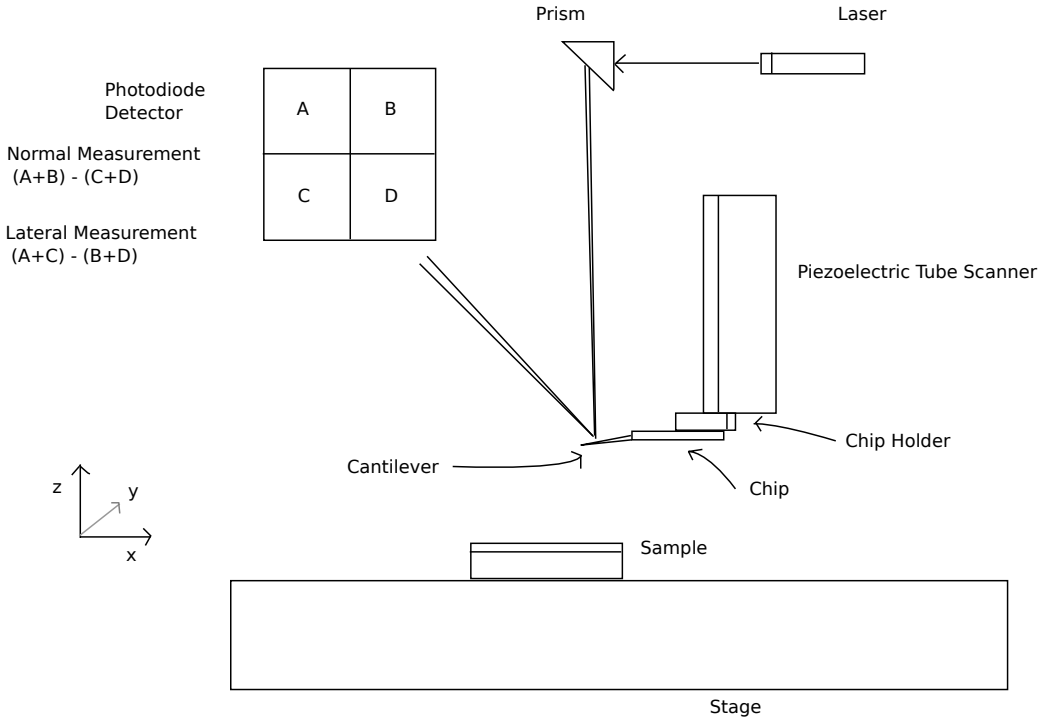

Figure 2.5: Simplified schematic representation of an AFM (not to scale)

laser is reflected off the back of the cantilever and the deflection is measured by a position sensitive photodiode detector. This system is illustrated in Figure 2.5. This detector reads the data from the laser and allows a line by line image of the sample surface to be generated.

The forces acting on the tip will result in the deformation of the cantilever that the tip sits on. This deformation is measurable, as described above. The exact make up of the forces acting on the tip will be dependent on the operating mode of the AFM and on the imaging conditions. There are a number of operating modes which may be used, including; contact mode, non-contact mode, friction force microscopy and tapping mode. The mode

selected will be dependent on the nature of the sample and which particular aspect is being measured.

2.7.2 Scanning Modes

Of all the scanning modes available, contact mode is the most widely used (Wickramasinghe, 2000). This, as its name implies, is a method whereby the AFM tip is held in intimate contact with the sample surface. This method may be used to acquire high precision images of sample surface topography, but will also apply shear stresses to the surface (Leite and Herrmann, 2005).

Friction force microscopy (FFM) (also known as lateral force microscopy) is a development of the contact mode. The only significant difference is that with FFM the detector is configured so that in addition to detecting deflectional movement of the cantilever, it also measures torsional (lateral) movement. This mode has found much use in the field of nanotribology (Bhushan et al. (1995); Sheehan and Lieber (1996)) and has also been successfully applied to studies on the mobility of adsorbed colloids (Yuan and Lenhoff, 2003).

The non-contact mode is an AFM method where the cantilever is not in physical contact with the sample. In this method the cantilever is placed very close to the sample surface so that the cantilever is subject to the attractive forces that exist between the surface and the cantilever tip. The attractive force is measured indirectly, by recording the changes to the resonance frequency of the cantilever.

The contact mode suffers from a major drawback in that it can damage the sample surface, particularly in studies of soft samples or thin liquid films. Conversely, if the sample is hard (for example silica) the tip itself may wear down. There is also the issue of capillary condensation when the AFM is operated in air (Zhong et al., 1993).

The non-contact mode deals with these problems but suffers from its own drawbacks. If the cantilever oscillates too closely to the surface it may be captured by the surface due to short range van der Waals forces, and would then have to be removed from the surface so that sample measurements could continue (Zhong et al., 1993).

The tapping or intermittent contact mode is an operating mode where the cantilever is deliberately excited so that it jumps up and down (taps) on the sample surface. In this method the change in the oscillation amplitude caused by tapping the surface is measured (Zhong et al., 1993). This method can provide high resolution topographical images and has the effect of excluding the variation in frictional force that influences images taken in the contact mode.

2.7.3 Applications

The versatile nature of atomic force microscopy has led to its use in a wide range of areas including studies of wetting and adhesion, biological systems, electrochemistry, crystallisation and studies of inter and intra-molecular forces. The key to its versatility is the ability to examine a surface with true atomic scale lateral resolution; which may be achieved by careful control of the sample/measurement conditions and has a reliability similar to that of the scanning tunnelling microscope (Ohnesorge and Binnig, 1993).

The atomic force microscope offers a significant advantage over the scanning tunnelling microscope in that it does not require a vacuum in order to obtain highly resolved images. It may be used for measurements in air (i.e. at atmospheric pressure) through a range of pressures down to those of an ultra high vacuum.

Marti et al. (1987) used AFM on samples coated with paraffin oil and successfully demonstrated that atomic resolution could be obtained when the

samples were covered with a liquid film. This has led to the use of AFM in the fields of biology (Hansma et al., 1988) and electrochemistry (Manne et al., 1991). An extension of this was then using atomic force microscopy to study liquid structures on surfaces and wetting behaviour (Herminghaus et al., 2000).

One of the principle applications of AFM is the measurement of surface forces (down to the picoNewton scale). The forces that exist between the cantilever and the sample surface may be determined from measurements of the deflection of the cantilever. These measurements may then be equated to a force through the use of a spring constant, k_s.

This is essentially an application of Hookes law; where the extension produced is proportional to the load, such that,

$$F = -k_s X_e, \tag{2.66}$$

where X_e is the distance that the spring has been moved from its equilibrium position.

In this case, the spring constant is that of the cantilever being used; which may be determined experimentally. The spring constant itself is dependent upon the shape and dimensions of the cantilever and the material(s) of construction.

2.7.4 Force Calibration

In order to obtain meaningful force measurements, the AFM cantilevers must be calibrated prior to use. There are a number of methods available in the literature to do this, many of which have been assessed by Palacio and Bhushan (2010). These methods cover both the determination of the normal and torsional spring constants, as well as the determination of the lateral signal sensitivity which is required for lateral force measurements. Of the

techniques available for the determination of the normal spring constants, the most prevalent seem to be the Added Mass (or 'Cleveland') method of Cleveland et al. (1993) and the Resonance (or 'Sader') method of Sader et al. (1999). These methods are also of interest as they have been adapted for the determination of the torsional spring constants.

The Cleveland method, involves the addition of spheres of known mass to the end of the cantilever and the measurement of the effect of these spheres on the cantilever resonance frequency (Cleveland et al., 1993). This method makes use of the relationship,

$$M = k_n(2\pi\upsilon_f)^{-2} - m*, \tag{2.67}$$

where M is the added mass (mass of the sphere), υ is the resonance frequency, k is the normal spring constant and m^* is the effective mass of the cantilever (defined as $m* \approx 0.24m_b$, for a rectangular cantilever, where m_b is the mass of the beam).

Then by measuring the resonance frequency for a series of successively increasing sphere masses, a plot of M versus $(2\pi\upsilon_)^{-2}$ is linear, with of slope of k_n. The nature of this method means that it is applicable to cantilevers of all shapes and materials (Green et al., 2004). However, the procedure is rather tedious, risks damaging the cantilever and can be prone to error if the added mass is not properly positioned (Palacio and Bhushan, 2010; Green et al., 2004.

The Cleveland method was extended by Green et al. (2004) to allow the determination of the torsional spring constant. This method utilises the same procedure of adding spheres of known mass to the cantilever as the 'normal' Cleveland method however, in this case it is the radial resonance frequency ω_t of the cantilever that is being measured. Here the effect of adding a sphere, of mass M, is considered in terms of its effect on the mass

moment of inertia, J present at the free end of the cantilever, such that

$$J_s = \frac{7}{5} M r^2 \tag{2.68}$$

(Green et al., 2004). The radial resonance frequency ω_t of a cantilever with an added mass may be described as,

$$\omega_t^2 = \frac{k_\phi}{J + J_e}, \tag{2.69}$$

Substituting Equation 2.69 into Equation 2.68 and rearranging gives,

$$\frac{28\pi\rho_s r^5}{15} = \frac{k_\phi}{\omega_t^2} - J_e, \tag{2.70}$$

where the mass of the sphere is re-expressed in terms of its radius and density (i.e. $M = 4/3\pi r^3$. In this (the torsional) case, $28\pi\rho_s r^5/15$ when plotted against ω_t^{-2} will give a straight line of slope k_ϕ. This technique however, suffers from the same drawbacks associated with the 'normal' Cleveland method (Green et al., 2004; Palacio and Bhushan, 2010).

The Sader method utilises the plan view geometry of the cantilever, with the cantilever resonance frequency (ω_f) and the cantilever quality factor (Q_f. This method is based on the observation that the change in the resonance frequency of a cantilever from when it is in a vacuum to when it is in a fluid, is mainly due to the inertial effects of the fluid (Sader et al., 1999). Therefore, with some manipulation, the normal spring constant may be determined for a cantilever by measuring the values of ω_f and Q_f in the atmosphere in which the cantilever will be used (usually air). The normal spring constant is then,

$$k = 0.1906\rho_f b_c^2 L_c Q_f \Gamma_i(\omega_f)\omega_f^2, \tag{2.71}$$

where ρ is the density of the fluid, b_c is the width of the cantilever, L_c is the

length of the cantilever and $\Gamma_i(\omega_f)$ is the imaginary component of the hydrodynamic function (Sader et al., 1999). Much of the difficulty in evaluating the hydrodynamic function has been removed by Green and Sader (2002), where the authors provide an empirical, analytical expression for the real and imaginary components of the hydrodynamic cantilever for a rectangular cantilever. This was achieved through the use of a non-linear least-squares fitting procedure applied to numerical data (Green and Sader, 2002). The expression for the imaginary component ($\Gamma_i(\omega_f)$) of the hydrodynamic function is,

$$\Gamma_i(\omega_f) = \left(\frac{0.41}{\sqrt{Re}} + \frac{1}{Re}\right)(0.82494\tau - 0.67701\tau + 0.41150\tau^2 - 0.16748\tau^3 + 0.04897\tau^4 - 0.01107\tau^5 + 0.00148\tau^6)(1 - 0.72962\tau + 0.40663\tau^2 - 0.16517\tau^3 + 0.04907\tau^4 - 0.01110\tau^5 + 0.0148^6)^{-1}, \quad (2.72)$$

where Re is the Reynolds number, in this case defined as $Re = \rho\omega_f b_c^2/4\mu$, and $\tau = log_{10}(Re)$ (Green and Sader, 2002).

The 'normal' Sader method has also been modified for the determination of the torsional spring constant by Green et al. (2004). This method was derived in an analogous way to the normal method and requires that L_c is much greater than b which is itself significantly greater than the cantilever thickness (t_c). These criteria are typically satisfied by AFM cantilevers. The torsional spring constant is then,

$$k_\phi = 0.1592\rho b_c^4 L Q_t \omega_t^2 \Gamma_i(\omega_t), \quad (2.73)$$

where the quality factor of the fundamental resonance peak of torsional vibration (Q_t) needs to be much greater than 1 (Green et al., 2004).

Sader (1995) has shown that the variation in the spring constant of a can-

tilever, subject to off end loading (i.e. with a sphere or lever attached) will be identical for rectangular and V-shaped cantilevers. Additionally, Green and Sader (2002) state that their theoretical models are applicable to any cantilever, provided certain criteria are met. For example, the cantilever length should be much greater than its width. Therefore, provided that the cantilever dimensions are appropriate, Equations 2.71 and 2.73 may be applied to V-shaped cantilevers. This assessment is also confirmed by Palacio and Bhushan (2010), who state that these methods are not limited by the geometry of the cantilever.

Having determined the value of k_ϕ, the torsional stiffness (k_{yT}), of the cantilever is then;

$$k_{yT} = \frac{k_\phi}{h^2}, \tag{2.74}$$

where, h is the length of the moment arm subject to the torsional force, such that,

$$h = \frac{t_c}{2} + l_t, \tag{2.75}$$

with t_c being the thickness of the cantilever and l_t being the length of the cantilever tip.

Alternatively, the torsional stiffness may be found directly using the analytical expressions of Neumeister and Ducker (1994), for a triangular (or V-shaped) cantilever,

$$k_{yT} = \frac{k_\phi}{h^2} = \frac{Et}{3\left(1+\upsilon\right)h^2} \times \left(\frac{1}{tan\alpha} log \frac{b_l}{dsin\alpha} + \frac{L_l cos\alpha}{w} - \frac{3sin2\alpha}{8}\right)^{-1}, \tag{2.76}$$

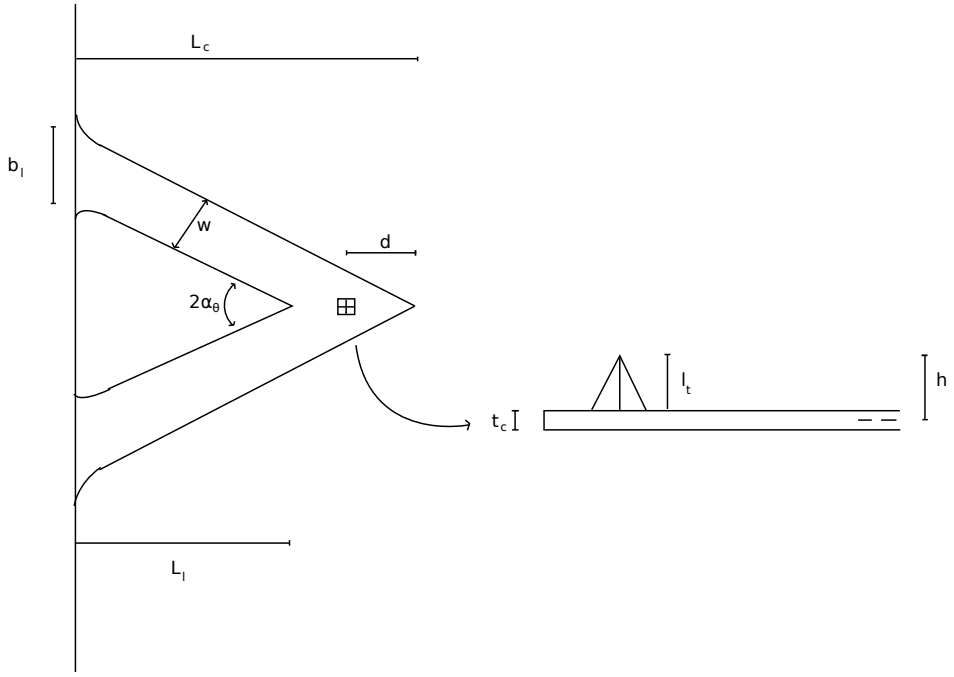

Figure 2.6: Schematic representation of a V-shaped cantilever (not to scale)

where, E is the Young's modulus, υ is the Poisson ratio, b_l is the width of a single cantilever arm at the base, d is the distance from the centre of the tip to the end of the cantilever, α is half the angle between the cantilever arms, L_l is the distance from the base of the cantilever to where the arms meet and w is the width of the cantilever arm at the midpoint. These parameters are shown diagrammatically in Figure 2.6.

Some other techniques include;

- The lateral electrical nanobalance method, where the cantilever tip is scanned both in and out of the nanobalance (Cumpson et al., 2005; Palacio and Bhushan, 2010). This technique obviously requires an appropriate nanobalance.
- The diamagnetic levitation spring method, which involves the use of

magnets to induce levitation in a graphite sheet and measuring the displacement of the cantilever tip that is in contact with said graphite sheet (Palacio and Bhushan, 2010). This method requires the use of additional equipment and materials.

- The lever method, where a fibre and sphere is attached to a cantilever and the resulting angular deflection of the cantilever is measured (Feiler and Larson, 2000; Palacio and Bhushan, 2010). This method requires that the fibre and sphere be attached to each cantilever, for the calibration and then removed. Given the nature of this method is it applicable only for tipless cantilevers.

To achieve the lateral force calibration the lateral signal sensitivity (s_{lat}) must also be determined. A calibration factor (α_f) can then be determined, such that;

$$\alpha_f = \frac{k_{yT}}{s_{lat}}. \tag{2.77}$$

There are a number of methods available for the determination of the lateral signal. These methods do, however, tend to be quite tedious and generally require the use of additional materials. The commonly used wedge method of Ogletree et al. (1996) requires the use of sloped surfaces of known gradients. The cantilever tip is then moved over the sloped surface and the lateral signal is expressed as a function of applied load. Alternatively, the lever method of Feiler and Larson (2000) can be used. This method involves the measurement of both the vertical and lateral deflection of the cantilever, that has a lever attached. Both the wedge and lever methods, however, require that each and every cantilever is calibrated in the respective manner.

Liu et al. (1996) determined the value of s_{lat} through the use of an optical method. This involves measuring the distance from the cantilever to the detector and also the size of the detector and the material properties of the cantilever. However, this measurement may be difficult to perform in practice.

The method of Meurk et al. (1998) does not involve the use of a cantilever at all. This method involves reflecting the laser off a small sample that has a reflective area that is smaller than the laser spot. The lateral voltage signal is then recorded as the sample is tilted at different angles. While this method seems simple, a mathematical correction is required to account for the motion of the cantilever on a surface, this is a function of the probe height. This method does however seem to disregard lateral in-plane bending of the cantilever and so may not be appropriate if cantilevers of different sizes are used.

The test probe method of Cannara et al. (2006) offers a significant advantage over the lever and wedge methods in that the procedure only needs to be performed on a single test probe. The method involves measuring the lateral deflection of the cantilever as it is pushed against a piece of Gallium Arsenide (chosen as it cleaves at a perfect 90° angle (Cannara et al., 2006)). This provides the s_{lat} value for the test cantilever which may then be converted for any other cantilever used in the AFM, through the use of the formula;

$$s_{lat,target} = s_{lat,test} \frac{(Ts_{target}/Ts_{test})}{(h_{target}/h_{test})} \frac{(1+\epsilon_{test})}{(1+\epsilon_{target})}, \tag{2.78}$$

where h is the torsional moment arm length, Ts is the total signal, ϵ is the lateral in plane bending and the subscripts *test* and *target* identify the test cantilever values and the target cantilever values, respectively (Cannara et al., 2006).

Generally, the lateral force calibration of the cantilevers is a two step procedure, with the individual methods for the torsional spring constant and the lateral signal sensitivity being chosen based on their accuracy and their ease of application.

2.7.5 Applications to Fibrous Filtration

The way in which liquid droplets interact with fibres is of particular importance in the field of liquid aerosol filtration. The force required to detach these droplets and the way in which they detach has received relatively little attention (Mullins et al., 2007b). Examination of the extension of droplets from their preferred position on a fibre, and the force required to detach them completely from the fibre, provides information on the interfacial tension between fibres and droplets (Mullins et al., 2007b). An understanding of fibre droplet interactions may provide an insight into re-entrainment behaviour. Thus far only one work has examined droplets on filter fibres using the AFM; that of Mullins et al. (2007b).

The measurement of these forces may be achieved through the use of an atomic force microscope (AFM). This method has been used successfully to measure the force required to both pull barrel shaped droplets away from filter fibres and to remove them completely (Mullins et al., 2007b).

In their work, Mullins et al. (2007b), present a model that describes the force required to pull a barrel shaped droplet away from its axisymmetric location. This model determines a restoring force, F_r, such that:

$$F_r = 2\sigma \int_0^{2\pi} \frac{r_f cos(\psi) \sqrt{r_f^2 + \frac{(x_a^2 r_f cos(\psi))}{z_A^2}}}{\left[r_f^2 + \frac{\left((x_a r_f cos(\psi) + r_f^2)^2 \right)}{z_A^2} \right]} d\psi \tag{2.79}$$

Where ψ is the angular position of the contact line around the fibre, x_a is the distance from the axisymmetric rest position to the droplet mass centre and z_A is the z component of the position vector r_A.

2.8 Computational Fluid Dynamics

Physical systems (such as mist filters) can be modelled, to a fair degree of accuracy, using partial differential equations. These equations however, are usually quite complicated and cannot be solved analytically. Computational fluid dynamics (CFD) provides a means of finding solutions to these equations for a given system. This involves applying appropriate boundary conditions, discretising the model equations, and solving the resultant equations (usually iteratively) for each point in time and space.

The flow of fluid through a filter was briefly mentioned in Section 2.2, where the Navier-Stokes equations (Equation 2.2 and 2.4) were given. These are the fundamental equation describing fluid flow. The derivation of the equations governing fluid flow are discussed in detail by (Versteeg and Malalasekera, 2007). For reasons of clarity, it may be better to re-express Equation 2.4 in terms of the x,y and z components of the momentum, such that;

$$x - momentum \qquad \frac{\delta \rho u}{\delta t} + \bigtriangledown (\rho u \mathbf{u}) = -\frac{\delta p}{\delta x} + \bigtriangledown \left(\mu \bigtriangledown^2 u\right) + S_{Mx}, \quad (2.80)$$

$$y - momentum \qquad \frac{\delta \rho v}{\delta t} + \bigtriangledown (\rho v \mathbf{u}) = -\frac{\delta p}{\delta y} + \bigtriangledown \left(\mu \bigtriangledown^2 v\right) + S_{My}, \quad (2.81)$$

$$z - momentum \qquad \frac{\delta \rho w}{\delta t} + \bigtriangledown (\rho w \mathbf{u}) = -\frac{\delta p}{\delta z} + \bigtriangledown \left(\mu \bigtriangledown^2 w\right) + S_{Mz} \quad (2.82)$$

where,

$$\bigtriangledown \mathbf{u} = \frac{\delta u}{\delta x} + \frac{\delta v}{\delta y} + \frac{\delta w}{\delta z}, \quad (2.83)$$

and S_{Mx}, S_{My} and S_{Mz} are the momentum sources in the x, y and z directions, respectively.

Solutions to these equations are found numerically by applying appropriate boundary conditions and discretising the partial differential equations

(PDEs) into linear or non-linear algebraic equations, that can be solved iteratively.

2.8.1 Discretisation

In order to evaluate the chosen mathematical model numerically, it is necessary to 'discretise' the continuous equations into a form that may be solved numerically. In CFD, this discretisation is achieved by selecting an appropriate method to approximate the differential equations (e.g. Equations 2.2, 2.80, 2.81 and 2.82) using a system of algebraic equations at a set of discrete time and spatial locations (Ferziger and Peric, 2002). There are three methods available for the discretisation of the partial differential equations, the finite difference method, the finite volume method and the finite element method.

- The finite difference method involves the use of either Taylor series expansions or polynomial fits to approximate the derivative terms in the model equations. These approximations are applied at each grid point and thus this method provides a simple means of discretisation. However it is restricted to use with simple geometries and does not inherently preserve the conservation equation, so some care is needed when this method is employed (Ferziger and Peric, 2002).

- The finite element method involves breaking up the solution domain into discrete volumes (finite elements). This method involves the use of weighted residuals to simplify the second order terms to first order terms. The solution is then found in terms of a shape function. These approximations are then substituted into the integral form of the conservation equation, with the discretised equations obtained by requiring the derivative of the integral to be zero (Ferziger and Peric, 2002). The result is a set of non-linear algebraic equations. The main drawback associated with finite element methods is that sometimes it is difficult

to find an efficient solution method (Ferziger and Peric, 2002).

- The finite volume method involves the division of the solution domain (i.e. the geometry over which the PDEs are being evaluated) into smaller control volumes. The method considers the integral form of the conservation equations, which are applied to each control volume. The variables are calculated at each node (located centrally in each control volume) with interpolation methods employed to determine the value of each variable at the control volume surface. The finite volume method requires approximation at three levels, interpolation, differentiation and integration (Ferziger and Peric, 2002). The advantage of this method is that (if used correctly) the conservation equations are inherently preserved.

The finite volume method is the most frequently used discretisation method in CFD, as it can be applied to complex geometries. Using this method, the discretisation yields a number of control volumes, each with a centrally located computational node. The solutions to the discretised system of equations are therefore the values of the variables at each node. However, to ensure adherence to the conservation laws the flux in and out of each control volume needs to be evaluated. For this reason, the surface and volume integrals describing each control volume must be approximated. In order for these approximations to take place, the values of the variables must be known at the faces of the control volumes; these are found via an interpolation method.

The chosen discretisation method will result in a set of linear or non-linear algebraic equations, which will essentially be a matrix. The matrices resulting from the discretisation of PDEs are sparse and in the case linear systems may be solved directly through the use of Gaussian elimination or Lower Upper (LU) decomposition methods. However, the triangular factors of sparse matrices are not sparse and therefore direct solution of the matrices may not

be computationally efficient (Ferziger and Peric, 2002), or necessary. Given that there is an error associated with the discretisation, solving the algebraic equations exactly is not so important, they only need to be evaluated to a higher level of accuracy than the discretisation error. Therefore an iterative solution method is employed for both linear and non-linear equations that result from the discretisation.

2.8.2 Pre-Conditioning

Greater solution efficiency can be achieved by an iterative solver, but only if the initial approximation of the solution is close to the final solution. Therefore by pre-conditioning the matrices before the iteration process, there may be a significant improvement in computational efficiency. Additionally, the use of pre-conditioners can make the iterative solver more robust (Chapman et al., 2000). There are a number of pre-conditioning methods available, the selection of which is somewhat dependent upon the system being modelled.

So for a system of linear equations, where;

$$A\phi = B, \tag{2.84}$$

and A is a sparse $n \times n$ matrix (resulting from the discretisation procedure) and B is the matrix we are solving for; the iterative solution may be achieved faster by using a preconditioning matrix, M, such that;

$$MA\phi = MB. \tag{2.85}$$

Where, M, is non-singular and in some way approximates A. Here Equation 2.85 will have the same solution as Equation 2.84, but it will be reached more rapidly. M is usually the result of an incomplete factorisation of A, and there are a number of methods on offer, which have been thoroughly reviewed by

Benzi (2002). Commonly encountered methods are the incomplete Cholesky method, for symmetric matrices (Meijerink and van der Vorst, 1977) and incomplete LU method for asymmetric matrices (Chapman et al., 2000; Benzi, 2002).

2.8.3 Solution Methods

There are a number of algorithms that have been developed to solve equations for pressure, momentum, volume of fluids, particle tracking etc, which may be used in-conjunction with each other to solve for all the variables of a given system. All of these methods make use of iterations to achieve the desired level of accuracy, as well as the efficient use of computational resources.

Such an iterative system can be described by;

$$A\phi^n = B - \rho_r^n, \tag{2.86}$$

where, n is the number of iterations and ρ_r is a residual term. Successive iterations, should adjust the residual term towards zero, such that when $\rho_r = 0$, Equation 2.86 has the same solution as Equation 2.84.

Typically, the iterations are run until a pre-determined level of accuracy is attained before the calculation is advanced by the next time-step. This is convergence, where as a result of the iterations the residuals converge towards the pre-determined criteria. This forms the basis of a stable iteration process and therefore, ultimately dictates the solution of the equations. There are a number of factors involved in ensuring the stability of a simulation and hence, convergence.

A key factor in the stability of simulations is the Courant-Friedrichs-Lewy (CFL) condition, originally described by Courant et al. (1928), where;

$$\frac{u\Delta t}{\Delta x} <= c, \tag{2.87}$$

with u, a velocity (i.e. geometric space travelled in relation to the time-step), Δt, the time-step, Δx, the length interval (i.e. the distance the calculation is advanced) and c, a simulation specific constant. It is essentially a measure of the number of mesh cells that are advanced through per time-step. To ensure stability the term before the inequality in Equation 2.87, or the Courant number, should be no greater than 1 (for 1 Dimensional systems and approximately 0.5 and 0.3 for 2 and 3 dimensions, respectively). Therefore the mesh size and the time-step size are dependant upon each other and this must be considered when constructing the simulation.

In order to attain stability in the simulations, a method known as under-relaxation is commonly used. This is a procedure that limits the change in variables between iterations, such that the variable in question is only changed by a fraction of the total change determined by the solution algorithm;

$$\phi^n = \phi^{n-1} + \alpha_\phi \left(\phi^{new} - \phi^{n-1}\right), \tag{2.88}$$

where α_ϕ is the relaxation factor, ϕ^n is the under-relaxed solution and ϕ^{new} is the solution obtained directly from the solution algorithm (Ferziger and Peric, 2002).

The solution algorithms used will be dependent on the nature of the system being modelled and will need to be applied in a specific order, as finding a solution for a particular variable may depend on having already solved for some of the other variables. If one considers solving for pressure and momentum, it becomes clear from examination of Equations 2.80 - 2.82, that one cannot be solved without the other. Furthermore if the flow may be considered incompressible (which it can be for fibrous filters, as the Mach number is $<< 0.3$) then the pressure gradient is not related to the density, as the density is constant Versteeg and Malalasekera (2007).

Therefore a solution algorithm is required that allows the solution of coupled variables (i.e. pressure and momentum). There have been several methods developed to allow the solution of the coupled pressure and momentum variables, the most common being the Semi-Implicit Method for Pressure Linked Equations (SIMPLE) of Patankar and Spalding (1972) (and its variants) and the Pressure Implicit with Splitting of Operators (PISO) algorithm of Issa (1986). These methods start with an estimation of p, which is used in the discretised equations to find u, v and w. This is followed by a corrector step, where a correction is applied to p and the corrected value of p is used to find the corrected values of u, v and w. The difference between the SIMPLE and PISO algorithms is that the PISO method uses an additional corrector step. A detailed description with examples of these algorithms is given by Versteeg and Malalasekera (2007).

Additional methods are required for solving for other variables, so depending on the nature of the simulation, several other algorithms may be required. In the case where there are two immiscible fluids present in the flow, an additional algorithm will be required to handle them; this is the Volume of Fluid (VOF) method of Hirt and Nichols (1981). This differs from other solution methods in that it must handle free boundaries (e.g. the surface of a droplet of one fluid that is bounded by another fluid). As these boundaries are not fixed and are subject to movement and deformation, the algorithm must be able to adjust this free boundary. Given that there is a clear boundary (i.e. either there is or isn't a particular fluid at a given location) techniques that act to average or interpolate variables across computational cells, will clearly be inappropriate, as they will not have a clearly defined free boundary. The VOF method circumvents this by taking the 'average' value and treating it as the fraction of the fluid in the cell, the free boundary is then normal to the direction where the fraction of fluid in the cell changes the most (Hirt and Nichols, 1981).

Often simulations will contain discrete particles, for example, simulations

of aerosols and sprays. This requires a particle tracking algorithm that is capable of tracking the motion and location of each individual particle through the flow. In simple geometries, particle tracking is relatively simple and may be achieved by moving it along its calculated trajectory, to new location in a new cell. However, in more complicated geometries (i.e one with a mesh of unstructured polyhedral cells), this process will require a search of the mesh to find the new cell where the particle is located (Macpherson et al., 2009). This search can be time consuming and may prevent the efficient computation of a solution, thus an alternative method is needed.

The particle tracking algorithms of Zhou and Leschziner (1999), Chen and Pereira (1999) and Chorda et al. (2002) all take a similar approach to determining where the particle trajectory intersects a cell boundary. Each boundary is systematically checked moving around the cell boundary. The algorithm of Zhou and Leschziner (1999) stops searching once it finds the boundary that has been intersected and immediately considers the neighbouring cell (that shares the boundary), whereas the algorithms of Chen and Pereira (1999) and Chorda et al. (2002) complete the check before progressing. The algorithm of Chorda et al. (2002) is more computationally efficient in 3D systems as it searches for the cell face where the intersection occurs; while the algorithm of Zhou and Leschziner (1999) requires that the face where the intersection occurs be divided until all the vertices of this sub-face lie on the same plane.

All three of these algorithms however, contain a flaw, whereby any trajectory that intersects a vertex could result in the particle being assigned to the wrong cell (Macpherson et al., 2009). This occurs as the algorithms essentially have to guess which cell the particle will move to and as such a particle may be place in a cell that is inconsistent with its position. This can cause the calculations to stop, become unstable and the particle tracking algorithm could fall into an infinite loop.

These issues are avoided by the particle tracking algorithm presented by

Macpherson et al. (2009), which considers not only the starting position of the particle (like the other algorithms) but also the centre of the cell. Any face then that is intersected is calculated based on both the node of the original cell and the original position of the particle, which allows the cell that the particle enters to be correctly identified. Additionally, this algorithm stores the particle location data so that at the beginning of the next step step that particles do not have to be found. It is the particle tracking algorithm of Macpherson et al. (2009) that is implemented in the OpenFOAM CFD package.

2.8.4 Boundary Conditions

Boundary conditions are, as the name implies, a set of conditions imposed on the system at the physical boundaries, i.e. the inlet, outlet, internal walls and so forth. These conditions are imposed on the cells that form the boundary and are incorporated as a source term modification in the discretised equation for these cells. As such, these conditions must be carefully applied as they can significantly affect the stability of the simulation. Commonly applied boundary conditions include, specification of the flow field at the inlet, specifying a flux at a solid wall and defining a boundary as an outlet (where the flow can 'leave' the geometry).

2.8.5 CFD Packages

A number of software packages have been developed to perform computational fluid dynamics calculations. The majority of these are commercial products, (e.g. FLUENT, StarCCM, ANSYS-CFX) which are able to handle a wide range of simulations, and are used extensively in industry and academia. The drawback is that being commercial software, there are annual license fees involved, which can make CFD a costly exercise, particularly if simulations need to be run in parallel over a large number of CPUs.

There are also some open source CFD software packages available, such as the Open Field Operation And Manipulation (OpenFOAM) package produced

by OpenCFD Ltd, which have the advantage of being open source; but may require a greater level of user involvement. The choice then, of which CFD package to use will then most likely be based on what one has access to and how suited it is to the simulation being run.

2.8.6 Applications to Fibrous Filtration

A small number of studies have been conducted using a computational fluid dynamics approach to fibrous filtration. These have predominantly focussed on modelling the flow through media to examine the effects of fibre orientation (Fotovati et al., 2010), the influence of bimodal fibre diameter distributions (Tafreshi et al., 2009) or for modelling filter permeability (Jaganathan et al., 2008b). A few have also modelled filter pressure drop (Jaganathan et al.. 2008a; Qian et al., 2009) through such media and some the loading of a single fibre (Lehmann and Kasper, 2002). All these works however have either purely focussed on the flow alone, or the flow and the capture of solid particles, none have considered liquid droplets and coalescence.

Qian et al. (2009) used CFD to examine the influence of filter face velocity, packing density and particle sizes on filter pressure drop and capture efficiency. However they did not use realistic filter geometries, but instead a series of parallel cylinders analogous to the systems examined by Kuwabara (1959) and Happel (1959). Additionally, there was some discrepancy between values predicted by SFE theory and simulated values. For particles less than 500 microns in diameter this may be due to most versions of Fluent having difficulty with the implementation of the equations for Brownian motion (Mullins pers. com(2009); Hosseini and Tafreshi, 2010). For particles greater than 500 microns in diameter, the capture efficiency is under-predicted, this is most likely the efficiency by interception; which may be due to the size of the mesh used. Since particles are centrally tracked, the solver only tracks where the centre of each particle is. If the mesh is too fine (i.e. smaller than the diameter of a particle) it is possible that the centroid of a particle will be in a cell that is not adjacent to a fibre and so will not be 'collected' even

though the edge of the particle is actually in contact with the fibre.

Lehmann and Kasper (2002) examined the collection of particles on a single fibre, by implementing user defined functions (UDF) to account for previously collected particles and to determine the probability of a particle adhering to previously collected particles. This work, however, focussed on solid particles and the simulation of dendrite formation, which does not occur when the aerosol particles are liquid droplets. Lehmann and Kasper (2002) did, however account for the diameter of each particle.

Perhaps the most thorough CFD based work on fibrous media is that of Jaganathan et al. (2008b), here the authors present a means of imaging fibrous media, so that geometries of actual media can be used in the simulations (similar work was also done by Lehmann et al. (2005)).This technique does however involve many steps, and there is a possibility of altering the media during imaging or image processing. In any event, this is less important than the simulations themselves, which simulated the permeability of the fibrous media. This work also demonstrates the viability of using an imaging technique to create actual filter geometries, on which CFD simulations can be run.

Fotovati et al. (2010) used CFD simulations to examine the effects of fibre distribution and orientation on the performance of a fibrous filter. This was primarily done by examining the filter capture efficiency. In the works of both Fotovati et al. (2010) and Hosseini and Tafreshi (2010), user defined functions (UDFs) are implemented in Fluent to correct deficiencies in the implementation of Brownian motion and also to correct for collection via interception. The simulation of particle motion is achieved by using the inbuilt Discrete Phase Model (DPM) in Fluent as well as the UDF, where an Eulerian approach is taken to the motion of particles smaller than 100nm. The drawback here is that these small particles are no longer individually tracked, but are tracked as a 'cloud' of particles (i.e. as volume fractions within the computational cells). This then requires some criteria to be set to indicate when these particles are captured, in terms of what volume fraction

in a cell results in particles being considered captured.

2.9 Summary of Literature

While liquid aerosol filtration has received much attention, there remain significant gaps in the literature, which require further study. Section 2.5 has presented several models for ΔP, η_T and S_e in mist filters, but has also highlighted the limited applicability of such macro-scale empirical approaches. Therefore, there is a need for a more fundamental approach to be taken.

The key gaps identified in the literature are considered to be:

- Capillarity in mist filters is a significant feature, which may prove useful for modelling such systems via capillary theory.
- The AFM provides a practical tool, suited to accurate micro-scale measurements of fibre systems.
- The rapid development of computational performance means that CFD can offer an alternative to long term experiments and the associated empirical expressions (after full validation of any models).

This work aims to fill these gaps by:

- Applying capillary theory to mist filters to model equilibrium saturation.
- Developing a method using the AFM to measure the force required to move a coalesced liquid droplet.
- Developing and validating a theoretical model to describe the force required to move liquid droplets along fibre.
- Measuring the force required to move both axisymmetic and 'clamshell' shaped droplets.
- Describing the development of a CFD solver for droplet fibre systems.

- Validating the CFD solver using existing theory in the literature and the results of the AFM measurements.

3 Research Case

As was illustrated in Chapter 2, there is still much work to be done in terms of modelling the behaviour of fibrous mist filters. The currently available models are largely empirical in nature and typically only applicable over a narrow range of parameters. Furthermore, they may only work for either clean filters or saturated filters, as modelling the dynamic processes that lead to saturation would be exceedingly difficult. Therefore, much potential for further work can be demonstrated. What is needed is a better understanding of some of the micro-scale processes which occur inside filters, as ultimately it is these processes that will be responsible for the macro-scale behaviour of the filter (e.g. pressure drop, saturation, drainage rate). The work herein will focus on the examination of the micro-scale liquid coalescence and transport processes that take place in filters capturing liquid aerosols.

Given the complex nature of the structure of mist filters, they will generally be examined not as a whole, but in smaller components. The results will then be examined and applied to the whole filter. This is much like the approach taken when the single fibre efficiency theory was developed, and has indeed been shown to be an effective approach. In this work, filters and filtration processes will be examined at a single fibre scale, or a slightly larger scale, such as that of a capillary. The capillary approach appears to be more limited in scope and so shall be examined first.

Filter saturation itself can be examined in the micro-scale, by studying the behaviour of a theoretical capillary. It was shown in Section 2.5.5 that fibrous filter media behaves, in general, like a series of capillaries and that it is possible to apply capillary theory to filter media. This could potentially be used to allow the equilibrium saturation of a filter to be determined using a modified capillary theory. This will be discussed in **Chapter 4**.

It is evident from Section 2.4 and the literature that there is very little information available on the behaviour of droplets on fibres. Given that the

filter saturation and drainage will be directly influenced by this behaviour, any attempt to describe the macro-scale properties of the filter must at the very least be based on an understanding of how coalesced droplets on fibres behave.

The atomic force microscope (AFM) provides a means to study coalesced droplets on fibres. If a relationship between the force required to move a droplet and the oil-fibre combination used an be found, it will be possible to predict, on this basis when, drainage is expected to occur, or at least the micro-scale criteria that must be met in order for drainage to occur. Such measurements will require a method to be developed to allow the force required to move a droplet on a fibre to be measured. The development of such a method will be detailed in **Chapter 5**.

Using a single fibre approach, the force required to move a coalesced liquid droplet will be evaluated and modelled. The measurements will consider, different, oils and different fibre materials and look at both axisymmetric and 'clamshell' droplets. These measurements and related models, will be detailed in **Chapters 6 to 8**. Additionally, this will provide validation data for a computational fluid dynamics model, that will first aim to simulate both single fibre (wetting) processes and transport processes (on a micro and macro-scale).

The force required to move coalesced liquid droplets containing particulate contaminants (such as soot) will also be examined in **Chapter 8**. This will provide information on the behaviour of mist filters when exposed to contaminants.

Given the complexity of fibrous filters and the various issues associated with using the models currently available, it is perhaps better to simulate their behaviour. This will be more computationally intensive than using an analytical model, however it is very likely that, as seen in Chapter 2, the behaviour of a particular fibrous filter will not be able to be predicted, if it has not been

used (or is not sufficiently similar to the filters used) in the development of the (empirical) models. Additionally, the real-time taken to simulate filter behaviour must only be less then the time that would be required to fully test a filter to make it useful. Furthermore, it should be noted that computational speed is continually improving.

Using computational fluid dynamics (CFD), it should be possible to simulate the behaviour of coalescing droplets. This potentially removes the issue of transition points between the different stages of filtration, as instead of using an empirical equation, the CFD model will simulate the filter and all the processes that go on within the filter. Therefore if one were interested in the transition points they could be determined by analysis of a completed simulation. This may be of interest practically (i.e. so that industries know what to expect in terms of a pressure drop profile), but would be unnecessary theoretically as the use of the empirical equations would no longer be necessary. However, CFD could also be used, ultimately to develop simpler theoretical models, much like those described in Chapter 2.

CFD models must of course validated. This could be done by examining different aspects of filter behaviour individually and comparing them to the relevant theory or experiments. So, the predicted capture efficiency can be compared to that determined using the single fibre efficiency theory, the implementation of the Plateau-Rayleigh Instability could be compared with the maximum film thickness determined using Equation 2.18. The simulated behaviour of large volumes of fluid could be examined by comparison to the liquid distribution in 'real' filters. The development and validation of the CFD model/solver will be discussed in **Chapter 9**.

In summary, this thesis will

- Examine the use of capillary theory, in order to model/predict filter behaviour.
- Extensively study droplet-fibre relationships, using the AFM and ex-

amine these relationships within the context of mist filtration.

- Detail the development and validation of a CFD solver for mist filters.
- Use the CFD solver to model realistic filter geometries and 'real' world filters.

4 Predicting Filter Saturation Using a Capillary Based Model

4.1 Introduction

It has been shown in detail in Chapter 2, that there are a number of unresolved issues in relation to the behaviour of mist filters. This is because they differ significantly in their behaviour to dust filters, where the system is much better understood. The lack of knowledge that is present in the field of liquid aerosol filtration is predominantly due to the ability of the aerosol droplets to coalesce (into larger droplets, liquid columns and arrays of droplets) within the filter, and then to drain from or flow through the filter (which itself is a porous media with a complex structure) under the influence of airflow and gravitational forces.

The presence of the collected liquid in the filter greatly increases the pressure drop of the filter, and (in most cases) has been found to decrease the filtration efficiency, (especially in the diffusional capture regime) (Letts et al., 2003). Therefore the accumulated liquid content of a mist filter is of paramount importance, as the saturation influences both pressure drop and collection efficiency. The saturation (S), as defined in Equation 2.1 is especially critical, since most filter systems operating in stable flow and mass loading conditions will attain a "pseudo"-steady-state; as described in Section 2.1. The effect of decreasing the equilibrium saturation (S_e), which is simply the saturation when the "pseudo-"steady-state is attained, will then (usually) be to increase efficiency and decrease pressure drop.

The most thorough treatment of equilibrium saturation thus far has been that of Raynor and Leith (2000), see Section 2.5.2, where empirical equations were derived to allow the prediction of not only saturation but also pressure drop and efficiency. While this work represents an important step forward, it has since been found that Equation 2.27 is only applicable to filters similar to those used by Raynor and Leith (2000), i.e. low packing

density, thick media, composed of fibres several microns in diameter. Such filters are not representative of the media used in many modern mist filter systems, which commonly use multiple layers of thin micro fibre glass media (with fibre diameters often an order of magnitude lower than that used by Raynor and Leith (2000)) or stainless steel media. The main issue being that the equilibrium saturation is much more dependant on velocity than indicated by Equation 2.27.

Previous work by Mullins et al. (2007a) has shown that when some commonly used fibrous (mist) filter media are permitted to imbibe liquid (from a reservoir), they behave in a similar manner to a traditional system of vertical capillaries. An additional study (Mullins and Braddock, 2011) examined forced immersion/withdrawal of such media into/from a liquid (oil) bath, and found that such systems could be described by applying a pressure gradient between the top and bottom of the "capillary" (fibrous media), as is commonly applied in other capillary applications. Yet further work, has found that in modern filter media, altering the airflow velocity acts on saturation in a similar manner to providing a pressure gradient above/below a capillary (increasing airflow velocity decreases S_e and vice versa - at a much greater rate than predicted by Equation 2.27).

Therefore it should be clear that capillary theory is suitable and appropriate to describe the imbibation of liquid into fibrous filter media when it is in a static state (i.e. without airflow). Also, since the behaviour of an operational mist filter appears to adhere to the general relationship of a capillary system, it should be possible to apply a capillary-based model to determine the capillary rise height in fibrous media whilst air is flowing through the filter. This then will be used to determine the steady-state (equilibrium) saturation of the fibrous filter.

4.2 Capillary Model

It has been observed previously (Mullins et al., 2007a), (Jaganathan et al., 2009) that the imbibation of liquid by wettable fibrous filter media under a static (no airflow) condition may be fully described using capillary theory (usually assuming a single "effective" capillary size for the entire media).

Previous work (Mullins et al., 2007a) determined that, when the Washburn capillary model is used, the effective capillary radius (r_c) can be determined using an empirical function of packing density and fibre radius (r_f). Such that r_c may be described as,

$$r_c = -Aln\left(\frac{\alpha}{r_f}\right) - B, \tag{4.1}$$

where A and B are material dependent constants (Mullins et al., 2007a).

The modified Washburn equation can be written in the following form to incorporate a pressure gradient at the top and bottom of the capillary,

$$\frac{d\left(A_c\rho\left(x-x_b\right)\frac{dx}{dt}\right)}{dt} = \left(P_a - P_0\right)A_c - A_c\rho gx + C\sigma cos\left(\theta\right) - 8\pi\mu\left(x-x_b\right)\frac{d\left(x-x_b\right)}{dt}, \tag{4.2}$$

where A_c is the cross-sectional area of a capillary, ρ is the density of the liquid, σ is the liquid surface tension, g is acceleration due to gravity, θ is the contact angle, P_a is the pressure acting on the liquid surface, P_0 is the pressure acting on the liquid within the capillary, x is the height of liquid in the capillary and x_b is the height of the capillary that is immersed in liquid.

Once equilibrium has been reached, Equation 4.2 reduces to,

$$x_\infty = \frac{-\Delta Pr_c + 2\sigma cos\theta}{r_c\rho g}, \tag{4.3}$$

where x_∞ is the equilibrium capillary rise height and ΔP is the pressure differential between the top and bottom of a vertical capillary. The value of x_∞ can be converted to an overall filter saturation (S or Se) if the geometry of the filter is known. This calculation assumes that all liquid is contained within these theoretical capillaries, and that droplets or films above this fully wetted zone may be neglected. The model assumes that the pressure differential is between the top and bottom of the capillary.

In order to use the capillary model to predict the equilibrium filter saturation there needs to be a way to correlate the filter pressure drop with the pressure difference over a single capillary. For convenience the pressure drop through a single theoretical capillary shall be termed the equivalent pressure drop, ΔP_E, i.e. the pressure drop through said capillary, which is correlated (or 'equivalent') to the pressure drop through the filter.

Therefore, Equation 4.3 can be rewritten in terms of ΔP_E, such that;

$$x_\infty = \frac{-\Delta P_E r_c + 2\sigma cos\theta}{r_c \rho g}, \tag{4.4}$$

with

$$\Delta P_E \approx \omega \Delta P, \tag{4.5}$$

where ω is a dimensionless equivalency factor which relates the measured pressure drop between the upstream and downstream sides of the filter to the pressure differential between the top and bottom of the theoretical capillary within the filter.

As the system being modelled is in reality a highly porous media (being simulated as a system of vertical capillaries), the theoretical capillary needs to relate to a "real" capillary within the filters. Examination of the force balance over a capillary at the steady state shows,

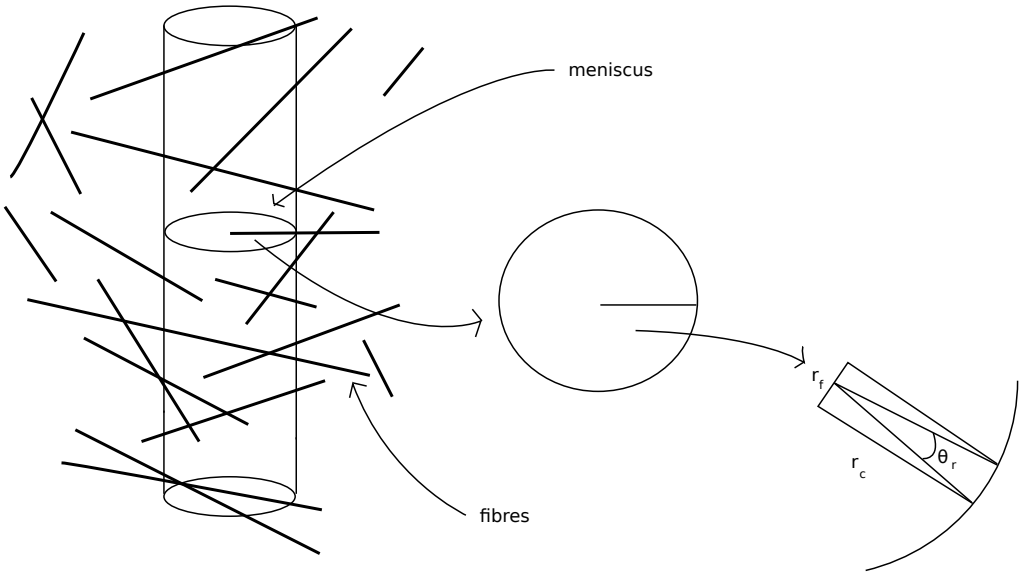

Figure 4.1: Diagrammatic representation of a cylinder (or theoretical capillary) imposed within the filter media; showing the wetted perimeter when a fibre penetrates at the height of the meniscus

$$\Delta P A_c + A_c \rho g x_\infty - C\sigma cos\theta = 0 \tag{4.6}$$

where A_c is the cross-sectional area of the capillary. Equation 4.6 may also be expressed in terms of the pressure drop ΔP,

$$\Delta P = \frac{-A_c \rho g x_\infty + C\sigma cos\theta}{A_c}, \tag{4.7}$$

or substituting πr_c^2 for A_c,

$$\Delta P = \frac{-\pi r_c^2 \rho g x_\infty + 2\pi r_c \sigma cos\theta}{\pi r_c^2}. \tag{4.8}$$

Examination of Equation 4.6 reveals that there are two potential variables where deviations from the ideal case (as in the difference between a true capillary and a theoretical 'capillary') may manifest. Firstly, A_c, is dependent on r_c; which in the case of fibrous filters can be described as a function of r_f. The second variable is the wetted perimeter (C).

If a cylinder is visualised within the filter media, it will contain a mixture of

free space and fibres, with a packing density comparable to that of the whole filter. At x_∞ the meniscus is described by $C\sigma cos\theta$, for a capillary tube. C is simply the wetted perimeter (such that $C = 2\pi r_c$). However in the case of the theoretical capillary (or cylinder) within the filter media, there will exist fibres which penetrate the cylinder. Taking the simple case of a horizontal fibre penetrating halfway into the theoretical capillary, as illustrated in Figure 4.1, we can begin to account for the difference in C between the two cases.

There are of course many possible configurations here, given the random orientation of fibres in mist filters. The case illustrated in Figure 4.1 is chosen for its inherent simplicity; of course one could consider a number of other scenarios; some of which will be mentioned here briefly.

Another model which could be considered is a slice through the cylinder from bottom to top of the meniscus, of height h_c and radius, r_c. This will have a volume (V_{cs}) of

$$V_{cs} = \pi r_c^2 h_c. \tag{4.9}$$

The volume of filter fibres in this volume will then be

$$\pi r_f^2 L_f = \pi r_c^2 h_c, \tag{4.10}$$

where L_f is the length of fibre to equate the volume. If the fibre is flat and lies half way into the meniscus, the wetted perimeter is

$$C = 2\pi r_c + (2L_f + 4r_f), \tag{4.11}$$

where the first term is the circumference of the capillary, and the next two terms are the wetted parts of the fibre along its length, and across the ends. This could be expected to represent an upper value for the circumference, as

it only uses a horizontal orientation of the fibre.

Considering then a fibre at angle β to the horizontal, which cuts the horizontal with a cross section of elliptical form, with axes of r_f and $x = r_f/sin(\beta)$. This would require the determination of the circumference of an ellipse, which is described by the integral,

$$C_e = 4r_f \int_0^{\pi/2} \left(\left(\frac{cos(\phi_x)}{sin(\beta)} \right)^2 + (sin(\phi_x))^2 \right)^{\frac{1}{2}} d\phi_x, \tag{4.12}$$

where ϕ_x is the angle in the fibre from the x axis in normal polar coordinates. This is an elliptic integral, and for $\beta = \pi/2$, this reduces to the circle and gives the correct circumference.

This case is however problematic, as Equation 4.12 cannot be solved analytically. It would also need to integrated over β to account for all random orientations, and multiplied by the number of fibre crossings of the meniscus volume. While it would be optimal to include all possible permutations in the model, it is evident that it would become extremely complex. Therefore it is the simplest case that will (initially) be explored to see what agreement with the experimental results can be achieved.

Considering then a single fibre oriented horizontally, as illustrated in Figure 4.1, the value of C may be described as,

$$C = 2\pi r_c - \theta_r r_c + 2r_f + 2(r_c^2 - r_f^2)^{\frac{1}{2}} \tag{4.13}$$

where θ_r is the angle in radians which defines the arc of the cylinder cross section which is occupied by the penetrating fibre. When the cross sectional area of the capillary is compared to the cross sectional area of a single fibre penetrating the cylinder (where the cylinder wall is assumed to have a thickness of the fibre radius) a result is obtained which is comparable to the filter

packing density.

Given that r_f is significantly smaller than r_c, the value of $2(r_c^2 - r_f^2)^{\frac{1}{2}}$ may be approximated by $2r_c$ and the value of $\theta_r r_c$ may be approximated by $2r_f$, which allows Equation 4.13 to be reduced to,

$$C = 2(\pi + 1)r_c \tag{4.14}$$

Substituting Equation 4.14 into Equation 4.6 a new expression can be developed for the pressure drop, such that;

$$\Delta P_1 = -\rho g x_\infty + \frac{2}{r_c}\frac{(\pi + 1)}{\pi}\sigma cos\theta, \tag{4.15}$$

where ΔP_1 is the pressure drop with the new (adjusted) wetted perimeter.

Similarly Equation 4.6 can also be re-written as a function of the fibre radius (i.e. $f(r_f)$), such that;

$$\Delta P_2 = -\rho g x_\infty + \frac{2}{f(r_f)}\sigma cos\theta. \tag{4.16}$$

Equations 4.15 and 4.16 each illustrate the extent to which the changes in the variables will influence the pressure drop experienced by the model 'capillary' in comparison to an actual capillary.

The pressure drops associated with the change in wetted perimeter and the change in the capillary radius may be related to one another by a dimensionless term, ξ, such that:

$$\Delta P_1 = \Delta P_2 \xi, \tag{4.17}$$

giving;

$$\xi = \frac{\Delta P_1}{\Delta P_2} = \frac{(\pi + 1)}{\pi} \frac{f(r_f)}{r_c} \tag{4.18}$$

This accounts for both the deviation in the wetted perimeter and the variation in the capillary radius between a capillary and the 'theoretical' capillary. Therefore there is no reason that (given the appropriate function of r_f) Equation 4.18 should not also be able to be used as our equivalency factor. Thus relating the model 'capillary' to the whole filter; which, as previously demonstrated, generally acts as a capillary system.

By examining Equation 4.4, it can be seen that when no pressure differential exists, the model will reduce to the modified Washburn equation, from which it is derived, and therefore give the static capillary rise height when both ends of the capillary are at atmospheric pressure. The relationship between the capillary rise height and pressure drop is linear, with the slope affected only by the liquid density, fibre radius and packing density and the intercept (static capillary rise height) is a function of liquid density, surface tension, contact angle, fibre diameter and packing density.

As the pressure drop of a filter is proportional to its thickness, the filter thickness is considered to be an intrinsic property of the pressure drop. Therefore a term for thickness is not utilised in the determination of ω. Equation 4.4 may therefore be applied to filters of varying thicknesses and number of layers as used in this work, as well as experimental data from other authors.

4.3 Experimental

4.3.1 Materials

Oleophillic glass fibre filter media, produced by Hollingsworth and Vose (H&V, East Walpole, USA), and stainless steel (SS 316) media, produced by Bekaert (Zwevegem, Belgium) were used in the experiments, as they are

Table 4.1: Filter and oil properties examined

Filter		Filter Properties			Liquid Properties		
Filter	Material	α	r_f (μm)	z (mm)	Liquid	ρ (kg/m^3)	σ(N/m)
GF1	Glass	0.064	0.55	0.53	Oil D	841	0.028
GF1	Glass	0.064	0.55	0.53	Oil B	875	0.0295
GF2	Glass	0.066	0.32	0.65	Oil D	841	0.028
GF2	Glass	0.066	0.32	0.65	Oil B	875	0.0295
GF3	Glass	0.056	0.31	0.55	Oil D	841	0.028
GF4	Glass	0.054	0.62	0.65	Oil D	841	0.028
GF4	Glass	0.054	0.62	0.65	Oil B	875	0.0295
*GF5	Glass	0.0744	0.59	0.39	Oil A	913.4	0.0304
SS1	Steel	0.017	2.2	5.16	Oil B	875	0.0295
SS2	Steel	0.022	2.0	5.08	Oil B	875	0.0295
SS3	Steel	0.016	3.2	6.90	Oil B	875	0.0295

* GF5 data from Frising et al. (2005). This was a 110 mm diameter, circular filter loaded with di-ethyl-hexyl-sebacate (DEHS) (Oil A).

representative of commonly used industrial mist filter media. The properties of the filter media used in the experiments are shown in Table 4.1. The filters were either used as single layers, or sandwiched together to form 2 or 3 layered filters. The filters were tested using both a common laboratory oil, Sigma Light Mineral Oil (Sigma-Aldrich, Australia) (Oil D) and an industrial oil, RX Super (Castrol, Australia) (Oil B). The properties of which are given in Table 4.1.

The filters used in experiments were either 47 mm circular filters (GF1-GF4), or cylindrical elements (SS1-SS3) with a height of 90 mm and an inside diameter of 50 mm (using a coarse supporting mesh on the inside of the cylinder). All filters were oriented vertically, with the air flowing horizontally through the media. In the case of the cylindrical elements the flow was from the inside of the cylinder to the outside.

4.3.2 Experimental Apparatus

The experimental apparatus used for all measurements, is shown in Figure 4.2. In a typical filter system, the filter media would be saturated gradually

by collecting liquid aerosol particles, and may take days or weeks to attain steady-state saturation.

It was found that more rapid saturation of the media could be attained via pre-saturating the media to a higher level than the equilibrium saturation. Rather than slowly accumulating liquid during the experiment, the filter would initially be used in a supersaturated condition, and then slowly drain (or re-entrain) liquid until steady state had been reached. This allowed more rapid experiments and more consistent saturation values between repetitions. However, experiments using aerosol saturation were also performed; which included a detailed validation of the dipping method.

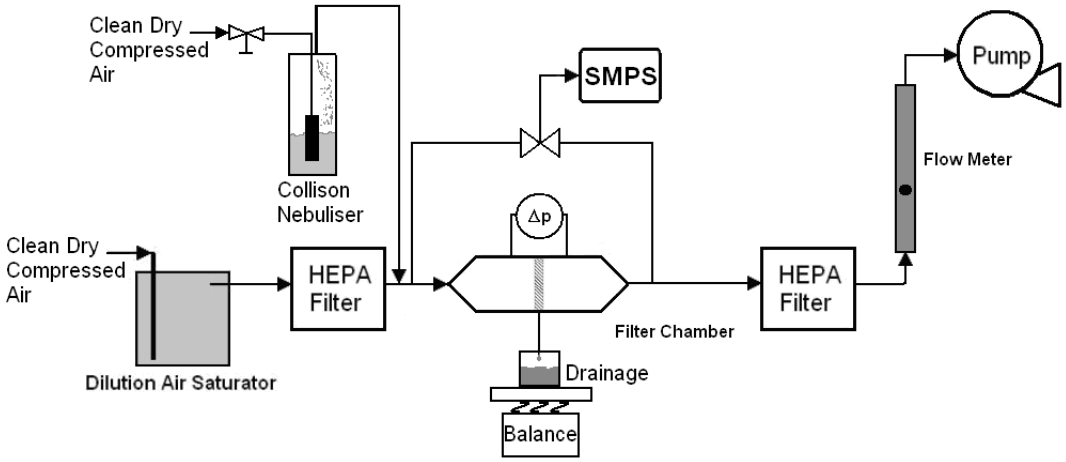

Figure 4.2: Experimental apparatus. Two different filter chambers were used to allow both cylindrical elements and circular filter discs to be examined.

To negate the possibility of evaporation of oil during experiments, the influent air was saturated (with the same oil as the test aerosol or filter saturation liquid) before entering the test filter chamber. The air saturator

consisted of a chamber packed with coarse, low packing density filter media, saturated with oil, through which air was passed.

High Efficiency Particulate Air (HEPA) filters were placed in front of the filter chamber and the flow meter. The former captured any particles that may have been generated by the saturator, while the latter captured the oil mist re-entrained from the test filter; before it could enter the flow meter.

A manometer (AHJ Systems, Sydney) allowed on-line measurement of the pressure drop across the filter. Particle concentrations before and after the filter were measured using a Scanning Mobility Particle Sizer (SMPS) system consisting of a TSI 3775 Condensation Particle Counter (CPC) and a TSI 3081 Differential Mobility Analyser (DMA). As the majority of experiments were performed using pre-saturated filters, the SMPS was principally used to ensure that the filter was only being challenged with clean (oil vapour saturated) air during these tests.

Three different filter face velocities were used in the experiments (see Section 4.3.3), which were set via a critical orifice.

4.3.3 Experimental Procedure

The filters were either allowed to saturate via collecting aerosol particles over several days (until steady-state pressure drop was reached), or via immersion in a bath of oil. In the "dipped" filter case, the filters were completely immersed in oil for thirty minutes, then removed and allowed to drain for a further thirty minutes, to allow an equilibrium saturation value to be obtained for the no airflow case, which is similar to the maximum value that could be expected in an industrial filter (with no airflow). This saturation level is greater than any equilibrium level which could be attained with air flowing through the filter.

The filter samples (in both clean and saturated conditions) and the filter

chamber were weighed before the commencement of each experiment, then again at the end. This allowed the amount of oil in the filter at equilibrium saturation to be determined, as the mass and density of the oil are known and so Equation 2.1 can be used.

Three filter face velocities (0.153, 0.219 and 0.285 m/s) were used in the experiments, using 1, 2 and 3 layers of filter media. A minimum of 3 replicate experiments were performed for each media/oil/layer combination. Overall the experiments utilised over 100 filter elements or filter media.

A number of tests were performed using the same (identical) piece of filter media, with re-saturation between tests, to ensure that the capillarity/pressure drop relationship was reproducible.

4.4 Results and Discussion

As mentioned previously, the majority of experiments were conducted with pre-saturated aerosol and no influent aerosol loading. This was to allow rapid and easily repeatable experiments, and to exclude loading induced effects (it has been observed that S_e and ΔP can increase with increasing aerosol loading in a real filter).

From Figure 4.3, it can be seen that the dipped and the aerosol saturated filters attained the same ultimate pressure drop, and hence equilibrium saturation, though at different time scales.

Upon commencement of airflow through pre-saturated media samples, ΔP decreased exponentially (and so presumably did S, as it is proportional to ΔP) as the oil drained or re-entrained from the (pre-saturated) filter. It was found that approximately 1 hour was required to reach S_e (defined as $< 1\%$ variation in S and ΔP over 1 hour) for the glass fibre media, and 20 hours for the stainless steel media (due to a significantly larger surface area). These are the times required to reach equilibrium saturation (S_e) with

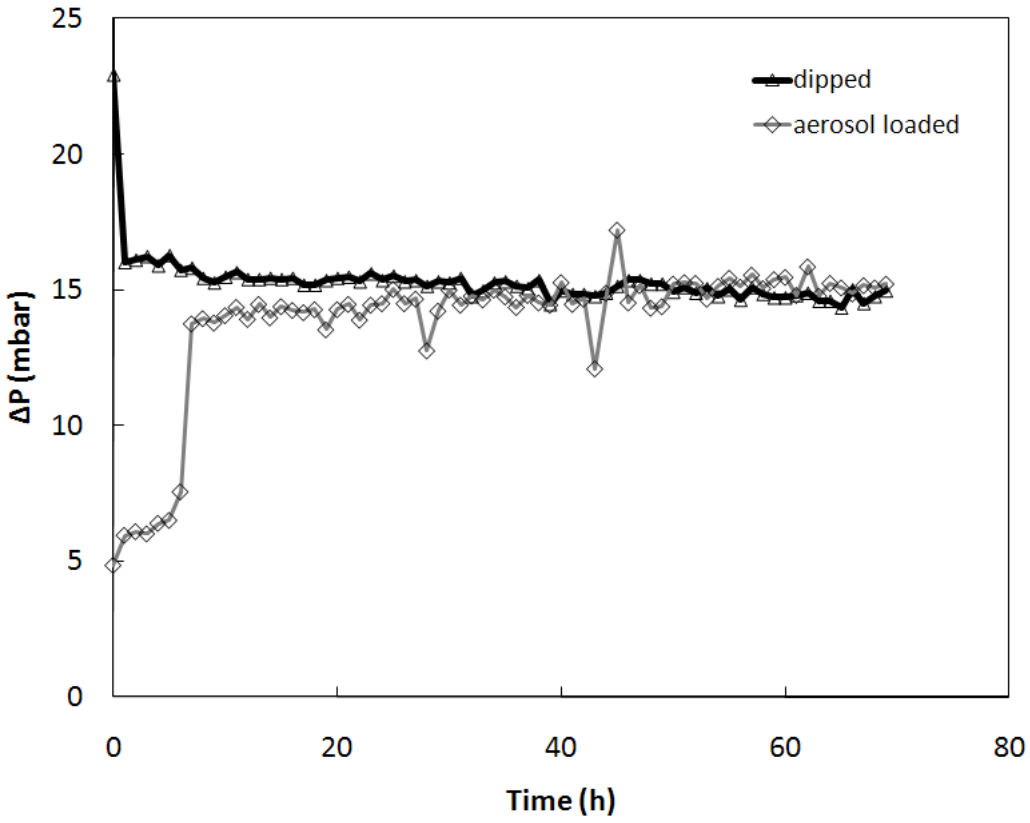

Figure 4.3: Pressure drop evolution for pre-saturated (dipped) and aerosol saturated SS3 filters

a pre-saturated filter, and would vary depending on the concentration of the aerosol. If the experiments were to be started with a clean filter, loaded conventionally, over 100 hours filtration time would be required. The glass fibre experiments were usually conducted for a minimum of 2 hours duration. Some experiments were, however, continued to 12 hours to ensure that the apparent steady state reached at 2 hours was indeed the true steady state. The experiments using stainless steel media were generally 40 hours in duration; with some extended to 200 hours.

4.4.1 Examination of Different Filter Media

The experiments were conducted using 4 different glass-fibre (GF) media and 3 different stainless steel (SS) media (the properties of which, are given in Table 4.1). Figure 4.4 shows the equilibrium saturation (S_e) for each of the GF filters, measured in this work, at different filtration velocities and Figure 4.5 shows the corresponding filter pressure drop.

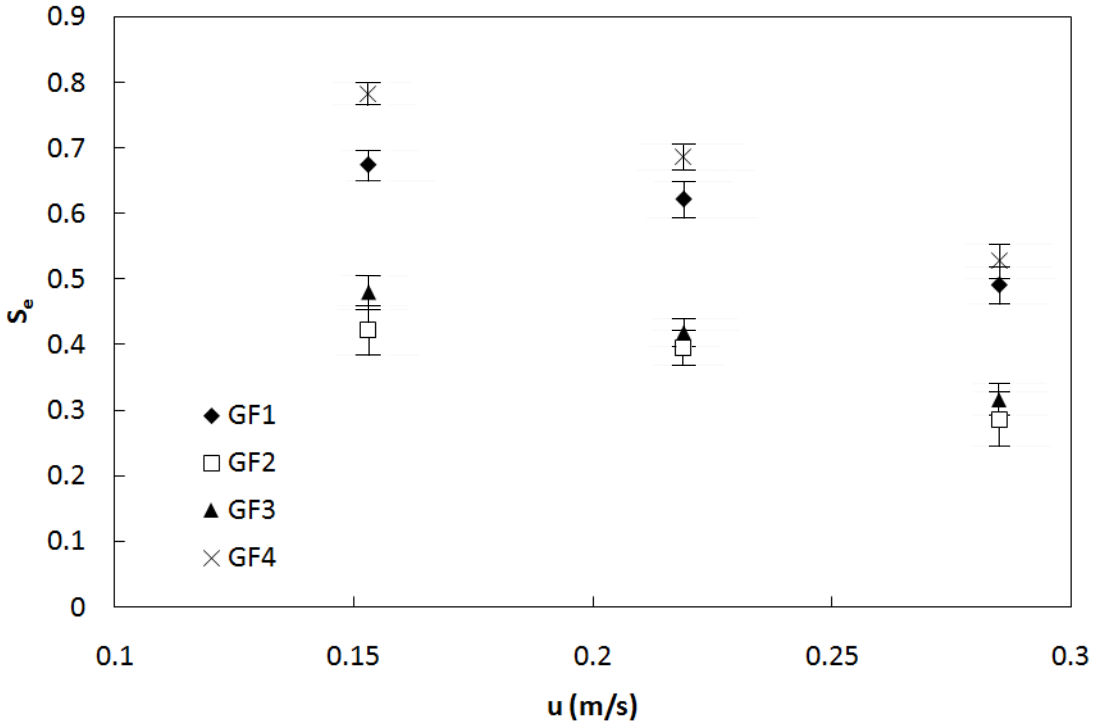

Figure 4.4: Equilibrium saturation for GF filters at different velocities

Figure 4.4 shows that the GF1 and GF4 are similar and the GF2 and GF3 media are similar in terms of S_e, with the largest difference being between these two pairs. This may be explained by examination of the filter properties (see Table 4.1) where, GF2 and GF3 have similar packing density to fibre radius (α/r_f) ratios and GF1 and GF4 posses α/r_f ratios that are closer to each other than they are to those of either GF2 or GF3.

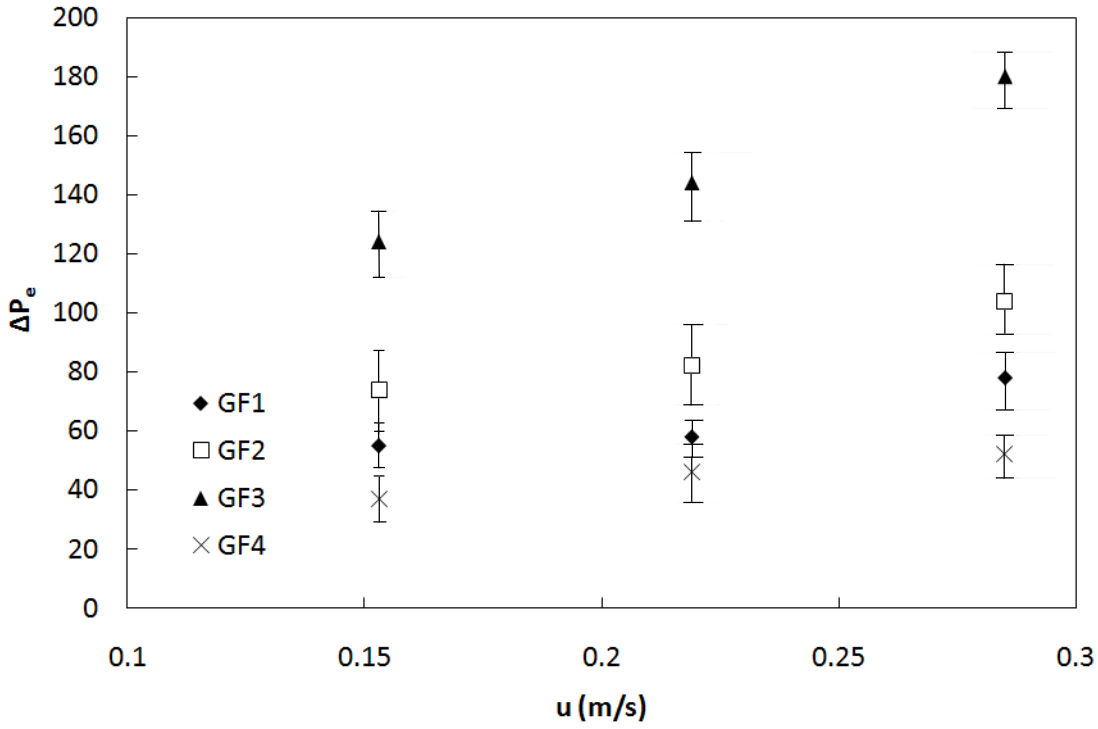

Figure 4.5: Filter pressure drop for GF filters at different velocities once the equilibrium saturation had been reached

Examination of Figure 4.5 indicates that the pressure drops for the GF1, GF2 and GF4 filters are closer to each other than any of them are to the GF3 filter. For the GF1, GF2 and GF4 filters the trend may be explained in terms of the α/r_f ratio, where the pressure drop is higher for filters with higher values of α/r_f. The GF3 filter however, seems to be an exception to this trend. The GF3 filter is however different from the other filters in that it is the only one of the four filters which has both a relatively low packing density and a relatively low fibre radius.

Each of the data points in Figures 4.6 and 4.7 represents a minimum of three measurements. The SS1 and SS3 filters can be seen in both Figures 4.6 and 4.7 to follow similar patterns, with the difference between the two likely due

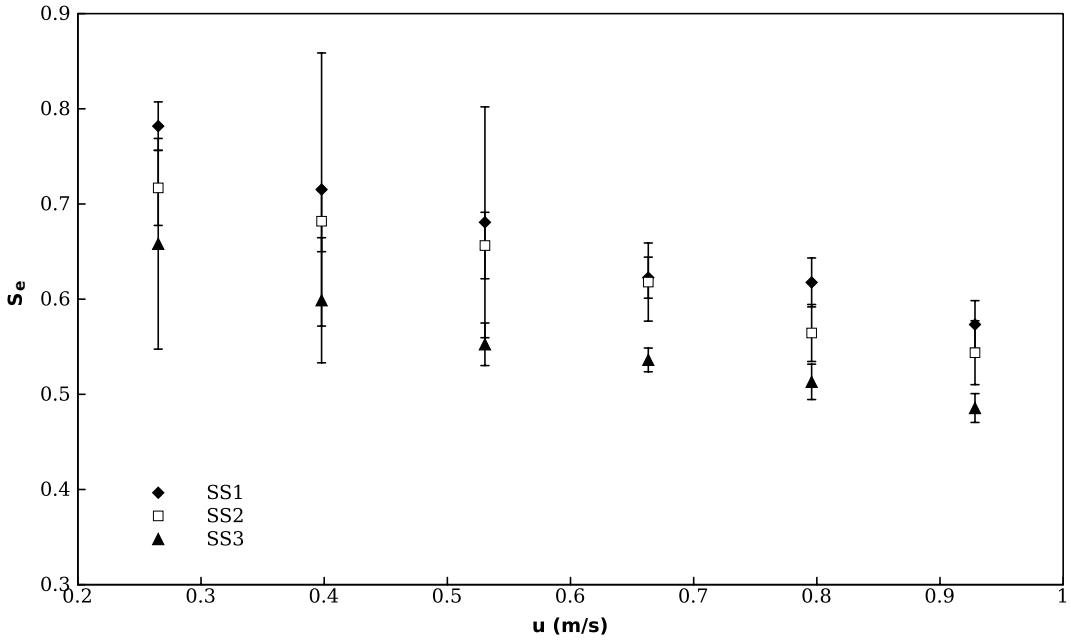

Figure 4.6: Equilibrium saturation for SS filters at different velocities

to the α/r_f ratio. The SS2 filter behaves slightly differently, though it also has a α/r_f ratio that is significantly higher than that of the SS1 and SS3 filters.

4.4.2 Examination of Different Layers of Filter Media

Using the GF1 filters and Oil D, the influence of the number of filter layers was investigated. Measurements were carried out on both single and two-layer media, and were attempted on 3-layer media also.

Figure 4.8 shows the equilibrium saturation reached for each combination of airflow and number of filter layers (for the GF1 filter), while Figure 4.9 shows the pressure drop for the same experiments (all values are mean ± SD). It was observed, that although the dual-layer filter elements possess a lower S_e than the single layer, the ΔP value is higher for the dual layer; thereby reinforcing the behaviour as a capillary system, where the pressure drop acts

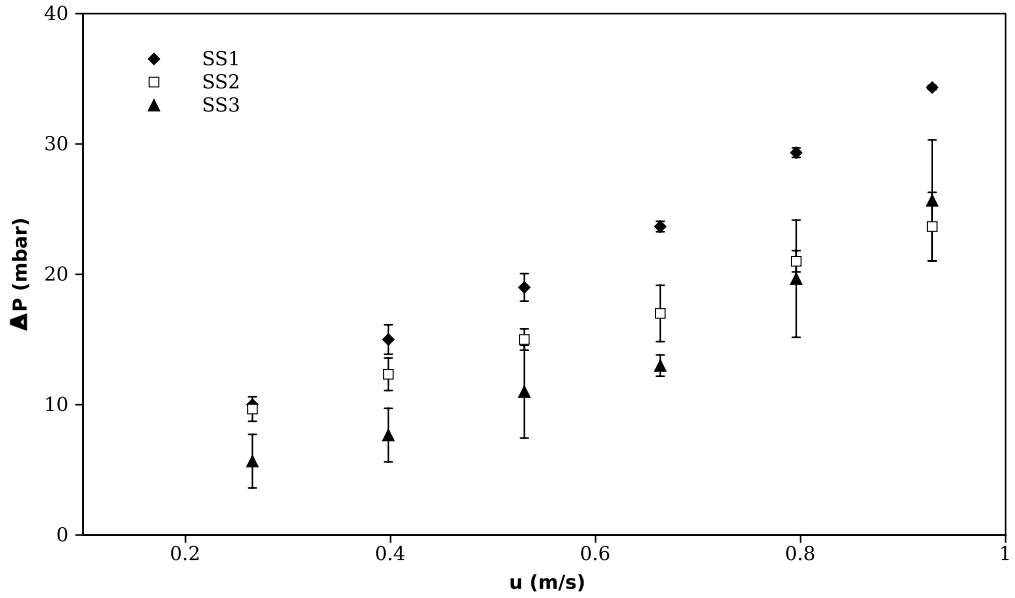

Figure 4.7: Filter pressure drop for SS filters at different velocities once the equilibrium saturation had been reached

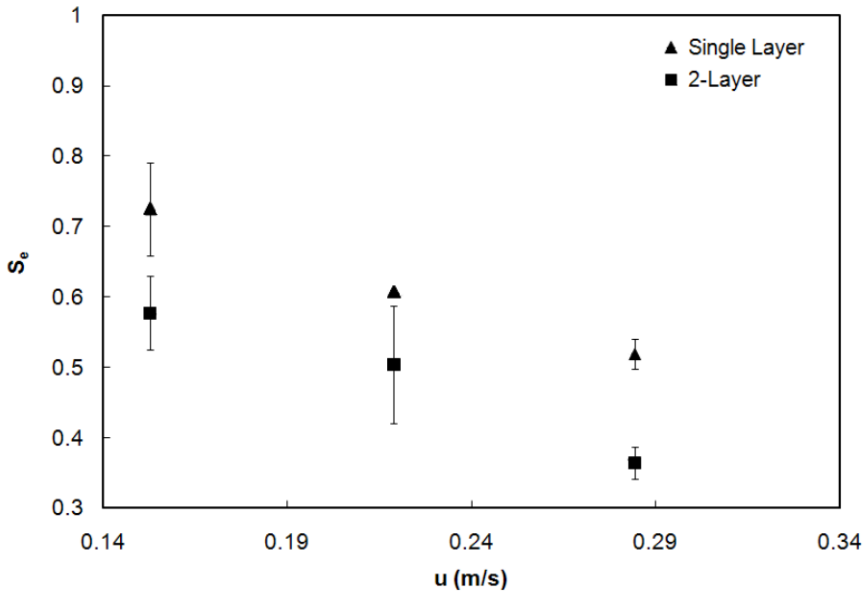

Figure 4.8: Equilibrium saturation of filter media as a function of filter face velocity

to decrease saturation.

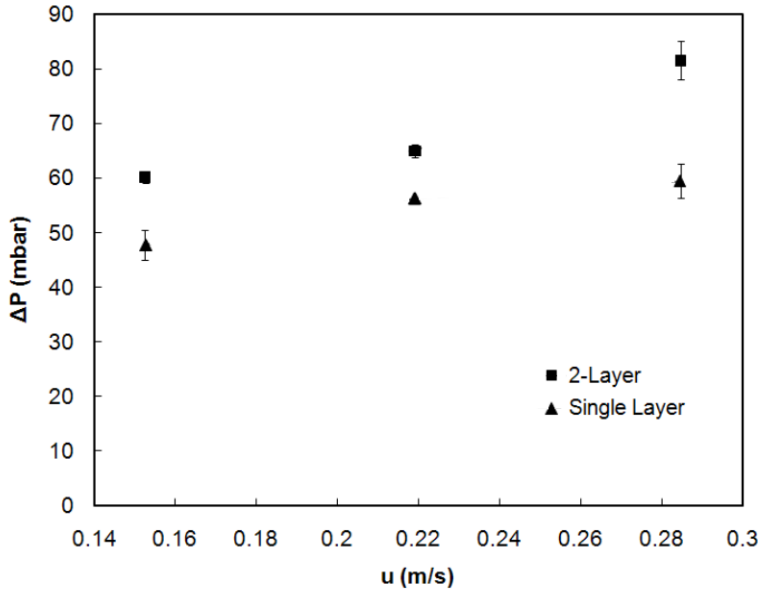

Figure 4.9: Pressure drop across the filter corresponding to the equilibrium saturation

For the specific media used in the above experiments, it was possible to derive a simple empirical equation to determine S_e, of the form,

$$S_e = -1.6u - 0.14(N_l - 1) + 0.96, \tag{4.19}$$

where N_l is the number of layers of filter media in the element. The R^2 value for the fit to the one layer data is 0.994, for two layers 0.964 and 0.810 for the few samples of 3-layer data (not shown). Likewise for the equilibrium pressure drop (the pressure drop that corresponds to the equilibrium saturation, ΔP_e), the following relationship could be determined,

$$\Delta P_e = -87N_l u + 35. \tag{4.20}$$

The R^2 value for one layer is 0.943, for two layers 0.910 and for the few three layer experiments conducted (not shown), a relatively poor fit of 0.650 was found. However it was possible that the filter chamber did not seal perfectly when 3 layers of media were used, which may have influenced the results.

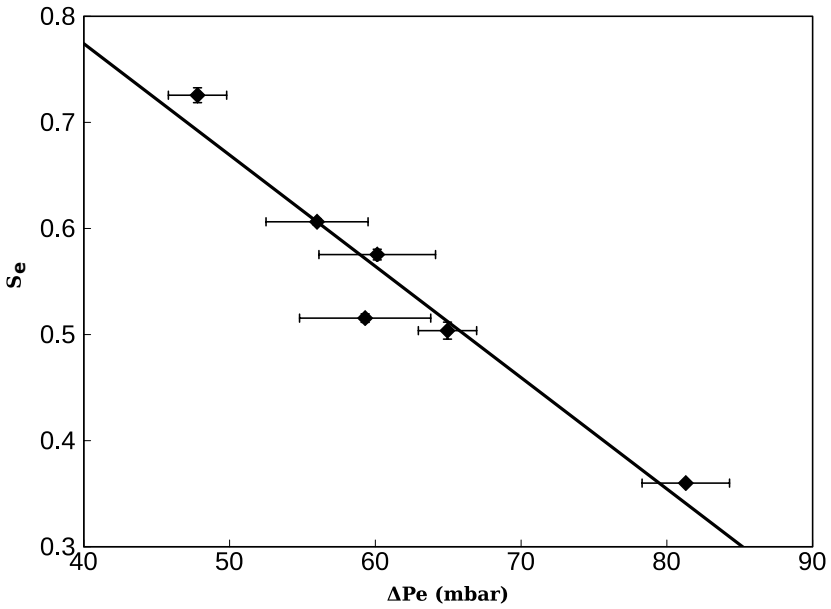

Figure 4.10: S_e and ΔP for GF1 filters, using oil A with linear fit added

When the final pressure from each experiment is plotted against the final saturation of the respective filter (as shown in Figure 4.10) a linear correlation can be seen ($R^2 = 0.934$ for the linear fit). In this figure, the results for both one, and two layers of filter media, for all three flow rates, have been included (the three points on the left hand side of the graph are for the 2-layer media, the three points on the right hand side are for the single layer media). Equation 4.21 displays the linear fit to Figure 4.10, which is fitted to the whole dataset, thus giving a relationship that is independent of the number of layers of media.

$$S_e = -0.0105\Delta P + 1.1939. \tag{4.21}$$

4.5 Saturation Model

Initial model calibration determined that if the pressure drop across the (entire) filter (ΔP) was utilised, then the model would predict x_∞ (and hence S_e) <0. The coefficient ω was the result of a comparison between a theoretical capillary and a simplified model of filter media.

In order to use Equation 4.4 it is necessary to select/designate a function of r_f to be used in Equation 4.18. During the development of Equation 4.18, a number of scenarios were considered, one of which led to an elliptic integral (Equation 4.12). While it was the simple case that was chosen, the integral is useful in that it is linear in terms of r_f, which suggests that the function of r_f used in Equation 4.18 will be linear. It would seem that the simplest function that could be used here would be $f(r_f) = r_f$, which would give an equivalency factor of;

$$\omega = \frac{(\pi + 1)}{\pi} \frac{r_f}{r_c}. \tag{4.22}$$

The equivalency factor is now expressed as ω as we will be relating the measured pressure drop to an 'equivalent' pressure drop and no longer the pressure drop of a true capillary to our theoretical one. As such the equivalent pressure drop, ΔP_E, can be found using Equation 4.5. The values of ΔP_E were then used in Equation 4.4 to find x_∞.

The predicted values of x_∞ were converted to equilibrium saturation (S_e) by simple geometric calculation. (i.e. the volume of the filter accounted for by x_∞ multiplied by the void space $(1 - \alpha)$ of the filter). This method assumes that a sharp boundary exists between the saturated and non-saturated parts of the filter, which may not be the case in some filters (Jaganathan et al., 2009). While in the cases presented this sharp boundary was not ideal, in the case of the glass fibre media, the saturated and non-saturated portions could be differentiated visually, and were sufficiently sharp to be approximated as such in this case.

There is however a deviation between the measured and predicted S_e values, which cannot be explained by altering the value of $f(r_f)$ in Equation 4.18. This is not unexpected though, as it should be remembered that the filter is being modelled as if a system of capillaries. It would therefore seem likely that the capillary radius used in Equation 4.4 would be subject to some variation (error), and in fact due to the (very) porous nature of the media there is the possibility that a range of effective capillary radii for a particular filter may exist, which can possibly be accounted for by some form of correction to r_c. The capillary radius then becomes;

$$r_c = \left(-A log_e \left(\frac{\alpha}{r_f} \right) - B \right) c_f. \tag{4.23}$$

As mentioned in Section 4.2 the values of A and B are media-specific constants. These values are also the result of fitting a least squares regression to experimental data with correlation coefficients varying between 0.53 and 0.88 depending on material type (Mullins et al., 2007a).

The contact angle (θ) term in Equation 4.4 does pose a problem however, as it is a dynamic contact angle, and is unable to be determined experimentally for fibrous filters. However, previous work by Mullins et al. (2007a) determined a range of values for dynamic contact angles, obtained from studies of capillarity in similar or identical fibrous media. They found that the dynamic contact angle fell within the range of 60.7 to 89.3 degrees for all media studied. Similarly Marmur and Cohen (1997) found that dynamic contact angles were typically within the range of 71.9 to 76.6 degrees. So, setting an initial contact angle within these ranges is not unreasonable. Given that only the intercept of the capillary model will be affected by the contact angle and not the slope, it is possible to use the range of contact angles and the correction factor term for r_c to fit the model.

It can be seen in Figure 4.11 that a good fit between the model and exper-

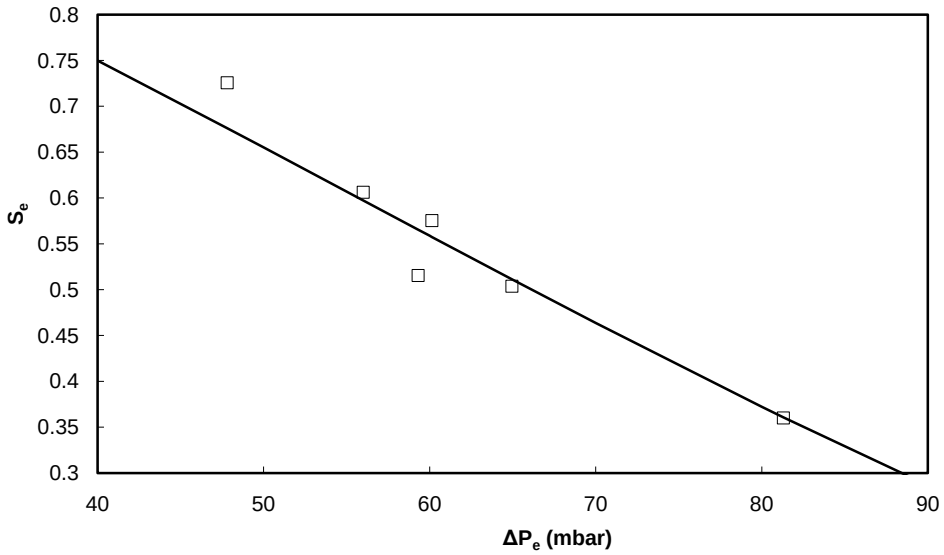

Figure 4.11: Experimental (symbols) and predicted (solid line) filter saturation S_e as a function of ΔP_e, filter GF1, oil A

imental results could be obtained, demonstrated by an R^2 value of 0.938. Which also serves to validate our choice of function of r_f when determining the equivalency factor.

It should be noted, that it is possible to obtain a value of x_∞ greater than the filter height using the capillary model. This represents a completely saturated filter and the value of x_∞ cannot be converted to a saturation using a function of filter geometry. This is however allowable as it is entirely possible that for certain fibre radius-packing density combinations that the (theoretical) capillary rise height will exceed the filter height that is imposed by the filter chamber.

To demonstrate the validity of the model, it was applied (in the same man-

Table 4.2: Filter and model parameter

Filter		Oil	Model		
Filter	Material	Oil	r_c (μm)	c_f	θ
GF1	Glass	Oil D	66.96	0.415	78.2
GF1	Glass	Oil B	66.96	0.415	77.5
GF2	Glass	Oil D	37.94	1	79
GF2	Glass	Oil B	37.94	1	78
GF3	Glass	Oil D	44.66	0.89	75.6
GF4	Glass	Oil D	81.33	0.32	79.1
GF4	Glass	Oil B	81.33	0.32	78.8
GF5	Glass	Oil A	62.88	0.29	71.2
SS1	Steel	Oil B	31.18	0.91	68.8
SS2	Steel	Oil B	22.81	0.98	74.9
SS3	Steel	Oil B	40.16	0.85	68.8

ner) to data corresponding to a range of (43 tested filters, each with an average of $\geq$ 3 filter tests) glass fibre (GF) media and stainless steel fibre (SS) media tested by the author for two different oils and also fitted to results obtained by Frising et al. (2005). All filter parameters are shown in Table 4.1. The fitted parameters corresponding to these filters are shown in Table 2.

Figure 4.12 shows the measured vs predicted data for the combined dataset of GF1-5 and SS1-3 for all different face velocities.

As can be seen in Figure 4.12 there exists a good fit between modelled and predicted values for the whole dataset ($R^2 = 0.904$). The fit to the glass fibre media alone is further improved at $R^2 = 0.946$. The slight deviation observed in the stainless steel media is likely due to the substantially different packing density-to-fibre radius ratio, which indicates that this media may behave less like a capillary system than the glass fibre media. Nevertheless, all data points in Figure 4.12 can be seen to fall within $\pm$ 10% of the ideal value. Also, as the conversion to saturation does not take into account the changes in the saturation profile through the thickness of the media, this deviation may be evidence of the effect of neglecting the 'u' shaped saturation profile which is sometimes present in thicker filter media. This effect may need

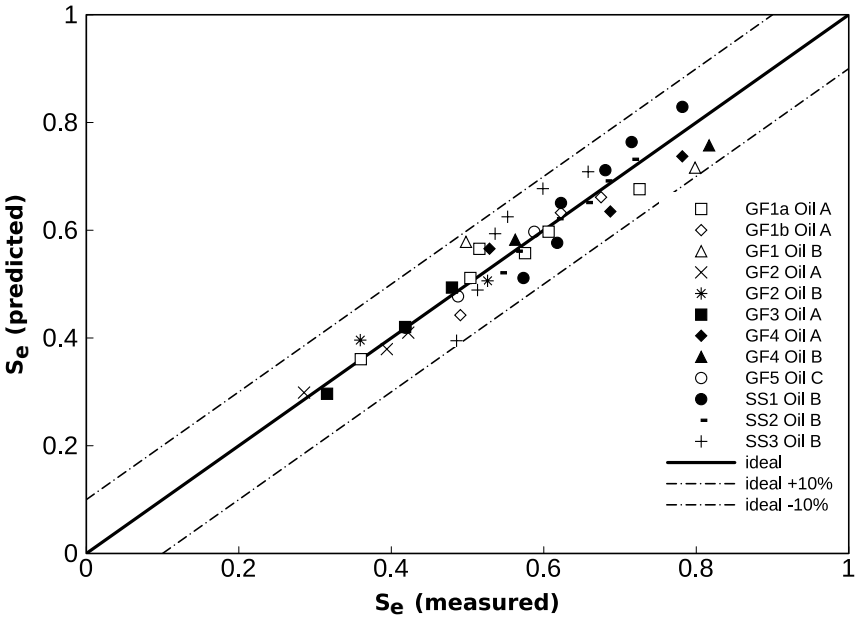

Figure 4.12: Predicted versus measured equilibrium saturation for all filters

to be accounted for when the thickness of the filter/filter layers exceeds 5mm.

Given the good fit it may be concluded that Figures 4.11 and 4.12 demonstrate the validity of the model. It also indicates that, as expected, the correction factor is dependent on the filter being used and therefore is a function of one or several properties. If this function can be determined then it should be possible to determine the saturation of a filter for a given pressure drop from easily measurable properties of the filter.

Figure 4.13 shows the capillary rise height obtained by the modified Washburn equation for varying values of capillary radius and contact angle. It can be observed that increasing θ or decreasing r_c will both decrease x_∞, which should ultimately be the goal in mist filter design.

Using data in Tables 4.1 and 4.2, equations for θ and c_f could be determined using generalised linear regression with stepwise backwards elimination. The

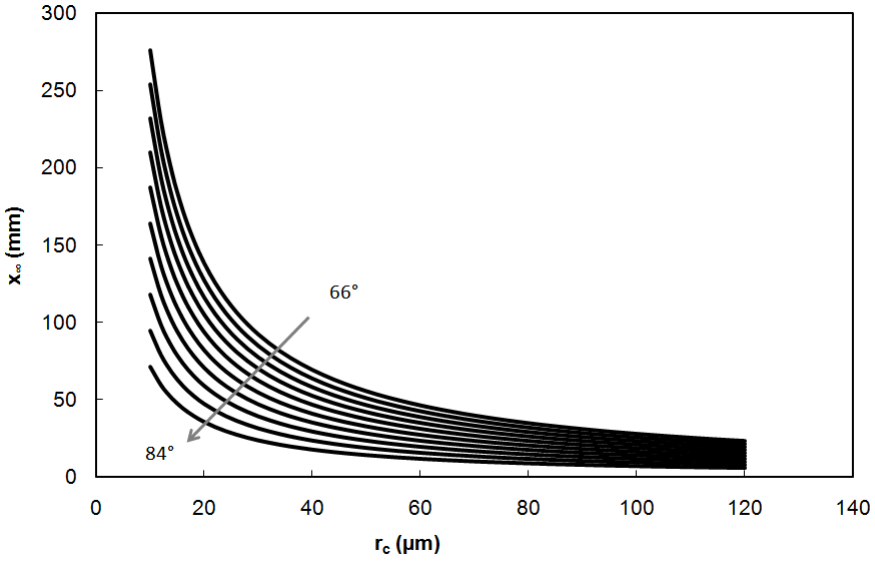

Figure 4.13: The influence of r_c and θ on x_∞

resultant equations were,

$$\theta = 151.5 - 3.5r_f + 8257\sigma - 0.36\rho \tag{4.24}$$

and,

$$c_f = 2.0 + 0.4Z - 8.7\alpha - 0.6r_f - 0.04\gamma \tag{4.25}$$

where γ is the surface energy of the fibre material, and the other parameters are as previously defined. The R^2 values corresponding to the above equations are 0.83 for Equation 4.24 and 0.87 for Equation 4.25. It can be observed that θ can be defined in terms of fibre size and fluid properties, which is intuitive, and c_f is a function of filter geometry and fibre surface energy.

Alternatively if the correction factors for the glass fibre filters are plotted against their respective fibre radii there is strong evidence of a linear correla-

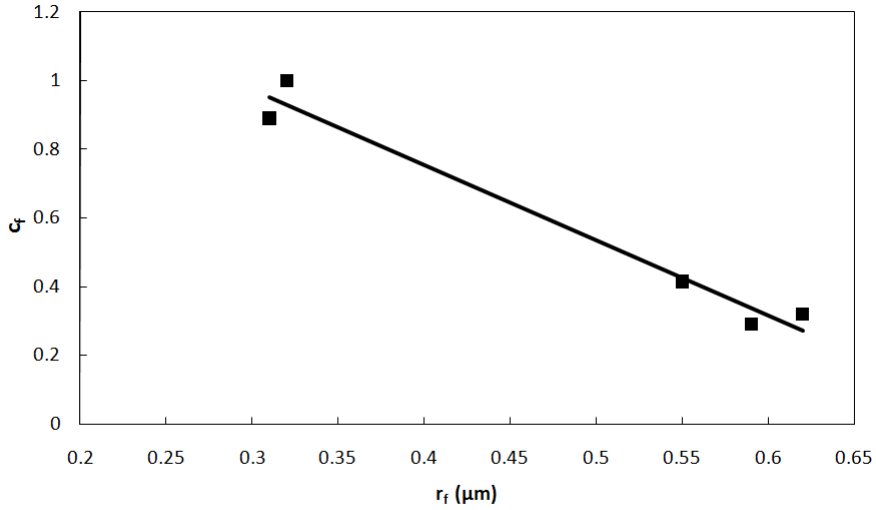

Figure 4.14: The relationship between the correction factors obtained for the glass fibre media and the fibre radii (with linear fit)

tion between the two (see Figure 4.14). It is known from our results that the correction factor is independent of the oil type used and so it may ultimately be easier to express the correction factor as a function of r_f; as we know that the value of r_c is heavily dependent on r_f. Additionally if different correction factors are obtained for the different fibre types, it will not be necessary to use the surface energy term given by the linear regression. It may also lead to greater accuracy in the model if the fibre materials are treated separately.

Taking this approach, the value of c_f for the glass fibre media may be found using the following equation, where the value of R^2 is 0.9702,

$$c_f = -2.1928 r_f + 1.6312. \tag{4.26}$$

4.6 Conclusion

This work has shown that it is possible to determine liquid saturation in single and multi-layer fibrous filter media using an empirically fitted capillary-based

model. The work has also detailed several important relationships with respect to saturation and pressure drop in single and multi-layered filter media. However, further work is required in order to allow the accurate prediction of the correction factor, which appears to be a function of the fibre diameter.

The model, as it is, will require some experiments to be conducted to allow the model to be calibrated to a new media type. The capillary model detailed within this chapter is applicable to the glass-fibre and stainless steel media used in this work and should also be applicable to similar filters (i.e. those which display significant capillarity and sharp boundaries between wetted and non-wetted areas). In this regard it is potentially of greater efficacy than the Raynor and Leith (2000) model in determining the equilibrium saturation of mist filters.

It is hoped that this work will assist in the advancement of mist filter theory, and the optimisation of such filter systems.

Despite the apparent applicability of large scale capillary models of filters, a more detailed finer-scale study of wetting and capillarity appears merited. Therefore it may be more appropriate to consider fibrous filters on the basis of a single fibre, much like the single fibre efficiency theory. Such a single fibre approach is taken in the following Chapters (5-8), to examine the behaviour of coalesced droplets on fibres.

5 Development of a Method to Allow the Measurement of the Force Required to Move a Coalesced Liquid Droplet

5.1 Introduction

Fibrous filters are a complex, usually random, arrangement of fibres and as such it is difficult to accurately describe their behaviour macroscopically. In the case of efficiency this issue to some extent has been resolved by basing models on the capture efficiency of a single fibre. Which, as has been documented in Section 2.5.3 and the literature, is sufficiently effective for determining the capture efficiency of clean filters with known properties. So the understanding of filter behaviour on a simple (fundamental) basis can provide viable models for the behaviour of complex arrays of these fibres. It is this approach which has been used to examine the droplet and coalescence processes that take place in mist filters. By examining the coalescence and transport of collected oil droplets on a single fibre one can likely describe the coalescence and transport behaviour of a filter made up of these fibres.

As has been extensively detailed in Section 2.7, the Atomic Force Microscope (AFM) may be used to measure force interactions between surfaces. Utilising Lateral Force microscopy, where the lateral (torsional) movement of the cantilever is measured (as opposed to the normal movement), it is possible to measure the deflection of a cantilever that is engaged with an oil droplet. The cantilever is used to move the droplet along a length of the fibre, and the deflection of the cantilever is measured and can be converted to a force if the torsional spring constant of the cantilever and the lateral sensitivity of the scanner are known.

There are however a number of factors that need to be considered when conducting these measurements. First and foremost it is a liquid droplet that the cantilever is engaging, so there exists the very real possibility of

droplet deformation occurring. To address this, a special methodology had to be developed to allow useful and reliable measurements to be made. This is detailed in Section 5.2.

5.2 Methodology

The versatility of the atomic force microscope (AFM) has been thoroughly detailed in Section 2.7. In this work, the AFM has been used to measure the force required to move a coalesced droplet along a filter fibre. In order to perform such measurements a procedure was required which allowed an oil droplet to be successfully engaged by and moved along a fibre by a cantilever. This procedure pertains to the preparation and loading of the filter fibres, the preparation of the AFM cantilevers and the measurement parameters of the AFM itself.

5.2.1 Fibre Preparation

Filter fibres (whether they be polymer, glass-fibre, or stainless steel) are generally oleophillic in nature and as such when examining axisymmetric droplets, little surface preparation is required. Essentially the fibres must be mounted, cleaned and then loaded with aerosol. Oleophobic fibres need to be prepared, which is done by applying a low energy polymer coating to the fibre surface, which is effectively how these types of fibres are commonly prepared in industry.

All fibres were mounted in custom made stainless steel (SS 304) mounts, which allowed a length of fibre to pulled taught and held firmly in place. The fibres were cleaned in their mounts, by ultrasonic cleaning in an ethanol bath. The ethanol was then removed by placing the fibres (and mounts) in milli-Q water, in a second usage of the ultrasonic bath. The fibres were then dried under nitrogen. The fibres were then loaded, by exposing them to an aerosol of the particular oil being measured which was generated using a Collision Nebuliser.

To create oleophobic fibres, the initial cleaning procedure was followed, as described above. The fibres were then coated with a fluorinated co-polymer (TL1143, Thor Chemie, Speyer, Germany) prepared at a 1:10 dilution with water. The coated fibres and the mounts were then placed in an oven at 100°C for 4 hours to allow the polymer to cure. They were then ready to be loaded, using the same method as for the oleophillic fibres.

5.2.2 Cantilever Preparation

In order to measure the force required to move a liquid droplet along a fibre, there must be a way of engaging the cantilever on the droplet, without deforming it or removing it from the fibre. Starting initially with commercially available cantilevers (tipped) and using them without modification, it was found that the oil droplet would wet the cantilever tip and arms and thereby be removed partially or completely from the fibre. The cantilever tip was then rendered oleophobic by applying a surface coating, in order to prevent the oil from spreading over the cantilever.

The cantilevers were coated by lowering the tips into a solution of one part fluorinated co-polymer (TL 1143, Thor Chemie, Speyer, Germany) to ten parts de-ionised water. The coated cantilevers were then heated to 100°C for 3 hours, to allow the polymer to cure. The coating was found to be very effective, with the cantilever tip being able to be lowered into the surface of the droplet without altering the droplet shape. However the coated cantilever was unable to move the droplet as the oleophobic coating was so effective that the tip simply moved through the droplet. Therefore a cantilever needed to be prepared such that it was sufficiently oleophobic so as to prevent the droplet preferentially adhering to the cantilever, whilst having a strong enough attachment to the droplet so that the droplet could be moved along the fibre.

Given the (very) small size of the cantilever tip (of the order of nanome-

tres), a sufficiently large contact between the cantilever and drop could not be obtained with the existing cantilevers. The optimal solution found, was to prepare colloidal probes. For this purpose different (NP-OW, tipless silicon nitride cantilevers, Veeco, Camarillo, USA) cantilevers were used. The probes were prepared by attaching glass micro-spheres to the ends of the cantilevers, using an epoxy-resin (Araldite, Selleys, Australia) and then once set, coating the micro-spheres with the polymer solution. A cantilever prepared in this manner is shown in Figure 5.1.

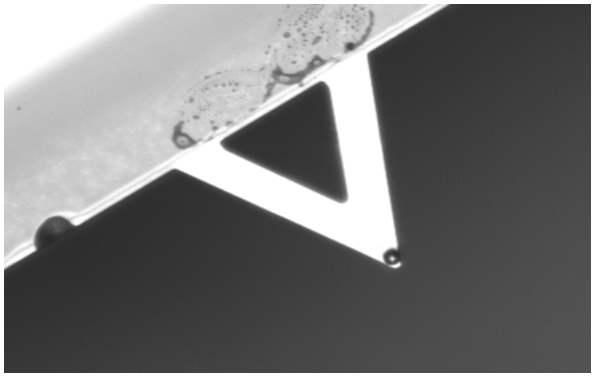

Figure 5.1: A cantilever (LTK) with a glass micro-sphere attached

Each cantilever chip contains four cantilevers, which vary in length and arm width, so there is a long thick (LTK) and a short thick (STK) cantilever and a long thin (LTN) and short thin (STN) cantilever. Initial experiments revealed that the TN cantilevers were not stiff enough to allow the droplet to be moved without exceeding the maximum measurable deflection on the microscope, therefore the TK cantilevers were used. Preference was given to the LTK cantilevers as, at least for the measurements in the oleophillic case, they could be used effectively (i.e. they could be successfully engaged with a droplet and upon moving the droplet were stiff enough that they did not reach a deflection outside their measurable range). If however the maximum deflection was reached using these cantilevers, then the STK cantilevers were used. The STK cantilevers were used only in the cases where the deflection of the LTK cantilevers was too great, as while the STK cantilevers were stiffer, this was coupled with reduced sensitivity.

5.2.3 Making a Measurement

In order to make a measurement the probe needs to be lowered into contact with the liquid droplet on the fibre. The size of the sphere on the probe needed to be chosen on the basis of the size of the droplet that was measured, with a larger droplet requiring a probe with a larger sphere and a smaller droplet able to be measured with a probe with a smaller sphere. The required sphere size was found not to relate to the fibre diameter, so even for the smallest fibre diameter, sometimes the probe with the largest sphere was necessary in order to make a measurement. The selection of an appropriately sized sphere was initially a trial and error process, but once enough measurements had been made this could be predicted.

It could be seen whether or not a sphere was an appropriate size by observing the motion of the probe and the droplet as well as through examination of the cantilever deflection plot. If a sphere is too small, the contact with the droplet will not be strong enough and the probe will move through the droplet without moving it; or will move within the droplet before the droplet begins to move. If a sphere is too large, it can visually deform the shape of the droplet, or the system will begin to measure the interaction between the probe and the fibre surface through the oil. This made it difficult to determine the deflection of the probe that corresponds to the droplet beginning to move. This is significant with respect to the measurement of droplets on oleophobic fibres and will be discussed in Chapter 8.

The probe also needed to be engaged centrally on the droplet, as this is the highest point on the droplet and so the closest to the probe. Also this is the furthest point from either contact line; which could become deformed if the probe was engaged at either of the droplet ends. For the purposes of this work, a probe with an appropriately sized sphere that is engaged centrally on a coalesced liquid droplet, which maintains its shape, was termed a good engagement.

As lateral force microscopy (LFM) that was used for these measurements, the scan angle was set to 90°. Additionally the slow scan axis was disabled as the measurement being made was of a droplets' movement along a fibre. Given that in some cases the stability of the droplet could be affected by sudden applications of force, an initial (pre-engagement) scan size was set to 1nm. After the probe was engaged this was gradually increased, until the desired scan size was reached as starting with an initial scan size that was too high could lead to the droplet becoming unstable and moving up on to the probe. This resulted in a deformed droplet shape (or complete droplet detachment from the fibre) and the droplet contacting the cantilever arms, rendering any deflection measurement useless as the oil effectively acted to 'dampen' the deflection.

The measurements were recorded for between 128 and 512 sample lines (which with the slow scan axis disabled, are essentially repeat measurements) and the average of these sample lines taken for each droplet measured.

After measurements have been made, or if the oil droplet is pulled off the fibre or up on to the cantilever arms, the cantilevers were cleaned by immersing them in n-Pentane (Sigma Aldrich, Australia). The cantilevers were then visually inspected, under a light microscope to ensure that no oil was visible and that the cantilever had not been damaged; before it was used for further measurements.

5.2.4 Force Calibration

There are a number of cantilever calibration techniques available (see Section 2.7.4). All have their potential drawbacks and limitations and as such, it is necessary to select the method which best suits the AFM set-up being used and the nature of what is being measured. Given that this work utilised the technique of lateral force microscopy, the torsional spring constant and the lateral signal sensitivity needed to be found so that the force calibration could be performed.

The method developed by Cannara et al. (2006) was selected as the best means of measuring the lateral signal sensitivity. This method was chosen as it allows the lateral signal sensitivity measured for a single 'test' cantilever to be converted to a lateral signal sensitivity for any other cantilever used, by means of a mathematical formula. This has the obvious advantage of avoiding the need to carry out an individual measurement on each of the cantilevers used. Additionally it meant that cantilevers already prepared and used in the development of the methodology could be cleaned and used for the force measurements. For this work both LTK and STK cantilevers were used as 'test' cantilevers.

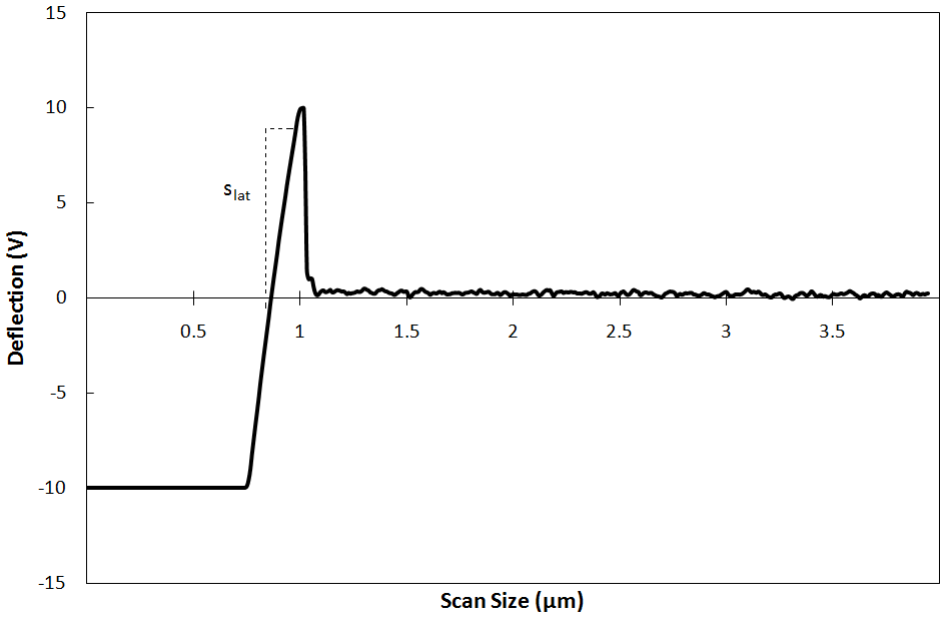

Figure 5.2: Lateral signal sensitivity measurement for a probe utilising an STK cantilever

A lateral signal sensitivity measurement is shown in Figure 5.2. As with the droplet measurements these are the subject of a series of scan lines. The lateral signal sensitivity (s_{lat}) is simply the slope of the line, as indicated in

Figure 5.2. This can then be converted to give the s_{lat} values for the other cantilevers used by applying Equation 2.78.

The force calibration factor, as defined in Equation 2.77, also requires the torsional stiffness of the cantilever to be known. This may be determined analytically, using Equation 2.76, or from a torsional spring constant, using Equation 2.74. The analytical expression at first seemed a good option, due mainly to its relative simplicity (it uses cantilever dimensions that may be measured optically and bulk material properties). It is however the use of the bulk material properties that effect the accuracy of this method, particularly when other methods do not require them.

The bulk material properties, namely the Young's modulus and the Poisson ratio, are in fact difficult to determine for silicon nitride cantilevers, as they differ from that of bulk silicon due to the nature of their preparation and the presence of a thin metal oxide surface coating. As such the range of values for the Young's modulus give in the literature is quite large (118-200 GPa)(Vila et al., 2003). Additionally Khan et al. (2004) studied the Youngs' modulus of silicon nitride used in AFM cantilevers and found that it was often much higher than quoted by the manufacturers. Given the difficulties associated with this it was determined, for reasons of scientific rigour, to select a calibration method that does not require the use of these bulk material properties.

Therefore a method that involves the determination of the torsional spring constant, which may be converted to a stiffness using Equation 2.74, proved to be a better alternative. Of the methods available to determine the torsional spring constant (discussed in Section 2.7.4) only the torsional Sader method (Green et al., 2004) is practical. This is because the other methods require additional equipment (Lateral electrical nanobalance and Diamagnetic levitation spring methods), calibration standards (the wedge method) or tedious procedures (Lever and Torsional added mass methods). The torsional Sader method allows the determination of the torsional spring constant

using the cantilever geometry (which can be determined optically) and the cantilever resonance frequency and quality factor (which can be measured using the AFM). It is this method that is used in this work.

Equations 2.73, 2.74 and 2.78 were evaluated for each cantilever used in the work and the calibration factor for each cantilever determined using Equation 2.77.

5.3 Measurements, Observations and Limitations

Once a good engagement could consistently be obtained, measurements were conducted to assess the effect of both the scan size (distance the probe moves in a measurement) and tip velocity (speed at which the probe moves). By holding the scan size constant and altering the tip velocity, it could be seen that the cantilever deflection increases with increasing tip velocity. This is shown in Figure 5.3.

The pattern of increasing deflection with tip velocity was not unexpected, as there is a velocity dependent dynamic force acting in this system. As the speed of the cantilever (and hence the speed of the droplet) was increased, the dynamic force increased. This is analogous to drag force curves where the dynamic drag is related to the velocity with which an object moves.

The cantilever deflection also showed some variability with scan sizes. This was explored by holding the tip velocity constant (for this a moderate tip velocity of $15\mu m/s$ was set) and varying the scan size.

The relationship between cantilever deflection and scan size is illustrated in Figure 5.4, which shows that there is an increase in the cantilever deflection until a certain scan size. Thus there exists a minimum scan size that must be used in order to conduct a measurement. In Figure 5.4 a scan size of $50\mu m$ would be required to properly measure the droplet; which was found to be sufficient to measure all droplets with volumes less than approximately

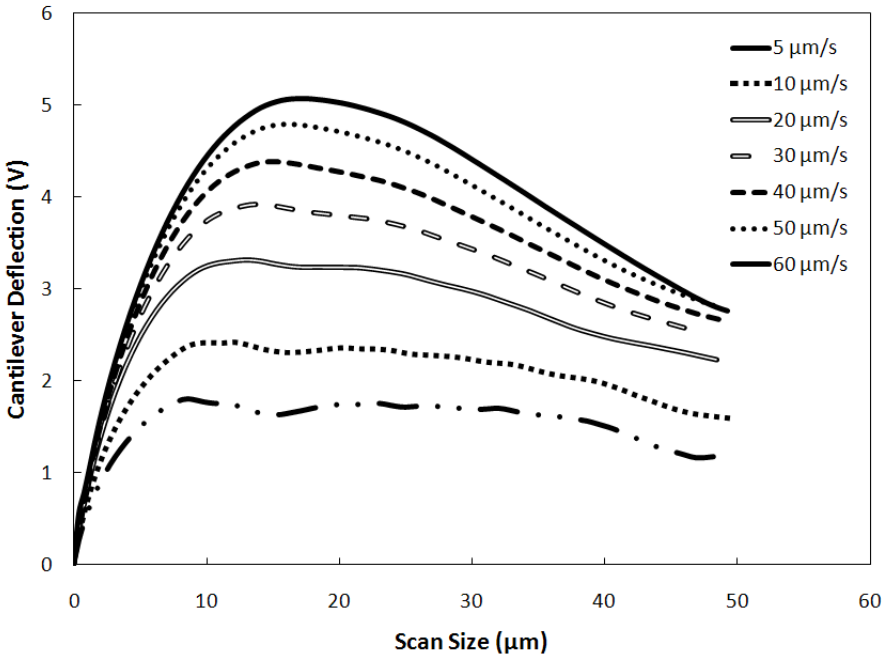

Figure 5.3: The influence of tip velocity (u_t) on the measured cantilever deflection

900000 μm^3, with larger droplets requiring scan sizes of up to 70 μm.

It seems that below a certain (critical) scan size that droplet deformation is being measured and not (yet) displacement. In some of these measurements it appeared that after the probe had commenced movement the droplet would 'race' to catch up with the probe (likely in response to a deformation of the contact line) as opposed to moving more steadily with the probe. Once the minimum scan size has been reached it seems that the droplet movement commences as a result of elastic deformation of the droplet and not some other effect, so it is then the force that is required to move the droplet that is being measured. Therefore using a scan size above this minimum value will allow the total cantilever deflection to be measured for a particular tip velocity. It should then be possible to measure a given droplet over a range of tip velocities and to then determine the force required to move a coalesced liquid droplet form its stationary (stable) position on a fibre.

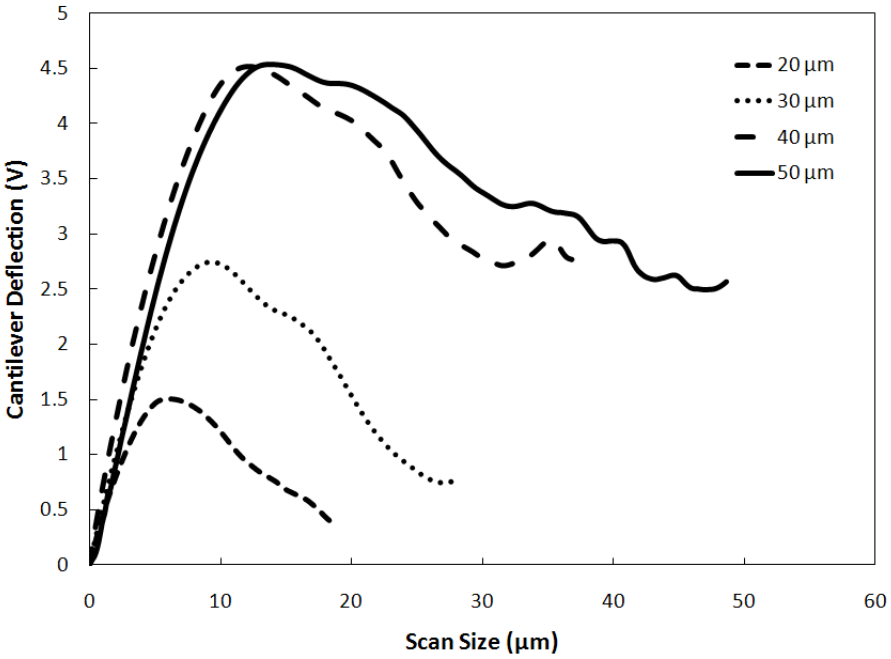

Figure 5.4: The influence of scan size on the measured cantilever deflection

Ultimately the point of interest in these cantilever deflection plots is the deflection that corresponds to the point where the movement of the droplet begins and is therefore the point that corresponds to the force that is required to move a coalesced liquid droplet. Figure 5.5 shows the measured cantilever deflection over a scan size of 50 μm. The cantilever deflection corresponding to the point at which the droplet begins to move is identified. It is this value that may be converted to a force, by using the force calibration parameter. The force given will consist of both a static and dynamic component.

Given the nature of the preparation of the coalesced liquid droplets, it was difficult to do repeat measurements starting from a clean fibre, as the volume of individual droplets is subject to some variation, depending on the rate at which aerosol is produced and the time that the fibre is exposed to the aerosol. However, each droplet measurement is in fact the average of a

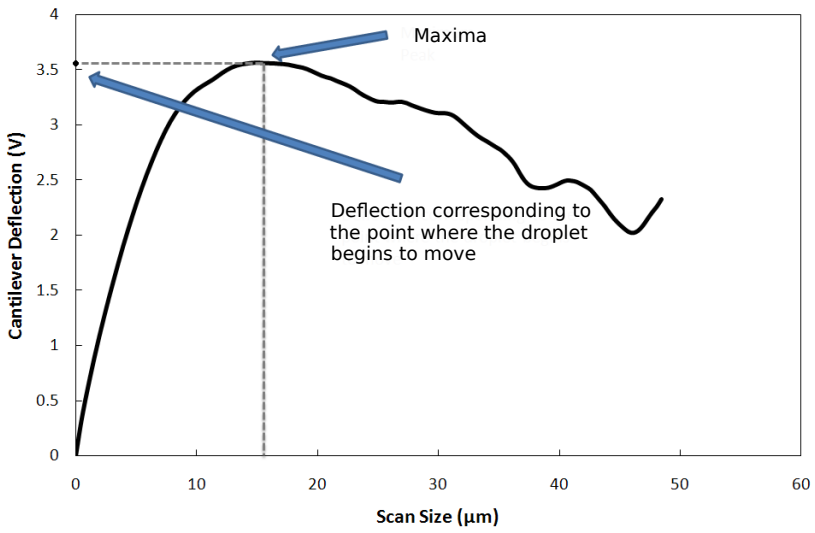

Figure 5.5: A plot of deflection vs. cantilever displacement for a coalesced droplet

number of successive droplet measurements. Furthermore, it is possible to dis-engage the probe and re-engage it to conduct a repeat set of measurements. This requires that the droplet remains on the fibre when the probe is dis-engaged. A repeat measurement of this nature is shown in Figure 5.6.

The slight variation between the initial and repeat measurements shown in Figure 5.6 is likely due to the probe being re-engaged in a slightly different position on the droplet. This is due to there being a small amount of 'play' in the mechanism that moves the cantilever into position.

During the measurements, droplets may merge, this happens if the scan size in use is less than the distance between the engaged droplet and a neighbouring droplet. While this is not desired during the course of a measurement where the force required to move a specific droplet is being measured, it is of interest in itself. This is because during the filtration process a coalesced liquid droplet may commence motion along the fibre and contact a neighbouring droplet, merging with it and this new larger droplet can continue moving on the fibre towards the next droplet.

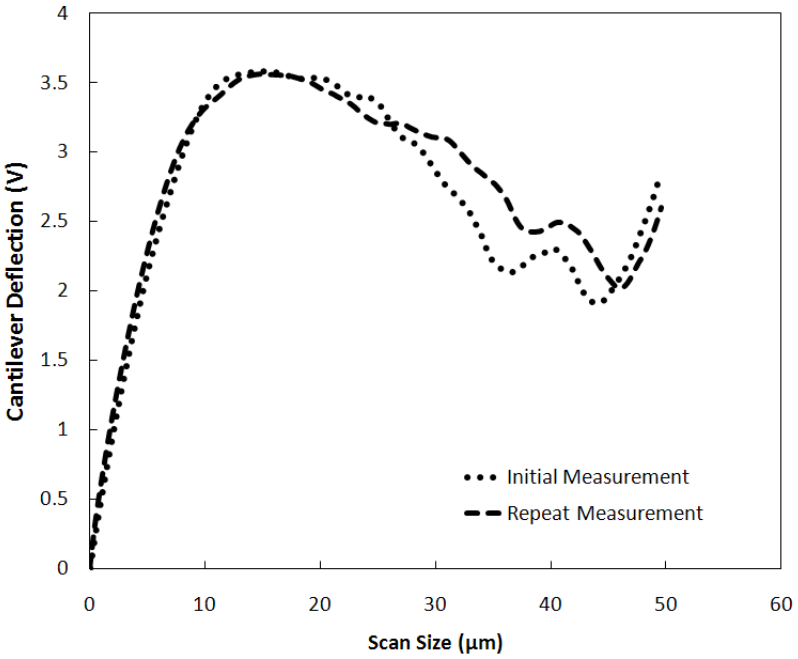

Figure 5.6: An initial droplet measurement and a repeat measurement conducted after dis-engaging and re-engaging the probe

Figure 5.7 shows a series of images of a droplet that has been engaged by a probe and is being moved along the fibre. Figure 5.7a through to Figure 5.7d shows the droplet being progressively moved along the fibre, until the engaged droplet is almost in contact with the droplet directly next to it (indicated by the arrow in the image). At this point the droplet only needs to be moved a very small distance before it comes into contact with the neighbouring droplet. When the engaged droplet, as shown in Figure 5.7d is advanced slightly, the droplet immediately next to it suddenly merges with it and forming a single, larger droplet. This merged droplet is shown in Figure 5.7e, which also indicates that there is a small residual droplet (indicated by the arrow) in the original location of the upper droplet droplet in Figure 5.7d. In this situation, when the cantilever is dis-engaged (provided that the droplet stays on the fibre) the droplet will immediately move along the fibre to a new stable position, as dictated by the Plateau-Rayleigh instability

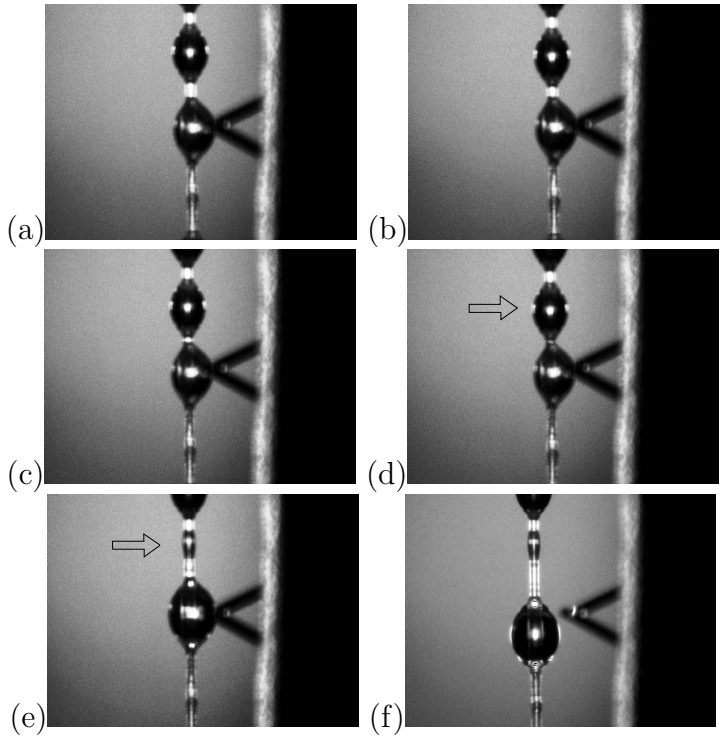

Figure 5.7: A series of images showing one droplet being moved progressively closer to another droplet. The droplet immediately above the droplet engaged with the cantilever then moves downwards to coalesce with the lower droplet (here it is the cantilever, and attached droplet, that moves; the fibre and camera form a fixed frame of reference)

frequency. This can be seen in Figure 5.7f.

The small residual droplet, as shown in Figure 5.7e, is not an effect of the measurement and actually represents the behaviour displayed in droplet-fibre systems; Dawar and Chase (2008) observed a similar residual droplet after the merging of droplets in the presence of flow. This is possibly due to the droplet being drawn into the engaged droplet by an attractive force, which is not great enough to overcome the forces holding the residual component of the droplet on the fibre. In a filter such, a scenario could occur when a droplet begins moving down a fibre due to drag forces imparted on it by the air flow. Once it moves close enough to a neighbouring droplet for the

attractive forces to act, the droplets would merge, leaving the small residual droplet.

Additionally, if the merged, engaged droplet is moved over the residual droplet, it will be taken up into the droplet and can no longer be seen on the fibre when the engaged droplet is moved away. Therefore, in a mist filter with droplets draining down a fibre and successively collecting droplets on the way, it seems likely that the residual droplets will be formed during the merging of droplets and be collected by the drainage of other droplets.

5.4 Conclusion

This Chapter has shown that it is possible to measure the force required to move a coalesced liquid droplet along a fibre. It has also examined the factors affecting the measurement (choice of sphere size, minimum scan size) and how these need to be accounted for. A coalesced liquid droplet in a barrel, clamshell or transitional conformation may be measured using this method, provided it is not overly large in size. Given that the maximum measurable deflection was exceeded during some measurements on larger fibres, this method appears to be limited to measuring droplets on fibres with diameters of less than 30 μm. Provided that an appropriate scan size is selected and a 'good' cantilever engagement is achieved, it is possible to reliably measure the force required to move a coalesced liquid droplet along a fibre. The measurement of the force required to move these droplets is the subject of the following Chapters (6-8).

6 Evaluation of the Force Required to Move a Coalesced, Oleophillic Liquid Droplet Along a Fibre

6.1 Introduction

The dynamics of wetting has received significant attention (deGennes, 1985; Semal et al., 1999) and remains of interest today (Seveno et al., 2009). However, previous work has predominantly considered droplets on flat surfaces, with comparatively little work on cylindrical elements (such as fibres).

Chapter 4 has illustrated, that while useful, modelling fibrous filters at a "capillary scale" does not provide sufficient resolution to accurately resolve all facets of their behaviour, without the use of (semi-) empirical corrections. Therefore, a smaller scale approach will be taken, that of a single fibre.

Given the complex (random) structure of fibrous filters (as illustrated in Figure 2.1) this single fibre approach provides a simple method of examining the fundamental behaviour of an otherwise complicated system. Accordingly, it is this approach that has been adopted in the study of the movement of coalesced liquid droplets along a fibre.

A number of previous studies of droplets on fibres have dealt with the stability of droplet conformations, contact angles and droplet geometry (Bauer and Dietrich, 2000; Brochard, 1986; Carroll, 1986, 1984, 1976; McHale and Newton, 2002; McHale et al., 1997; Quere et al., 1988). Some of these works detail the measurement of the contact angle of a droplet on a cylindrical fibre (Bauer and Dietrich, 2000; Wagner, 1990; Carroll, 1976) (which is different to the contact angle the same liquid would form on a flat plate (deGennes, 1985; Bacri et al., 1988; Quere et al., 1988)) as well as providing equations describing the profile of a droplet (Yamaki and Katayama, 1975; Carroll, 1976). Using the equations of Carroll (1976), the reduced droplet volume

($\overline{V}$) and volume of the droplet (V), the wetted area of the fibre and the wetted length (L) (distance between contact lines) can be determined numerically from the known contact angle (θ), fibre radius (h) and droplet radius (measured perpendicular to the fibre (x_2)). The reduced volume can be defined as,

$$\overline{V} = \frac{V}{h_r^3} = \frac{2\pi n}{3}[(2a^2 + 3an + 2n^2)E(\phi, k) - a^2 F(\phi, k) + \frac{1}{n}(n^2 - 1)^{\frac{1}{2}}(1 - a^2)^{\frac{1}{2}}] - \pi\overline{L} \tag{6.1}$$

where $E(\phi, k)$ and $F(\phi, k)$ are elliptical integrals of the first and second kind, respectively, and $\overline{L}$ is the reduced wetted length,

$$\overline{L} = 2[aF(\phi, k) + nE(\phi, k)], \tag{6.2}$$

with the parameter a (used to simplify the rather complicated expression for the profile of a droplet (Carroll, 1976)) defined as

$$a = \frac{x_2 \cos\theta - h_r}{x_2 - h_r \cos\theta}, \tag{6.3}$$

and the reduced radius (n_r) as

$$n_r = \frac{x_2}{h_r}. \tag{6.4}$$

Using these equations, however, relies on the contact angle being known or measurable, as Equation 6.3 depends on the value of θ. Direct measurement of the contact angle from a fibre image is not always reliable as there is a high degree of curvature at the fibre-liquid interface (Rebouillat et al., 1999). The contact angle can be calculated from the Carroll (1976) equations if the wetted length, L is known, however this may be difficult to measure accurately as the exact boundary of the droplet is difficult to detect optically. However, the inflection method of Rebouillat et al.1999 allows the contact

angle of a droplet on a fibre to be determined from an image, without the need to measure L. Using the equation for the profile of a droplet Carroll (1976); Yamaki and Katayama (1975), the relationship between the inflection angle (θ_i) (i.e. the angle between the fibre and the point on the droplet that has maximum slope) and the contact angle can be established (Rebouillat et al., 1999), where

$$a_i = n_r(1 + 2\tan^2\theta_i) \pm n_r((1 + 2\tan^2\theta_i)^2 - 1)^{\frac{1}{2}}, \tag{6.5}$$

and

$$\theta = \frac{((1 - n_r^2)(a_i^2 - 1))^{\frac{1}{2}}}{n_r a_i + 1} \tag{6.6}$$

with $a_i < 1$.

Here a_i is a modified value of a used to derive the relationship between θ and θ_i.

It is therefore possible to measure all necessary parameters for the equations from an image of the droplet, which allows the comparison of force measurements of different droplets to a chosen droplet parameter.

By using the methodology described in Chapter 5, this Chapter will detail the determination of the forces required to slide a droplet along a fibre both theoretically and experimentally using the AFM.

6.2 Model

For the purposes of modelling the force required to move a droplet from its static position on a fibre, an axisymmetric droplet situated on a cylinder of radius h_r, oriented horizontally, as shown in Figure 6.2, will be considered. The centre of mass, G, of the coalesced droplet may be displaced a distance r from the centre of the fibre (so for a droplet at its axisymmetric rest position, where the effects of gravity are negligible, $r = 0$). Here b, is the radius of the droplet defined as the distance from G to the contact line in contrast to the

value of x_2 which is the perpendicular distance from the centre of the fibre to the droplet edge (these values are different as the droplets are not perfectly spherical). In the case where $r = 0$, b is half the wetted length (distance between contact lines). The position of a point on the contact line around the fibre can then be expressed in terms of

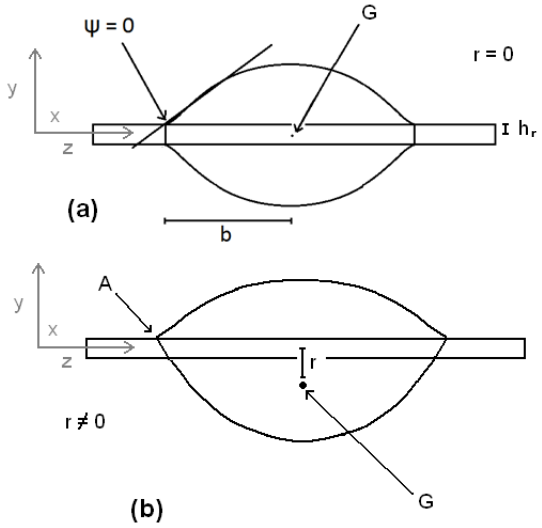

Figure 6.1: Schematic representation of the model parameters with the droplet (a) at the axisymmetric rest position and (b) displaced from this position by a distance *r*. The x axis is perpendicular to the yz-plane and the origin is at the centre of mass, G.

$$x_A = h_r \sin(\psi), \tag{6.7}$$

$$y_A = r + h_r \cos(\psi), \tag{6.8}$$

$$z_A^2 = b^2 - r^2 - h_r^2 - 2rh_r \cos(\psi), \tag{6.9}$$

where ψ denotes the angular position on the contact line around the fibre, so $0 \leq \psi \leq 2\pi$.

If we consider the position vector ($\underline{r}_A$) of a point A on the contact line we

get:

$$\underline{r}_A = \underline{i}h\sin(\psi) + \underline{j}(r + h\cos(\psi)) + \underline{k}(b^2 - r^2 - h_r^2 - 2rh_r\cos(\psi))^{\frac{1}{2}}, \quad (6.10)$$

where *i, j, k* are the component vectors.

The tangent plane to the droplet at point A is given by

$$\underline{r} \cdot \underline{u}_A = b, \quad (6.11)$$

where $\underline{r}$ is the position vector of a point in the tangent plane and

$$\underline{u}_A = \frac{\underline{r}_A}{|\underline{r}_A|} \quad (6.12)$$

is a unit vector normal to the droplet at A. The normal to the fibre $\underline{u}_f$ at A is given by

$$\underline{u}_f = 2(x_A)\underline{i} + 2(y_A - r)\underline{j} + W\underline{k}. \quad (6.13)$$

The tangent plane, perpendicular to the contact line at A, may be displaced by $\underline{v}s$ such that,

$$\underline{r} = \underline{r}_A + \underline{v}s \quad (6.14)$$

where s is a parameter and the vector $\underline{v}$ has the form,

$$\underline{v} = 2\underline{i}x_A + 2\underline{j}(y_A - r) + \underline{k}W. \quad (6.15)$$

If the conditions,

$$\underline{v} \cdot \underline{u}_A = (2\underline{i}x_A + 2\underline{j}(y_A - r) + \underline{k}\,W) \cdot \frac{\underline{r}_A}{|\underline{r}_A|} = 0 \tag{6.16}$$

are met then

$$W = \frac{2x_A^2 + 2y_A^2 - 2ry_A}{z_A}. \tag{6.17}$$

The vector $\underline{v}$ at A acts in the direction of the surface tension at A and is normalised to provide a unit vector $\hat{\underline{v}}$ for each value of ψ and therefore for all points around the contact line.

This normalised vector is then,

$$\hat{\underline{v}} = \frac{2\underline{i}x_A + 2\underline{j}(y_A - r) + \underline{k}\,W)}{[4x_A^2 + 4\,(y_A - r)^2 + W^2]^{\frac{1}{2}}}. \tag{6.18}$$

The force required to move the droplet from its static (stable) position will then be a function of $\hat{\underline{v}}$ and the advancing (τ_a) and receding (τ_r) line tensions, such that

$$F_m = \int_0^{2\pi} \tau_a \hat{\underline{v}}\, d\psi + \int_0^{2\pi} \tau_r \hat{\underline{v}}\, d\psi, \tag{6.19}$$

where $z_A > 0$ for the advancing and $z_A < 0$ for the receding contact lines and must be real. The line tensions are

$$\tau_a = 2h_r \pi\sigma \cos\theta_a, \tag{6.20}$$

for the advancing and

$$\tau_r = 2h_r \pi\sigma \cos\theta_r, \tag{6.21}$$

for the receding boundaries, with σ being the surface tension of the liquid and θ_a and θ_r being the advancing and receding contact angles, respectively.

6.3 Experimental

Given that the methodology has been described in Chapter 5, the experimental methods used will only be discussed here briefly.

This work required the preparation of modified cantilevers, since the contact between the AFM probe and the droplet needed to be sufficiently large that the droplet could be moved along the fibre with the AFM probe and secondly, it was found that the surface of the AFM probe needed to be rendered oleophobic to ensure that the droplet remained on the fibre and did not attach to the cantilever. These two criteria were achieved by mounting a colloidal probe with a surface coating on to a cantilever. A glass sphere was attached to the cantilever (NP-OW, tipless silicon nitride cantilevers, Veeco, Camarillo, USA) using an epoxy resin (Araldite, Selleys, Australia). The surface of the attached sphere was then coated with a fluorinated co-polymer (TL1143, Thor Chemie, Speyer, Germany) rendering it oleophobic. The size of the coalesced droplet which could be moved by a cantilever was found to depend on the size of the glass sphere attached to the cantilever. For this work, a series of cantilevers were prepared using glass spheres ranging from 20-70 μm in diameter.

The fibres (9.1, 10.2, 12.5, 17, 22.7 μm diameter polyester, Barnet, Aachen, Germany) were mounted individually in a custom made stainless steel mount (SS 304) so that a length of approximately 50 mm of fibre was held rigidly, 5 mm above the base of the mount. The fibres were then loaded (with oil) by exposing them to oil-aerosol generated by a Collision Nebuliser. Hence the fibres were allowed to collect the oil in the same manner they would in a mist filter. The size of the coalesced droplets that accrete on the fibre was dependent on the time that the fibre is exposed to the aerosol stream. The

Table 6.1: Oil properties

	DEHS (A)	RX Super (B)
density (ρ) kg/m^3	914	875
viscosity (μ) $Pa.s$	0.025	0.131
surface tension (σ) N/m	0.0324	0.0295

oils used in this work were (A) a mono-component laboratory oil di-ethyl-hexyl-sebacate (DEHS, Sigma-Aldrich, USA) and (B) a multi-component commercial lubricating oil RX Super (Castrol, Australia). The properties of these oils are given in Table 6.3.

The contact angles of these oils on the fibre were determined using the 'inflection method' of Rebouillat et al. (1999) from images taken with a CCD camera. The droplet dimensions were determined optically and by using the Carroll (1976) equations evaluated in MATLAB (MathWorks, USA).

For the AFM measurements, a Digital Instruments Dimension 3100 Scanning Probe Microscope system with Nanoscope V6.13 control software (Veeco, California, USA) was used. All force measurements were taken using contact mode, whereas the topography of the fibre surface was imaged in tapping mode. The torsional spring constant of the cantilevers used was determined via the Torsional Sader method (Green et al., 2004) and the lateral signal sensitivity was measured according to the method of Cannara et al 2006.

The choice of cantilever calibration methods has been discussed in Section 5.2.4. The errors associated lateral force calibration using these methods (Palacio and Bhushan, 2010; Cannara et al., 2006; Green et al., 2004) are approximately $\pm$ 15%.

In order to move the droplets along the fibre and to measure the required force, the probe was moved at a scan angle of 90° with the slow scan axis disabled. Figure 6.2 shows the typical set-up for the measurements.
Approximately 10^3 droplet scans were conducted in order to produce the

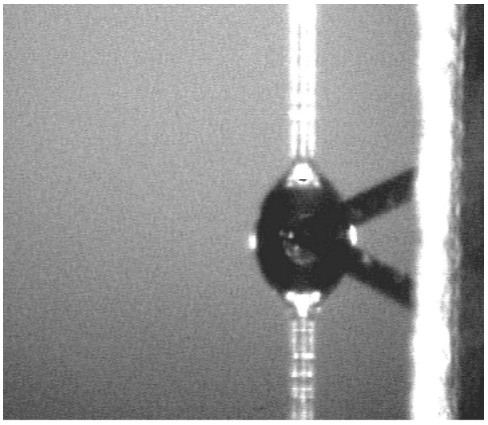

Figure 6.2: A coalesced droplet of oil B being measured on a 22.7 μm diameter fibre

results given in the following section.

6.4 Results and Discussion

For a detailed analysis of the force measurements, information on the dimensions of the measured droplets is required. The first step was to determine the contact angle of the coalesced droplets on each of the different fibre diameters. Figure 6.3 shows the contact angles for all the combinations examined in this work.

The contact angles of axisymmetric droplets of both oils were measured for each fibre diameter. A minimum of 20 droplets were measured for each oil-fibre combination, which were then averaged to give a representative static contact angle for each of the fibre diameters with each oil (see Figure 6.3). With respect to our model, dynamic contact angles would be preferred, however measurement of the dynamic contact angle is exceedingly difficult and for this work the static contact angles have been used. Figure 6.3 shows that there is little difference in contact angles for the two oils on each of the different fibre diameters, with the exception of the thinnest fibres where the difference becomes evident. Given the similar surface tensions of the oils, similar contact angles were expected, with the deviation at the small fibre

diameters perhaps being due to liquid surface tension forces having a greater influence as fibre diameter is decreased.

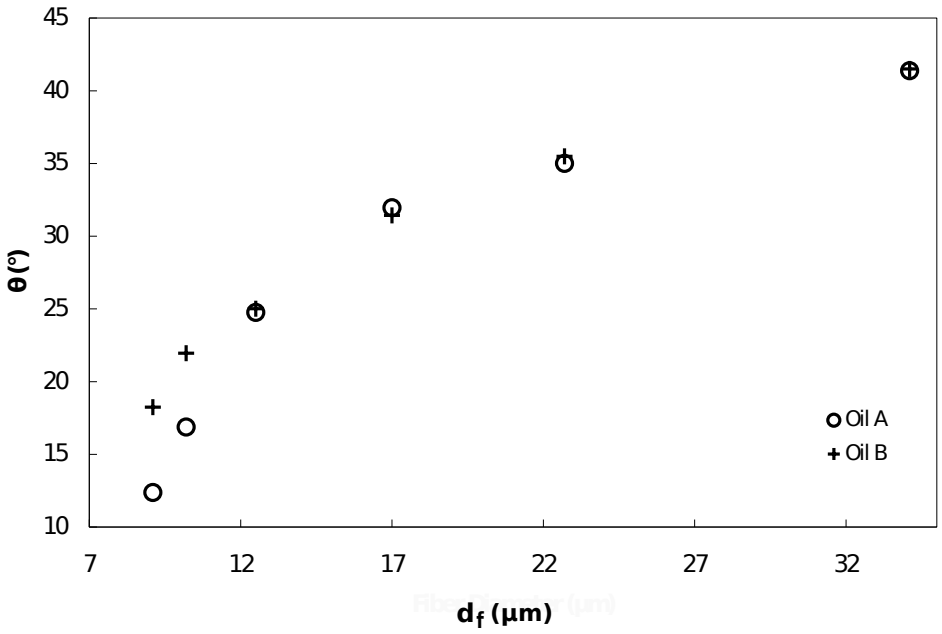

Figure 6.3: Static contact angles for each oil and fibre combination used in this work. Error bars indicating an average standard deviation of 1.5° are omitted for clarity

It was found that the force required to move a droplet on a fibre increased with increasing tip velocity, which is likely due to there being both a static and a dynamic component of the measured force. The dynamic (viscous drag) force component is dependent on tip velocity (u_t) and therefore is a result of measuring the force required to move a droplet, by actually moving it. The static component of the force (due to static friction/interfacial tension) though is the force holding the droplet in place and as such is present when the droplet is not in motion (i.e. when $u_t = 0$). By using velocities from as low as 0.8 μm/s and up to 50 μm/s a series of measurements were made

for each droplet so that the relationship between tip velocity and cantilever deflection could be found. The deflection corresponding to the movement of the droplet was extracted from each of the scans at the different tip velocities and converted to a force by multiplication with the force calibration factor, found using Equation 2.77. Resulting in a plot of force vs. tip velocity, as shown in Figure 6.4. It should be mentioned each of these points represents the force required to move the droplet and so elastic tension and the resultant droplet deformation have already occurred before the droplet moves and the force measurement is obtained.

Examination of Figure 6.4 reveals that there is an increase in the force with tip velocity, which can be described by a polynomial fit. For the case shown in Figure 6.4 the total force, F_t, is described by the polynomial fit,

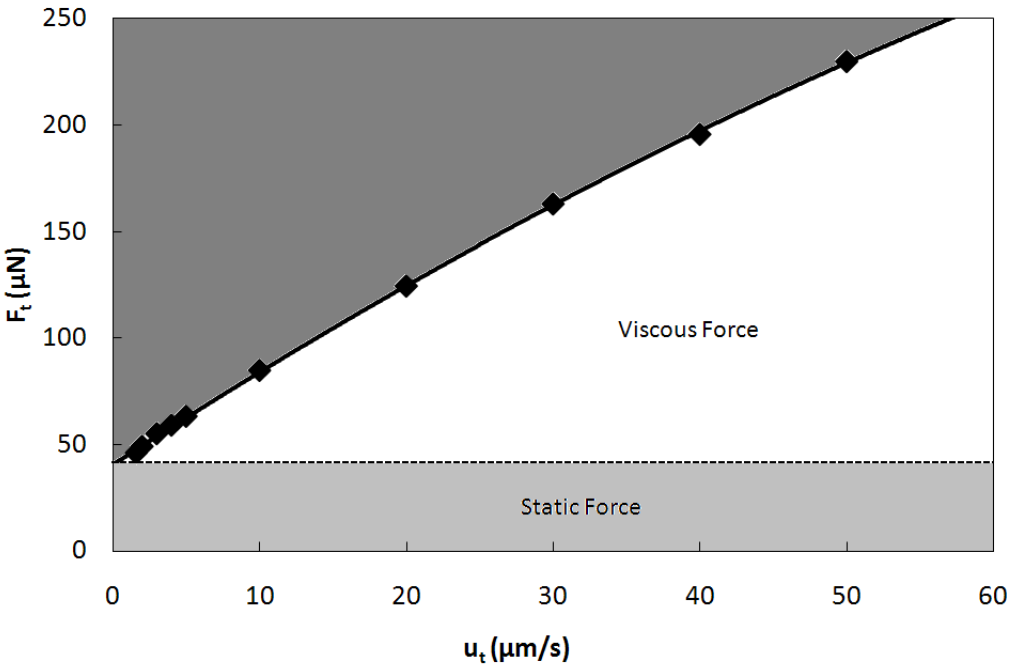

Figure 6.4: Force vs. tip velocity curve used for the static force determination; this is for a droplet on a 17 μm polyester fibre

$$F_t = -0.0144u_t^2 + 4.4962u_t + 40.605, \tag{6.22}$$

where u_t is the tip velocity and the fit has a correlation coefficient (R^2) of 0.99. Remembering that the force here consists of both a static and a dynamic component, Equation 6.22 can be evaluated as the value of u_t approaches 0, such that F_t approaches the force holding the droplet in place when there are no dynamic forces acting. For the droplet measured in Figure 6.4 it is 40.6 μN. This is the static/minimum force required to commence droplet motion.

The model was evaluated for droplets of the same dimensions as those measured using Equation 6.1 and Equation 6.2. The droplet parameters were determined using the value of x_2 measured directly from the droplet images and the contact angle data from Figure 6.3 corresponding to the oil type and fibre diameter being used. For the purposes of modelling the droplets the effect of gravity is considered to be negligible and $r = 0$ for all droplets. The model neglects the surface energy of the fibre as this affects the wettability and as such is intrinsic in the contact angle (which has been measured).

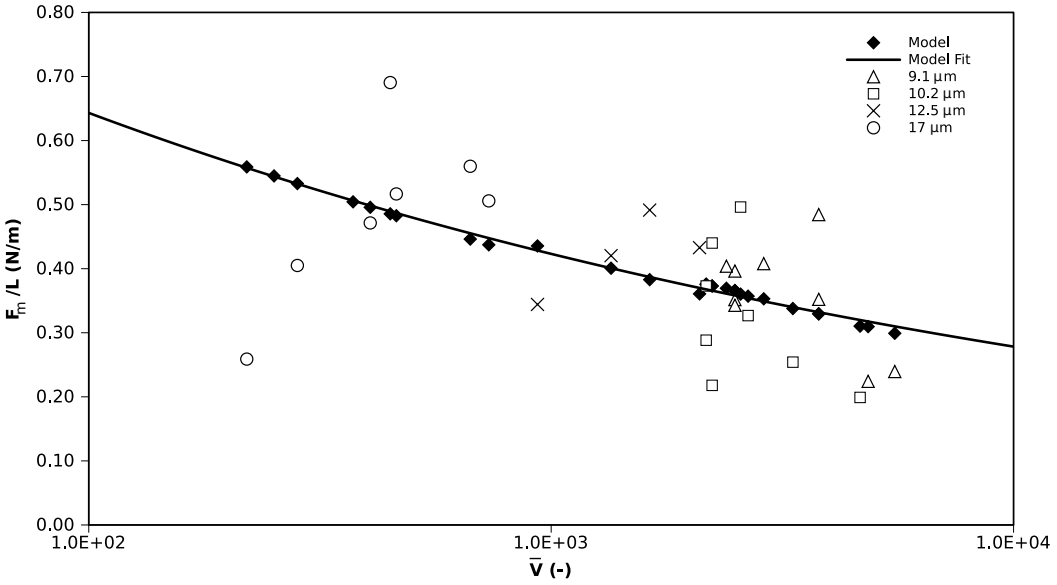

Figure 6.5: Measured and modelled static forces for coalesced droplets of oil A on 9.1, 10.2, 12.5 and 17 μm diameter fibres

Figure 6.5 and Figure 6.6 show the results plotted in terms of force over wetted length vs. reduced droplet volume (as defined by Equation 6.1). This allows all the results for the different fibre diameters to be plotted on the same set of axes. For oil A the correlation coefficient (R^2) between measured and modelled values is 0.77 and for oil B 0.82.

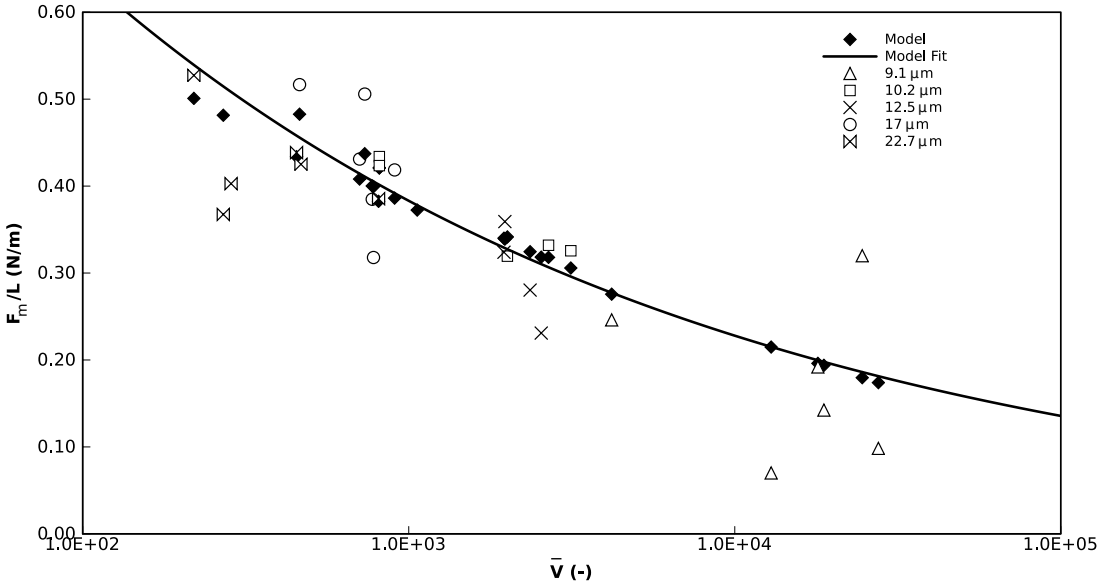

Figure 6.6: Measured and modelled static forces for coalesced droplets of oil B on 9.1, 10.2, 12.7, 17 and 22.7 μm diameter fibres

Close examination of the modelled values revealed that an empirical fit could me made to the model data points. The best empirical fits were found using power laws. These are,

$$F_l = 6.8012\overline{V}^{-0.241}, \tag{6.23}$$

for oil A, and

$$F_l = 7.9946\overline{V}^{-0.282}, \tag{6.24}$$

for oil B, where F_l is the force per wetted length (F_m/L) and the correlation (R^2) between the modelled data and the power law fit is 0.99 for both oils. While we are able to determine all the values necessary for the model Equation 6.19 the empirical fits allow a simplified force determination, without the need for the numerical evaluation of the model. It is believed that these equations may be useful in fibrous filter (and other engineering) applications.

Therefore it is possible to determine the force required to move a coalesced droplet, of known dimensions, of oil A or oil B from its stationary position without the need to numerically evaluate the force model - or to evaluate the model for a reduced number of points.

Figure 6.5 and Figure 6.6 both show some scattering of data points in terms of the modelled values and the model fit, this is not unexpected as we are dealing with droplets of different wetted lengths on different diameter fibres with contact angles that vary over the different fibre diameters. It is also possible that measurement errors associated with the determination of the droplet dimensions may affect the model.

The variation between modelled and measured forces for both oil A and oil B are due to a number of factors. The error associated with the force calibration of the cantilevers must of course be considered, but also there are two possible explanations for this based on experimental observations and measurements. Firstly, the fibres are not smooth cylinders, they are polymer fibres manufactured using the melt-blown process and contain surface inhomogeneities which will affect the length and shape of the contact line, wetted area and ultimately the force required to move the droplet. Figure 6.7 shows the three-dimensional tapping mode AFM topography image of a randomly selected fibre section, where the surface irregularities can clearly be seen.

Secondly, it was observed that during some measurements that the droplet appeared to move into contact with the sphere on the cantilever while the

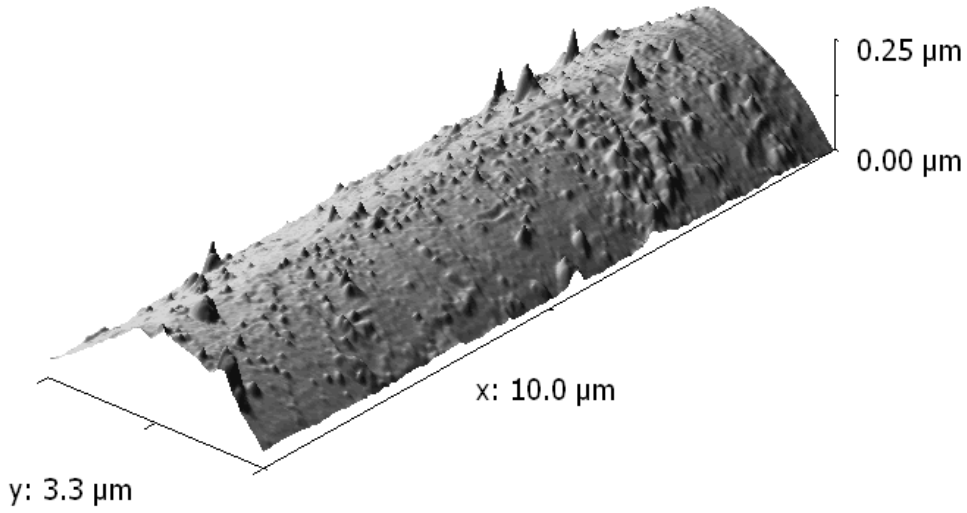

Figure 6.7: The topography of a section of the surface of a 17 μm diameter polyester fibre

cantilever was still approaching the fibre. This leads to a situation where the droplet is no longer in the axisymmetric rest position (i.e. $r \neq 0$) and the force measured is no longer the force required to move the droplet from its original (static) position, but from a slightly off centre static position. This is important both in terms of explaining differences between measured and modelled values and also in terms of the behaviour of mist filters. It has been observed in fibrous filter systems that under the influence of air flow a droplet may be pushed away from its preferred position (see Figure 6.8).

The effect of the droplets shifting away from their axisymmetric rest position was investigated by deliberately pulling the droplet to the side of the fibre with the cantilever and measuring the force required to move the droplet

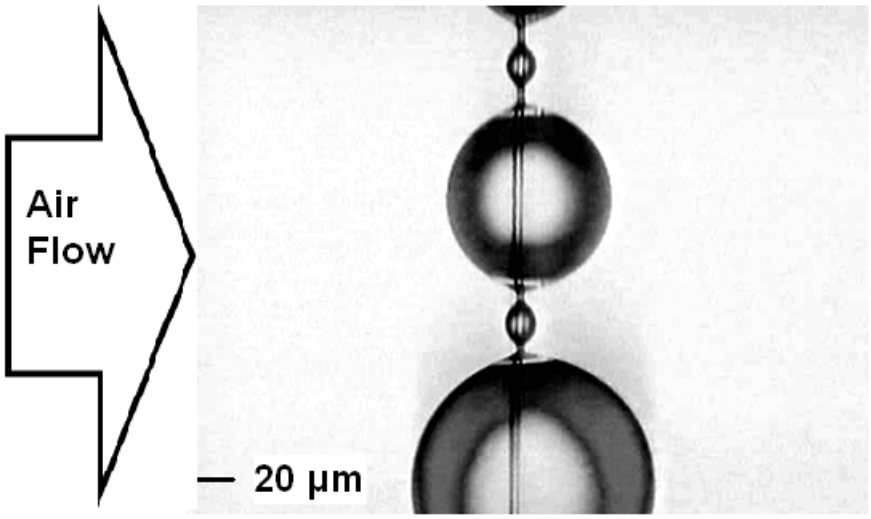

Figure 6.8: Coalesced droplets on a fibre subject to air flow (Mullins et al., 2006). The displacement from the preferred axisymmetric position is evident.

along the fibre, from this new position. This was also modelled by varying r in the model. A comparison of the experimental and modelled data is shown in Figure 6.9.

Figure 6.9 shows a gradual deviation between the measured and modelled values with increasing r. This is likely because the contact angle may vary at different points around the fibre as when r is increased the symmetry of the droplet around the fibre will be lost. Both modelled and measured values do however demonstrate that as the value of r increases the force required to move the droplet from its static position decreases. This may have practical applications in mist filtration as it implies that the onset of droplet drainage (motion) could be brought forward by increasing the flow velocity through the filter and moving the coalesced droplets away from their stable (rest) positions.

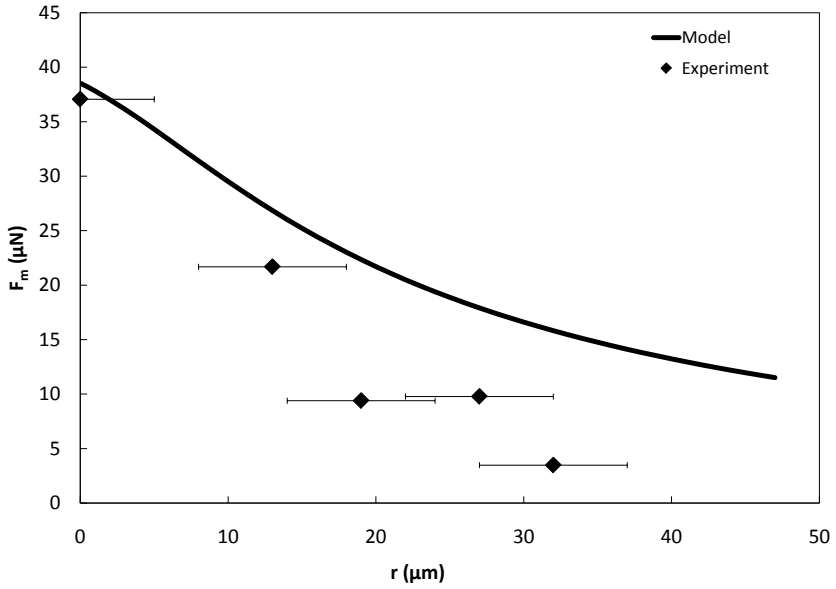

Figure 6.9: Influence of increasing droplet displacement (r) on force (F_m)

6.5 Conclusion

The force required to move a coalesced liquid droplet along a fibre from its stable stationary position has been measured. A good agreement between the measured force values and those predicted by the model was found and the factors which may influence the static force have been identified. These include fibre surface inhomogeneity and displacement of the droplet from the axisymmetric rest position. The influence of pulling the droplet away from the fibre on the force required to move it along the fibre has also been established. It is expected that the theoretical model presented would show very close agreement with measured data if atomically smooth fibres could be obtained and AFM measurement error neglected.

Additionally, empirically derived equations have been given for the specific cases examined, which allow calculation of the force required to move a droplet on a fibre, based on the reduced volume, without the need to solve the theoretical model numerically. The theoretical model requires h_r, b, θ and σ as input to calculate the force.

As shown, the model conforms to a power law relationship for the cases evaluated in this work. This implies that for a new case, the model can be evaluated for a relatively small number of points and the power law fitted to obtain a range of values. Chapter 8 will examine coalesced oil droplets on different fibre materials.

Furthermore, the force required to move 'clamshell' droplets (i.e. droplets on oleophobic fibres) will be discussed in Chapter 7.

7 Examination of Liquid Droplets Collected on Oleophobic Fibres

7.1 Introduction

The behaviour of liquid droplets on hydrophobic and super-hydrophobic surfaces is of significant interest and has received much attention (Jagdheesh et al., 2011; Lee and Owens, 2011; Lee et al., 2011; Marmur, 2004). However, most of the previous work in this area focuses on flat surfaces, with comparatively few studies examining curved surfaces (such as those on a fibre). Surfaces that are hydrophobic, are also typically oleophobic (typically to a lesser extent), which provides a means of studying '-phobicity' without having to contend with the evaporation of water, or work in 100% humidity environments.

Droplets which form on phobic surfaces may be characterised as being 'clamshell' shaped and have contact angles $> 90°$ which result from the liquid being unable to 'wet' the surface. If the droplets have contact angles $> 150°$ then the surface is considered super-()-phobic.

This non-wettability makes oleophobic or hydrophobic fibres an attractive option for use in industrial mist-filters or mist eliminators, which typically become 'clogged' with liquid during operation, as in theory phobic fibres may provide more effective drainage. Mist eliminators are commonly used in industry to remove water droplets in spray towers.

Unlike oleophillic media the droplets formed will not be axisymmetric and will typically be present in far greater numbers of much smaller volumes. The droplets formed are classified as 'clamshell' shaped and may range from spherical caps, through to near perfect spheres, depending on the contact angle between the droplet and the fibre.

Existing models for mist filters tend to focus on predicting macroscopic prop-

erties such as saturation (Raynor and Leith, 2000) and pressure drop (Raynor and Leith, 2000; Frising et al., 2005). These models are of a (semi-) empirical nature and are only applicable over a narrow set of parameters (oil type, fibre diameter, packing density and others). Given that there is much conjecture about whether it is better to use oleophillic or oleophobic fibres (Agranovski and Whitcombe, 2000; Agranovski et al., 2001), perhaps a more fundamental approach is needed which focuses on the behaviour of coalesced droplets on oleophobic fibres.

Therefore, by considering droplets on a single fibre, the droplet-fibre relationship can be studied and will allow comparisons to be made directly between oleophillic and oleophobic fibres. This single fibre approach has also been used in the modelling of filter capture efficiency (Hinds, 1999; Lee and Liu, 1981, 1982).

In Chapter 5, a method was developed to measure droplet-fibre forces using an AFM, and was applied to oleophillic fibres in Chapter 6. This Chapter extends the methods and models developed in those Chapters to the measurement of phobic systems.

7.2 Theory

It is difficult to describe 'clamshell' droplets on fibres mathematically, as determining the length of the contact line involves finding the length of a curved line around a curved surface and the variation in the contact angle at different points around the droplet is unclear. Additionally, unlike axisymmetrical droplets (where the profile is known in terms of elliptic integrals (Carroll, 1986; McHale et al., 1997; McHale and Newton, 2002)). there is no known solution to the Laplace equation for the non-axisymmetric case (McHale and Newton, 2002). Using a Finite Element approach, McHale and Newton (2002) were able to approximate the 'clamshell' shape by specifying droplet volume and contact angle. These were however, only preliminary re-

sults and were more concerned with droplet stability and the 'roll-up' process than with expressing the dimensions of the droplet, which would be useful in this work.

The force model presented in Chapter 6 for droplets on oleophillic fibres may, however, be able to be applied to droplets on oleophobic fibres, provided that the differences between the two cases can be accounted for.

This model equation is given below, for the full description and development refer to Chapter 6.

$$F_m = \int_0^{2\pi} \tau_a \underline{\hat{v}} d\psi + \int_0^{2\pi} \tau_r \underline{\hat{v}} d\psi, \tag{7.1}$$

where F_m is the force required to move a droplet from its stationary position on the fibre.

Included in the model derivation is a variable r, which defines the distance of displacement of a droplet's centre of gravity from the centre of the fibre. In the case of an axisymmetric droplet the value of r will be zero; unless a force acts on the droplet, thereby displacing it from its equilibrium (stable) position. The value of r is also limited by the criterion that the value obtained from the model must be real. As such the value of r can not be increased indefinitely. In practical terms this means that r cannot be greater than the droplet radius minus the fibre radius.

Given the that the model was developed for axisymmetric droplets there are limitations that will effect its applicability to 'clamshell' shaped droplets. In order to apply it, a value of r should (ideally) be used corresponding to the distance that the centre of mass of the droplet is from the centre of the fibre. This value however, is likely to be too large and will result in complex numbers. Therefore the largest permissible value of r should be used if the true distance is too large. In order to apply the model a contact line length

Table 7.1: Oil properties

	DEHS (A)	RX Super (B)	Glycerol (C)
density (ρ) kg/m^3	914	875	1262
viscosity (μ) $Pa.s$	0.025	0.131	1.2
surface tension (σ) N/m	0.0324	0.0295	0.064

is also required. Given that to the authors' knowledge there is no method available to determine the length of the contact line for 'clamshell' droplets, the length of the contact line is approximated as that of an axisymmetric droplet. The contact angles used should be those of the liquid droplet on the fibre.

7.3 Experimental

The AFM required the use of colloidal probes with an oleophobic surface coating, this has been detailed in Section 6.3.

Polyester fibres (9.1, 10.2, 12.5, μm diameter, Barnet, Aachen, Germany) were mounted individually in a custom made stainless steel mount (SS 304) . The fibres were then coated in place in the mounts, with a fluorinated co-polymer (TL1143, Thor Chemie, Speyer, Germany), to render them oleophobic. Filter fibres are commonly rendered oleophobic industrially by coating them in this manner. The coated fibres were then loaded (with oil) by exposing them to an oil-aerosol generated by a Collision Nebuliser. The size of the coalesced droplets that accrete on the fibre was dependent on the time that the fibre is exposed to the aerosol stream. The oils used in this work were (A) a mono-component laboratory oil, di-ethyl-hexyl-sebacate (DEHS, Sigma-Aldrich, USA), (B) a multi-component commercial lubricating oil RX Super (Castrol, Australia), both used in Chapter 6, and (C) Glycerol (Sigma-Aldrich, Australia). The properties of these oils are given in 7.3.

As previously, the AFM measurements were conducted using a Digital Instru-

ments Dimension 3100 Scanning Probe Microscope system with Nanoscope V6.13 control software (Veeco, California, USA) was used. The torsional spring constant of the cantilevers used was determined via the Torsional Sader method (Green et al., 2004) and the lateral signal sensitivity was measured according to the method of Cannara et al. (2006).

7.3.1 Statistical Methodology

Bayesian linear regression was used to determine the relationship between the force (F_m) required to move a droplet and the other measurable parameters. A Bayesian statistical method was chosen as it allows the type of distribution of each of the variables to be defined; as opposed to assuming that all variables conform to a normal distribution.

The observed force was modelled as y_i ~Normal (μ_i, σ^2) and y_i ~Log-Normal (μ_i, σ^2), where y_i is the force (F_m) for *i=1...N* observations. For the model with all oil types $\mu_i = \alpha_0 + \alpha_1 \times d_f(\mu m) + \alpha_2 \times V(\mu m^3) + \alpha_3 \times d_s(\mu m) + \alpha_4 \times c_l + \alpha_5 \times oiltype + \alpha_6 \times fibre$. Where α_0 is the intercept, and both oil type and fibre are dummy variables denoting the presence/absence of a particular oil type or fibre. The models for each oil type, $x_i = \alpha_0 + \alpha_1 \times d_f(\mu m) + \alpha_2 \times V(\mu m^3) + \alpha_3 \times d_s(\mu m) + \alpha_4 \times c_l + \alpha_5 \times fibre$. The coefficients ($\alpha_i$(i=0....6) were modelled as Normally distributed, α ~Normal *(0,* σ^2), where σ^2 was set to a large constant, thus all coefficients were treated as non-informative priors. Bayesian regression was performed using Markov chain Monte Carlo (MCMC) using WinBUGS 1.4.3. Convergence of models was assessed using all convergence diagnostics in the CODA package (Best et al., 1995). From these diagnostics the burn-in selection for all models was 10,000 iterations and a further 500,000 iterations were used to estimate the parameters α_i. The deviance information criterion (DIC) and model predictions were used to compare between the two models (Normal and Log-Normal) (Gelman et al., 2004).

7.4 Results and discussion

Initial measurements revealed that it was often difficult to avoid (undesired) probe-fibre interaction. This was due to the glass spheres on the probe are of comparable size to the droplets themselves and smaller spheres do not give sufficiently strong contact to move the droplets and because there is a high degree of surface roughness on the fibre. Thus an examination of the coating applied to the fibre was needed.

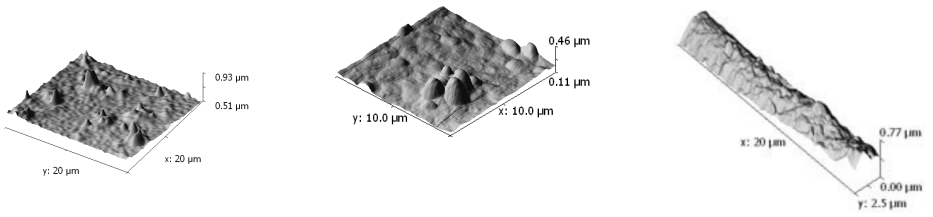

(a) (b) (c)

Figure 7.1: Topography of a piece of mica, spin coated with copolymer solution at 3000 rpm (a) and 2000 rpm (b) and the topography of a coated fibre (c)

It is known from Chapter 6, that the surface of the uncoated fibre has a number of asperities and hence is not smooth; and that this influences the force required to move a coalesced droplet. To examine the influence of the polymer surface coating, an identical coating was applied to both the fibres and to pieces of mica. Mica was chosen as it is atomically flat and therefore any roughness that appears after the coating will be due to the curing properties of the polymer. To examine this, pieces of mica were spin-coated with the polymer solution at different rotation speeds.

Figure 7.1a shows the surface coating on mica with a rotation speed of 3000rpm and Figure 7.1b shows the surface coating at 2000rpm. Both clearly demonstrate that the surface coating is non-uniform. We may therefore conclude that if, on a flat surface, the surface coating has a high degree of

roughness then on a fibre that is not smooth the coating will act to exacerbate the roughness of the surface (the effect of which can be seen in 7.1c). Therefore in this work the roughness of the surface will be significant, however since oleophobic fibres are typically prepared in industry by applying surface coatings, similar degrees of surface roughness will be present in filters made up of oleophobic fibres. This results in another variable which must be accounted for. This has been achieved by using fibre replicates (i.e. different sections of fibre, which will have differing 'roughnesses' as the surfaces are non-uniform, were used for the series of measurements).

Determining the contact angle of a 'clamshell' shaped droplet on a fibre can also be problematic, so as a starting point the contact angle on a flat surface was considered. This surface was the mica, spin-coated at 3000rpm, and so was not a smooth surface. A sessile drop of each oil on the coated mica is shown in Figure 7.2.

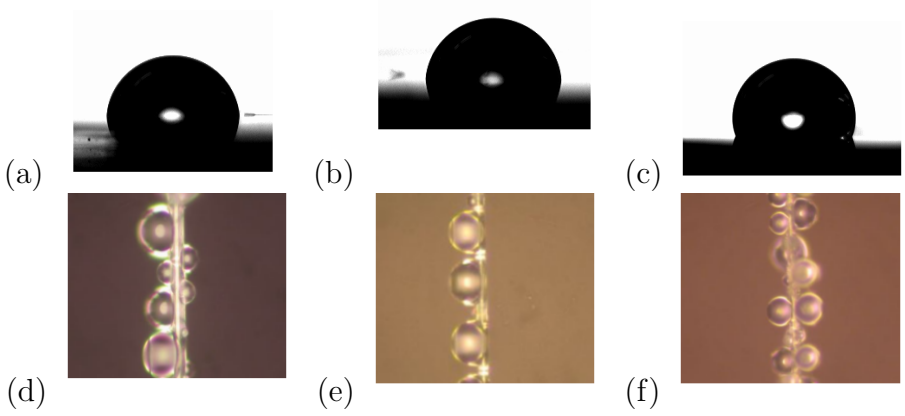

Figure 7.2: Sessile drops of Oil A (a), Oil B (b) and Oil C (c) on a polymer coated mica surface and coalesced droplets of Oil A (d), Oil B (e) and Oil C (f) on coated fibres

Figure 7.2 shows that the contact angles for oils A and B are similar, while the contact angle for Oil C is noticeably larger. On the coated mica the average contact angle was found to be 86° for Oil A, 88° for Oil B and 110°

for Oil C. The contact angles on the fibres are difficult to determine, as the images only show part of the droplet. The remainder of the droplet may extend beyond the field of view, so it is difficult to determine if a contact angle measured form an image, is in fact the actual contact angle. However, the droplets appear to have a qualitatively similar contact angle on the fibre.

In order to examine the effects of the fibre replicates, an exploratory data analysis using principal component analysis (PCA) and linear regression was conducted to determine the amount of variability in data which could be accounted for by the fibre replicates and the significance of the other variables. This analysis revealed that the most significant parameter in the measurement was the fibre replicates (i.e. a high degree of variability between fibres of the same size and material was found, which was not present in the work presented in Chapter 6, which used uncoated fibres of the same type); therefore fibre roughness has a significant influence on the force required to move a coalesced droplet on an oleophobic fibre. Also significant was the size of the sphere present on the probe, this in fact was just as significant as the fibre diameter. The significance of the surface roughness and the sphere diameter as indicated by the PCA, confirms the interpretation of our observations.

In order to apply the Bayesian regression, values for each of the variables likely to influence the force are required. The droplet volume and length of the contact line are difficult to determine accurately so are approximated. As these variables were found to be the least significant in the PCA, we do not anticipate that the approximation will have a significant influence on the models.

The general form of the Bayesian model is

$$logF = -\beta_b + \gamma_b d_f + \epsilon_b V + \delta_b d_s - \omega_b l_c + \chi f_x \tag{7.2}$$

where d_f is the fibre diameter, V is the droplet volume, d_s is the sphere

Table 7.2: Coefficients for each oil type for the Bayesian model

Coefficient	Oil A	Oil B	Oil C
β_b	-5.674	31.4	354.3
γ_b	17.68	-4.136	-39.21
ϵ_b	0.009591	2.91×10^{-5}	1.08×10^{-4}
δ_b	3.781	0.232	0.1277
ω_b	-5.775	0.02347	-0.02382

Table 7.3: Coefficient values for the fibre replicates

f_x	f_a	f_b	f_c	f_d	f_e	f_f	f_g	f_h	f_i
χ	0	-0.6816	3.82	4.461	14.05	13.4	0	46.31	-69.44
f_x	f_j	f_k	f_l	f_m	f_n	f_o	f_p	f_q	f_r
χ	-28.7	-57.45	39.67	17.43	0	-0.01508	1.209	45.49	45.71
f_x	f_s	f_t	f_u	f_v					
χ	45.21	135.2	134.5	135.6					

diameter, l_c is the length of the contact line, f_x designates the fibre replicate and the values of the coefficients for each oil are given in 7.2. To apply the model the appropriate value for the fibre replicate was chosen from 7.3. The model only requires the value of the fibre replicate being used to be input. Therefore, the value of f_x is 1 for the fibre being used and zero for all others.

The Bayesian model for Oil A is not logged as, owing to the large number of fibre replicates and low number of measurements on each replicate, it had to be evaluated differently. The Bayesian statistical models produced, predict the measured force quite well, as can be seen in Figures 7.3, 7.4 and 7.5. Also included in these figures is a power law fit to the statistical model and values calculated using the theoretical model, originally presented in Chapter 6. The power law has been chosen as it was used in Chapter 6. The theoretical model is applied by using a non-zero value of R. The droplet volumes here are expressed in terms of a reduced volume ($\overline{V}$) so that measurements on different diameter fibres may be directly compared.

Figure 7.3 shows how well the Bayesian regression fits the measured data.

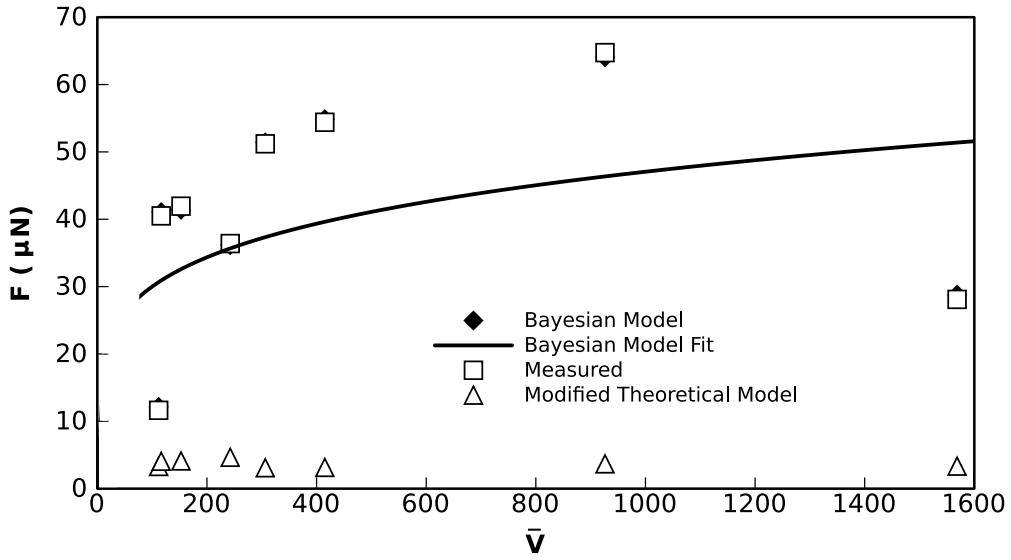

Figure 7.3: Measured and Predicted forces for Oil A on the coated fibres

There is however a significant disparity between the measured/regression data and the theoretical model. This is not unexpected, as the theoretical model was derived for axisymmetric, not clamshell shaped droplets. There are therefore a number of limitations. Firstly, the maximum value permitted for r is approximately $r_d - r_f$; which still corresponds to a droplet that surrounds the fibre, though moved away from a central position. Secondly, the shape of the contact line is different as it consists of a single continuous length, which does not surround the fibre.

For both Oil A and Oil B the values predicted by the theoretical model are much less than the measured values. This is partly due to the model being used outside of its original purpose and also due to the value of r being limited in the model, as when r becomes too large, a complex number results. The r values used then correspond to a droplet that still partially surrounds the fibre, as opposed to one that sits on the fibre surface. Thus, the value predicted by the theoretical model is expected to be lower.

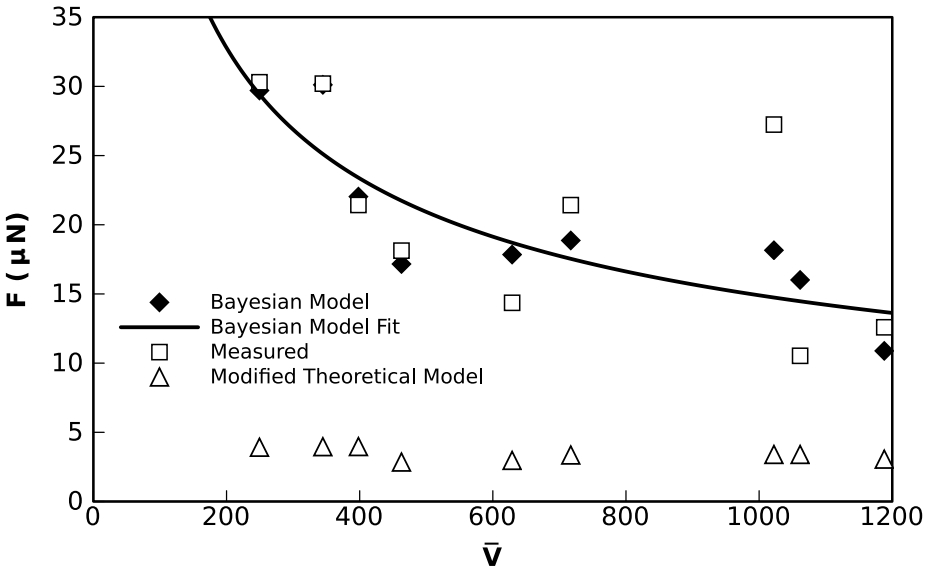

Figure 7.4: Measured and Predicted forces for Oil B on the coated fibres

Taking the deficiencies of the model (in this application) into account then, the disparity between the model predicted values in 7.3 and 7.4 must be due to another factor. Given that the roughness of the fibre surface is not incorporated in the model and the coated fibres are very rough, this is the logical source of the disparity.

The effect of this (very) rough fibre surface would be to increase the wetted area of the fibre and therefore the force required to move the droplet. This is however in contrast to the results shown in Figure 7.5, where the model predicted values are in fact greater then the measured values. Taking into account the limited value of r which can be used in the model, it is expected that the force required to move a droplet would continue to decrease as the value of r was increased outside the limits of the model. Therefore the force would decrease and approach the Bayesian regression fit line.

The key difference between Oil C and Oils A and B is the surface tension. The surface tension of Oil C is twice that of the other oils, the effect of which

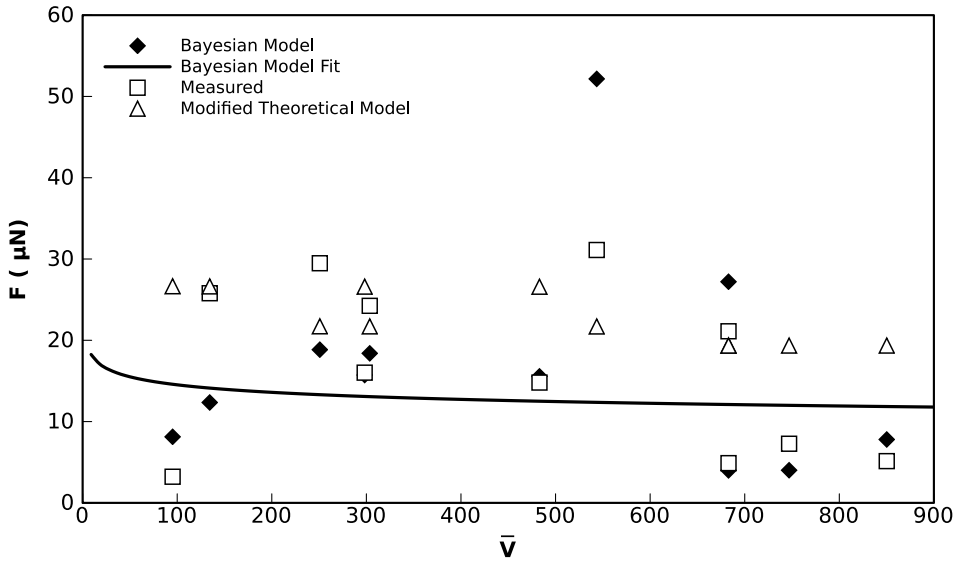

Figure 7.5: Measured and Predicted forces for Oil C on the coated fibres

is manifested in the shape/contact angle of the droplet. The Oil C droplets closely approximate spheres and so sit on the fibre surface. As the fibre surface is quite rough and the surface tension high, the droplet may not be in contact with the whole surface area of the fibre on which it sits. Therefore the effects of the increased fibre surface area due to roughness would not be present in the force measurement. Essentially, this means that Oils A and B homogeneously wet the contact area on the fibre surface, where as for Oil C, the contact area is wetted heterogeneously.

This explanation is further supported by examination of the deviance information criterion (DIC) (Gelman et al., 2004). When the Bayesian-regression model is generated, both with and without the sphere diameter used as a variable, the results can be compared to indicate the influence of the sphere diameter on the force. For these measurements the DIC indicated that for Oil C, the sphere has no significant effect and the presence of the sphere diameter in the regression model does not effect the force. However, for Oil A and Oil B, the sphere diameter does effect the force. This can again be

explained by the surface tension of Oil C being lager than that of Oil A and B.

Alternatively there is another possible explanation, that of contact line pinning. This would again be due to the different surface tension of Oil C in relation to Oils A and B. For Oils A and B then, contact line pinning is present and as such the measured values are much higher then the values predicted using the modified theoretical model. In the case of Oil C, this pinning effect is not present and as such the measured forces are closer to the model predicted forces. Some evidence of this may be seen in 7.6, where images taken during the force measurement are shown.

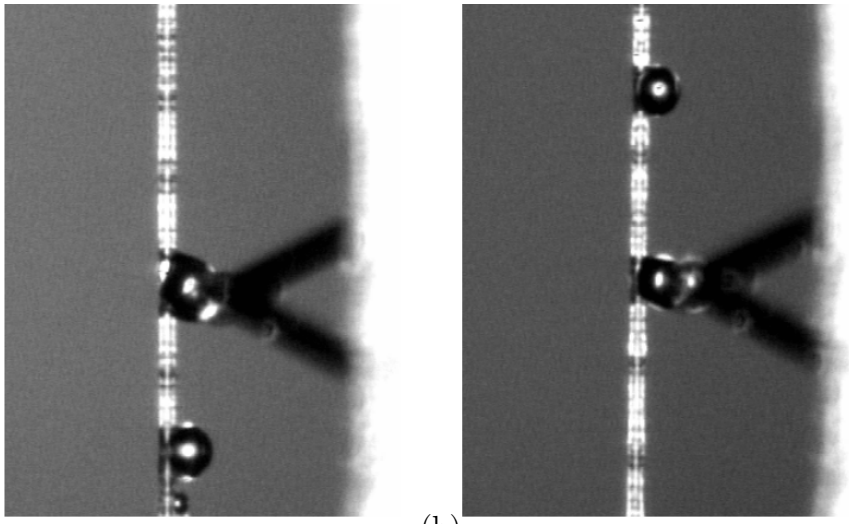

(a) (b)

Figure 7.6: Images of a droplet of Oil B (a) and a droplet of Oil C taken whilst the measurement was in progress. The droplet of Oil B appears to stick to the fibre and become slightly distorted; whereas the droplet of Oil C appears to retain its near spherical shape.

Figure 7.6(a) shows a droplet of Oil B being moved along the fibre (here the cantilever is moving from the top to the bottom). The droplet appears to 'stick' to the fibre and as such is distorted by the movement of the cantilever. In Figure 7.6(b) a droplet of Oil C is shown (with the cantilever moving from top to bottom). The droplet retains its near spherical shape through out the

measurement and does not appear to stick to the fibre in the same way as droplets of oils A and B.

A few of the measured data points in Figures 7.4 and 7.5 differ from the values predicted by the Bayesian regression. This potentially means they are statistical outliers, as Bayesian methods do not typically work well for these values.

The measured forces on the coated (oleophobic) fibres may be compared to measurements conducted on uncoated (oleophillic) fibres in Chapter 6. Figure 7.7 shows the measurements on the coated and uncoated fibres with Oil A and Figure 7.8 the results for Oil B.

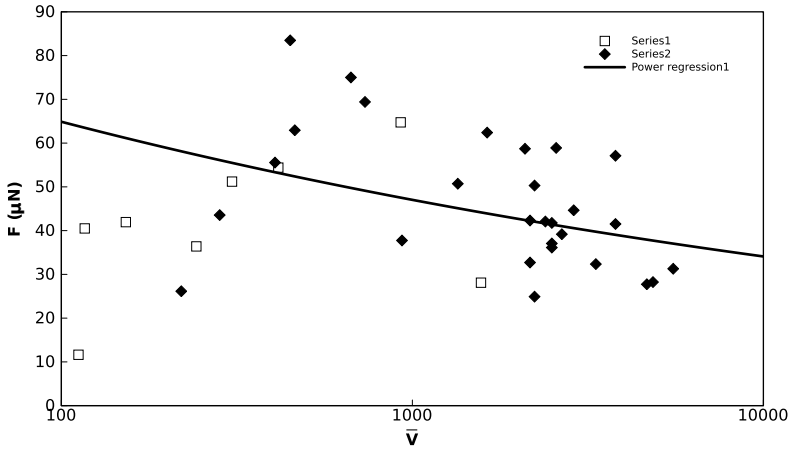

Figure 7.7: Force required to move coalesced droplets of Oil A along coated and uncoated fibres

In Figure 7.8 a clear difference is evident between the measurements on oleophillic and oleophobic fibres. It appears that the force is simply reduced by a common factor, which may be seen directly by comparison of the power law fits. For oil B it appears that for droplets of the same reduced volume the force required to move them is 1.6 times greater on oleophillic fibres than it is on oleophobic fibres. This difference is not so apparent in Figure 7.7 where there is some overlap of the results. It does appear though that the

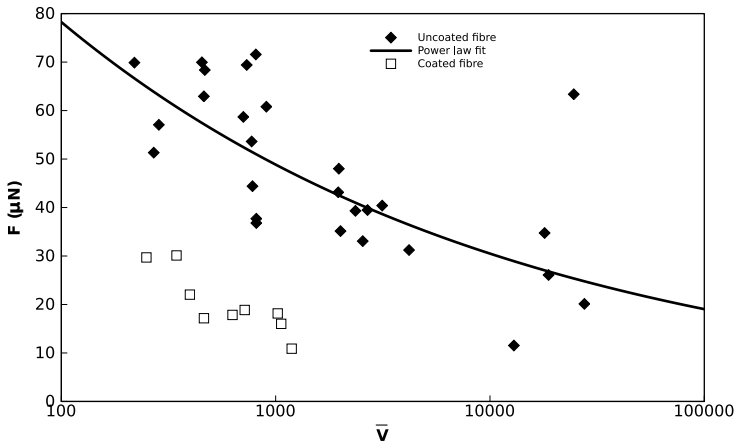

Figure 7.8: Force required to move coalesced droplets of Oil B along coated and uncoated fibres

force required to move a droplet of Oil A will be greater on an oleophillic fibre than on an oleophobic fibre.

In terms of mist filters, this implies that oleophobic fibres may imbue the filter with better drainage properties and perhaps a lower equilibrium saturation. This however would possibly come at the cost of increased levels of re-entrainment, as if it is easier for the droplets to drain from the fibre it will be easier for them to be blown off the fibre and returned the air stream.

7.5 Conclusion

It has been shown that, when measuring the force required to move an oil droplet along an oleophobic fibre, the surface roughness of the fibre is a significant factor, as is the wetting behaviour of the liquid. Additionally using the current method, the effect of the AFM probe must also be considered. These factors aside, it has been demonstrated that the Bayesian-regression is a useful tool to obtain useful conclusions from such measurements. Furthermore, it has been found that an estimate of the force required to move a droplet along the fibre may be obtained by adapting the theoretical model,

developed in Chapter 6, (outside its originally intended application), provided there is homogeneous wetting of the contact area and/or the effects of contact line pinning are minimal. It has been found that in general, less force is required to move a liquid drop along an oleophobic fibre, than an oleophillic fibre.

8 Examination of the Effect of Fibre Material and Particulate Matter on the Force Required to Move a Coalesced Droplet Along a Fibre

8.1 Introduction

Fibrous filters are typically made up of fibres made from polyester, glass-fibre or stainless steel, all of which have their own unique surface properties. As such, the contact angles formed by coalesced oil droplets on fibres with different surface energies will vary. Also the amount (and nature) of surface roughness will vary, which will influence the force required to move a coalesced droplet from its stationary (stable) position. Therefore, it is likely that there will be a relationship between the force required to move a coalesced liquid droplet and the material from which the fibre is manufactured.

These differences in static forces will likely manifest, in the drainage properties of the filters from which they are made, and lead to different levels of filter saturation. Which, as discussed in Chapter 4 is a critical factor in filter design.

Also of interest, is the influence of particulate matter (such as soot) that may be present in the oil. Fibrous filters may be called on to filter aerosols where the liquid dispersed phase has been contaminated and the contaminants may influence the behaviour of the mist filter. Despite the significance this may have, particularly in diesel crank case filters (where the oil gradually becomes soot contaminated, up to the order of 2-5%) only the two studies (mentioned in Section 2.6) thus far have been carried out.

The examination of the influence of soot particles on the force required to move a coalesced droplet along a fibre, may therefore provide an insight into the influence of particulate matter on the drainage/saturation behaviour of

mist filters. Also of interest, is the behaviour of the soot, which may not stay suspended in the oil, but rather adhere to the fibre.

8.2 Experimental

In terms of measurements on the different fibre types, the procedure is the same as used in Chapter 6 (see Section 6.3). The work utilised glass-fibre (7.9 μm diameter, Barnet, Aachen, Germany and stainless steel (30 μm diameter, Bekaert, Ghent, Belgium) fibres. Given the relatively large size of the stainless steel fibres the 'STK' cantilevers were used for these measurements.

In order to examine the influence of particulate matter on the force required to move a droplet along a fibre, a solution of 'dirty' or sooty oil had to be prepared. For the purposes of this work, the soot-in-oil sample was prepared using a combination of oil A and printer toner (Printex U, Evonik, Hanau, Germany). The printer toner was used as it is essentially a fine power of carbon particles, which is much like the soot found in diesel engines, and has previously been used as a soot surrogate (Bredin et al., 2011).

The sooty oil was prepared in two different concentrations, with one at 1.5 % soot and the other at 2.5 % soot (weight per volume). These concentrations were selected, as they are soot concentrations that may typically be encountered by crank-case filters. Higher concentrations are unlikely as the oil is changed to prevent abrasion to the engine.

8.3 Results and Discussion

The contact angles formed by the oils on the glass-fibre and stainless steel fibres were measured in the same way as those in Chapter 6. For the glass-fibre media the contact angles were 11.9° and 13.9° for oils A and B, respectively. For the stainless steel fibres, the contact angles for both oils was 33.2°. This is likely due to the relatively large fibre diameter, as evidenced by Figure 6.3, where the contact angles of different oils appear to converge with increasing fibre diameter.

8.3.1 The Effect of Fibre Material

Given that the fibres made of different materials all have different diameters, comparison between the fibre materials is best carried out using the reduced droplet volume, as used in Chapters 6 and 7.

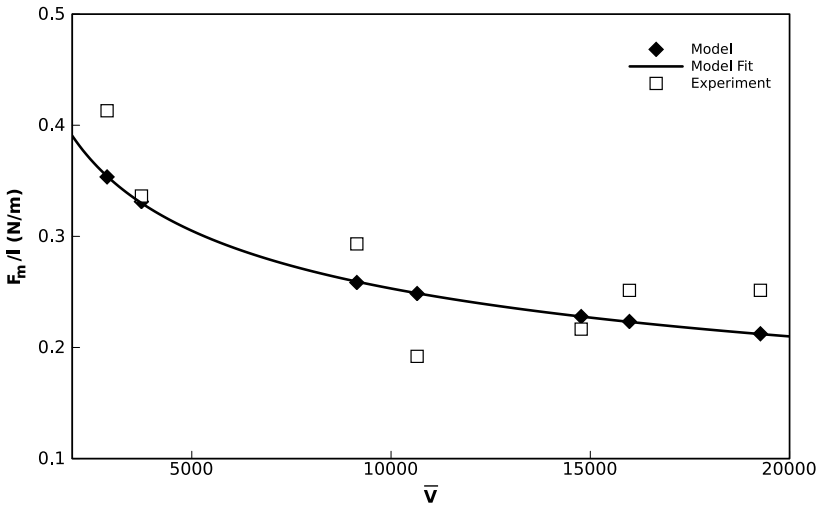

Figure 8.1: Measured and modelled static forces for coalesced droplets of oil B on a 7.9 μm diameter glass fibre

A 7.9 μm diameter glass fibre was used for the measurements, with droplets of both oil A and oil B being used. The results are shown in Figures 8.1 and 8.2, with the results presented in the same manner as in Chapter 6.

As with the results shown in Chapter 6, a power law can be fitted to the modelled values. The power laws can be described by the equations,

$$F_l = 3.028\overline{V}^{-0.269}, \tag{8.1}$$

for Oil A and

$$F_l = 2.158\overline{V}^{-0.238}, \tag{8.2}$$

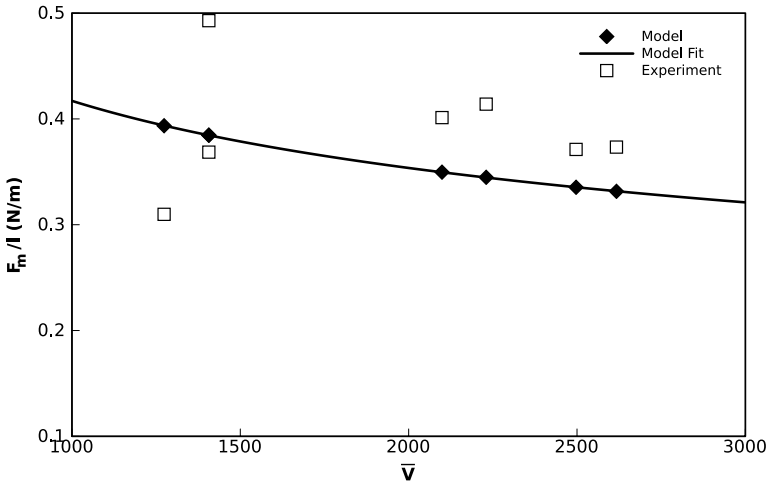

Figure 8.2: Measured and modelled static forces for coalesced droplets of oil B on a 7.9 μm diameter glass fibre

for Oil B. The R^2 for both Equations 8.1 and 8.2 is 0.99.

Measurements were also conducted using a 30 μm stainless steel fibre, again using both oil A and oil B. The results are shown in Figures 8.3 and 8.4.

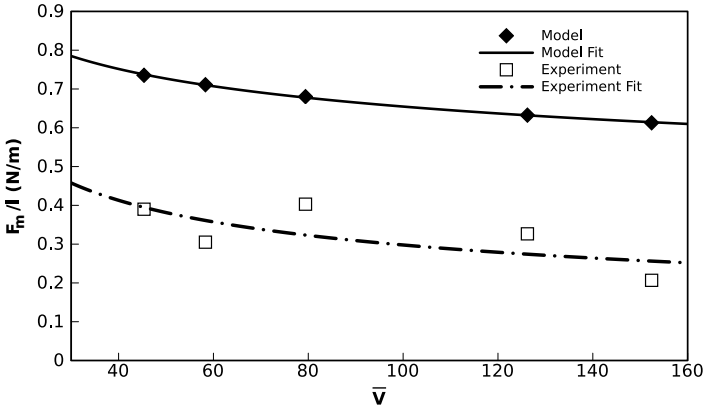

Figure 8.3: Measured and modelled static forces for coalesced droplets of oil A on a 30 μm diameter stainless steel fibre

As with the other measurements, a power law has been fitted to the modelled values. The power laws may be described by the equations;

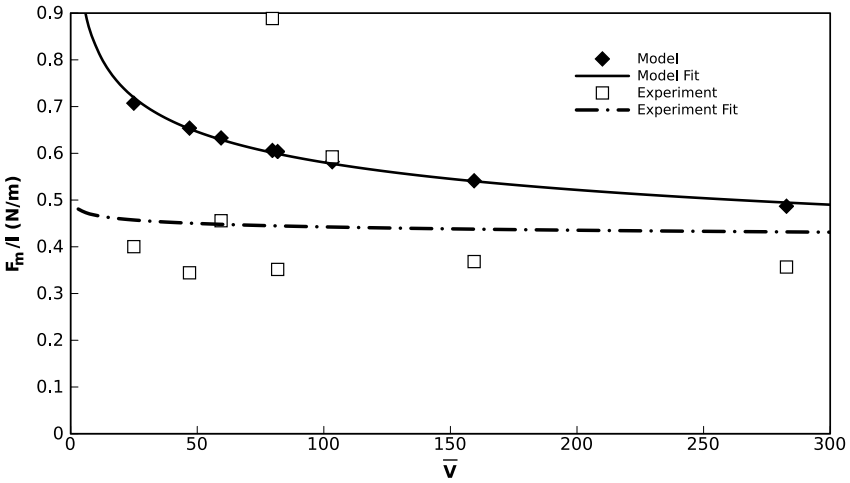

Figure 8.4: Measured and modelled static forces for coalesced droplets of oil B on a 30 μm diameter stainless steel fibre

$$F_l = 1.311\overline{V}^{-0.151} \tag{8.3}$$

for oil A and,

$$F_l = 1.329\overline{V}^{-0.178}, \tag{8.4}$$

for oil B. With the R^2 values for both Equations 8.3 and 8.4 being 0.99.

The measurements on the stainless steel fibre, were somewhat limited by the diameter of the fibre. In Chapter 5, it was stated that the upper measurement limit was a fibre diameter of 30 μm. This can be seen in Figures 8.3 and 8.4 where the majority of the measured values fall below the modelled values. For this reason a power law fit has also been applied to the experimental data in Figures 8.3 and 8.4. In Figure 8.3 the power law fit to the experimental data appears as if it is a translation of the power law fit to the the model data. This is primarily due to the effect of r; where the droplet has been pulled away from the fibre by the cantilever. This was necessary

on this larger fibre diameter in order to get the droplet to move. In Figure 8.4 the power law fit also appears shifted, most likely due top the effect of r. However, the power law fit to the experimental data is different in appearance to that of the fit to the model, as it is distorted by the two data points that lie above the model fit line. It is likely that these two measurements correspond to droplets that sat on a particularly rough section of the fibre.

Also present to some degree is probe-fibre interaction. As the fibre is relatively large, the coalesced droplets formed are also large. These larger droplets require a larger sphere size on the probe and in some cases the sphere is large enough that it unintentionally interacts with the fibre while the droplet is being moved.

As was the case in Chapters 6 and 7, the surface roughness of the fibre also influences the force measurements.

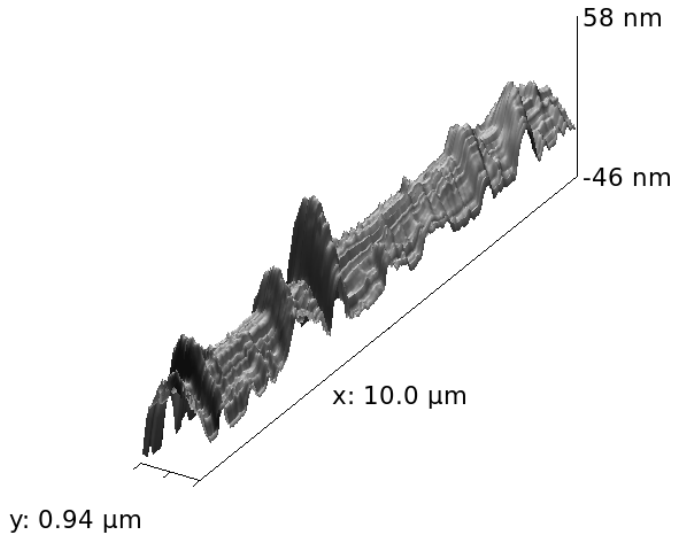

Figure 8.5: The topography of the glass-fibre surface

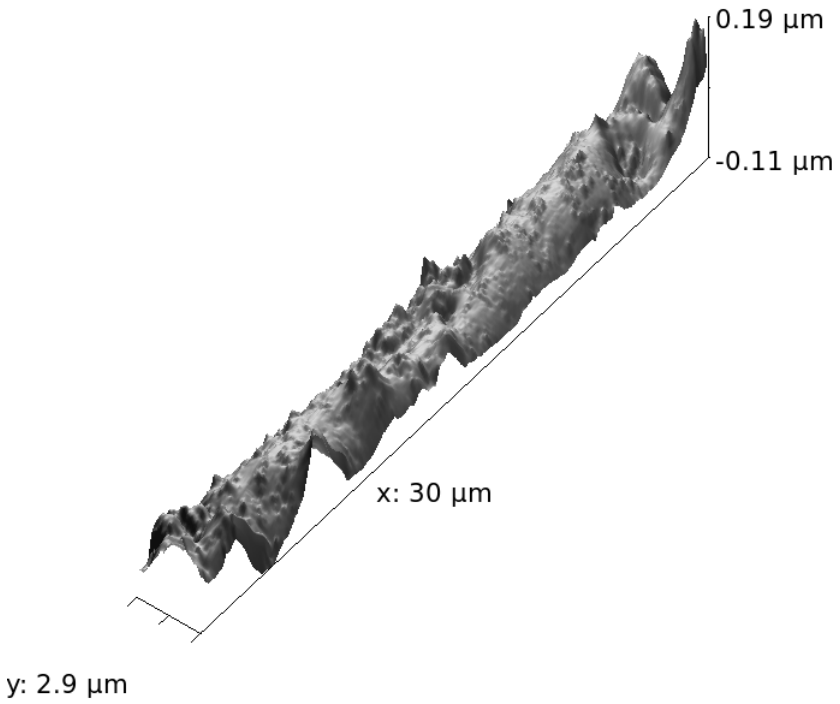

Figure 8.6: The topography of the stainless steel surface

To allow comparison of the influence of the roughness of the fibre surface on the measurements, both the glass-fibre and stainless steel fibre surfaces were imaged using the AFM in the tapping mode. The surface topography of the glass-fibre is shown in Figure 8.5 and that of the stainless steel fibre in Figure 8.6. In examining Figures 8.5 and 8.6, in particular the scale on the z-axes, it can be seen that the glass-fibre surface is significantly smoother.

Comparison between the polyester, glass-fibre and stainless steel fibres is best done using the root mean square (rms) roughness (R_q), which can be calculated using the formula,

$$R_q = \sqrt{\frac{\sum_{n=1}^{N} z_i^2}{N}}, \tag{8.5}$$

where N is the number of peaks and z_i is the peak height. Or it may be obtained directly from the AFM software.

The R_q values for fibres of each material type are given in Table 8.1. Given

Table 8.1: Surface roughnesses and R^2 values

		R^2	
Fibre Material	R_q (nm)	Oil A	Oil B
Glass-fibre	2.06	0.87	0.67
Polyester	3.17	0.77	0.82
Stainless steel	5.78	0.67	0.05

that the surface roughness of each fibre is non-uniform the R_q values given in Table 8.1 are the average value of a minimum of 5 surface measurements.

Direct comparison of the surface roughness values with the R^2 values indicates that, in general, a higher surface roughness correlates with deviation between measured and modelled values. This confirms that the surface roughness will effect the force required to move a coalesced liquid droplet.

8.3.2 Measurements on Oil Droplets Containing Particulate Matter

Measurements of the force required to move a coalesced, oleophillic droplet of sooty oil were conducted on 17 μm diameter polyester fibres. These measurements can be compared to those for clean oil and the influence (if any) of the presence of soot in the oil. The measurements for both soot concentrations are given in Figure 8.7, along with those of oil B on this fibre diameter (previously shown in Chapter 6).

The combined data set in Figure 8.7 shows that the majority of the measurements are close to the model predicted values and that there is no significant differentiation between the measurements at the different soot concentrations. It therefore appears that at these (low, realistic) soot concentrations there is no observable effect on the force required to move a coalesced liquid droplet along a fibre.

It should be noted, however that the presence of particulate matter, such as soot, would be expected to alter the physical properties of the oil. These

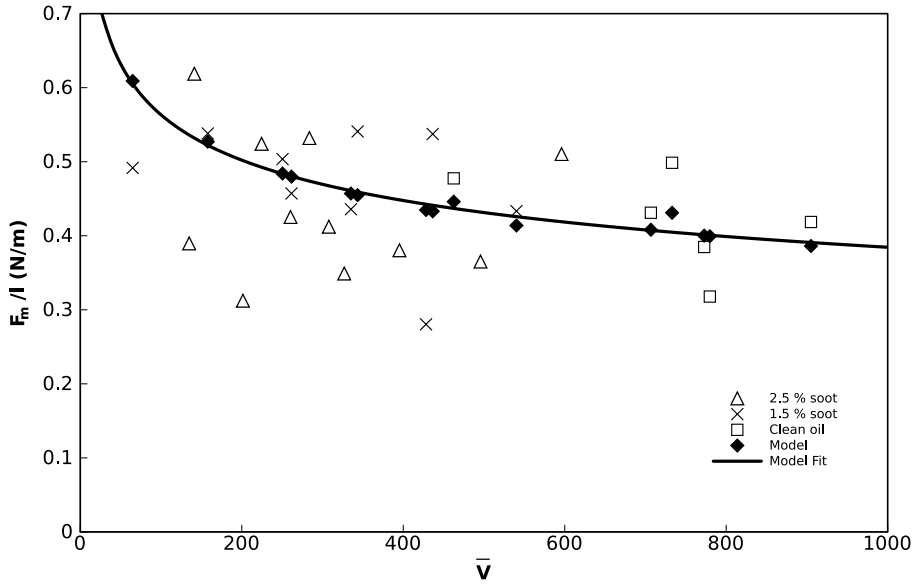

Figure 8.7: Measured and modelled static forces for different soot concentrations

Table 8.2: Properties of sooty oil

	0 % Soot	1.5 % Soot	2.5 % Soot
viscosity (μ) $Pa.s$	0.0941	0.1035	0.1086
surface tension* (γ) N/m	0.0295	0.0297	0.03

* values from Bredin et al. (2011)

effects would most likely be exhibited by changes to the oil viscosity and possibly the surface tension. This was examined and the surface tension of oil containing 2.5% soot was only 3% higher then that of the clean oil, while the difference in viscosity is around 15%. The surface tension and viscosity values are given in Table 8.2.

The surface tension is therefore not significantly affected by the presence of soot; at these concentrations. This explains the results shown in Figure 8.7, where the force required to move droplets with different soot concentrations does not vary significantly. However, experiments conducted with oil containing soot were found to have a higher pressure drop than experiments

with clean oil, meaning that the presence of soot is having an effect (Bredin et al., 2011). This effect can also be seen by comparing the viscosities of oil that contains soot and oil that does not. Therefore, the effect of soot is to increase the viscosity of the oil and hence slow down the process by which the oil drains from the filter. It is therefore expected that the force required to move the droplet from its stationary position will not be (significantly) effected by the presence of soot, but once droplet motion starts, the effect of soot on the viscosity will act to slow the drainage of the droplets.

Additionally, there is the possibility that the presence of the soot particles will have further effects on the system, such as possible adhesion of soot particles to the fibre, which may ultimately influence the force measurement. While the sooty oil appears much darker in colour than the clean oil, there was no observable difference in the areas of the fibre between the droplets, so the presence (if any) of soot sticking to the fibre when a droplet is moved could not be verified.

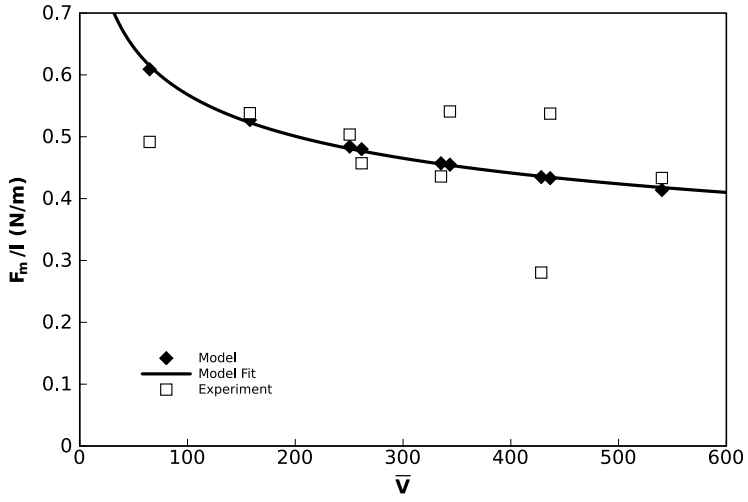

Figure 8.8: Measured and modelled static forces for coalesced droplets of oil containing 1.5 % soot

Figures 8.8 and 8.9 show that at low soot concentrations the theoretical model is still valid.

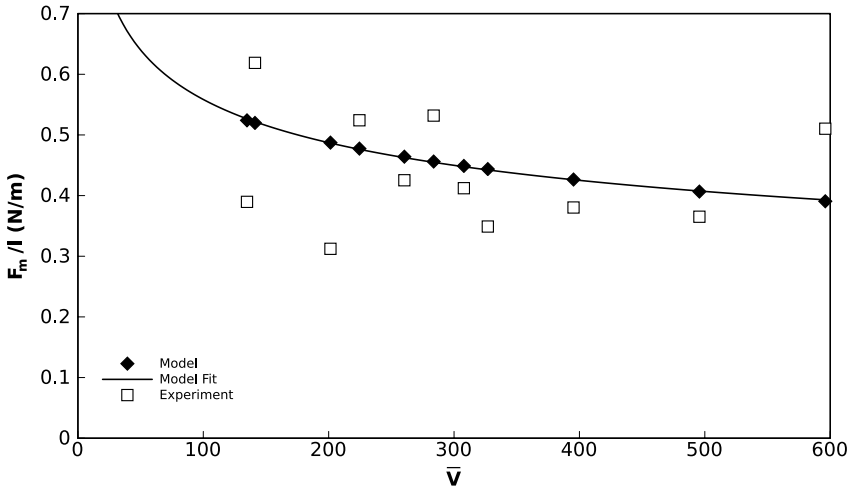

Figure 8.9: Measured and modelled static forces for coalesced droplets of oil containing 2.5 % soot

8.3.3 Coalesced Droplets on Oleophillic Fibres

In both Chapters 6 and 8, power laws have been fitted to the model predicted data to provide an empirical approximation to the theoretical model. In Chapter 6, the reduced volume has been used to allow the comparison of different fibre diameters and has also been used in this chapter to allow direct comparison between the results for different fibre materials all of which have different diameters.

To allow data for different oils to be plotted on the same graph, F_l has been divided by the surface tension (σ) of the relevant oil, thus producing a dimensionless 'force'. Figure 8.10 shows all of the measured and modelled data points for the measurements of coalesced droplets on oleophillic fibres. Also shown is a power law fitted to all the modelled data.

Examination of Figure 8.10 reveals that the model data can be described by a single power law, where;

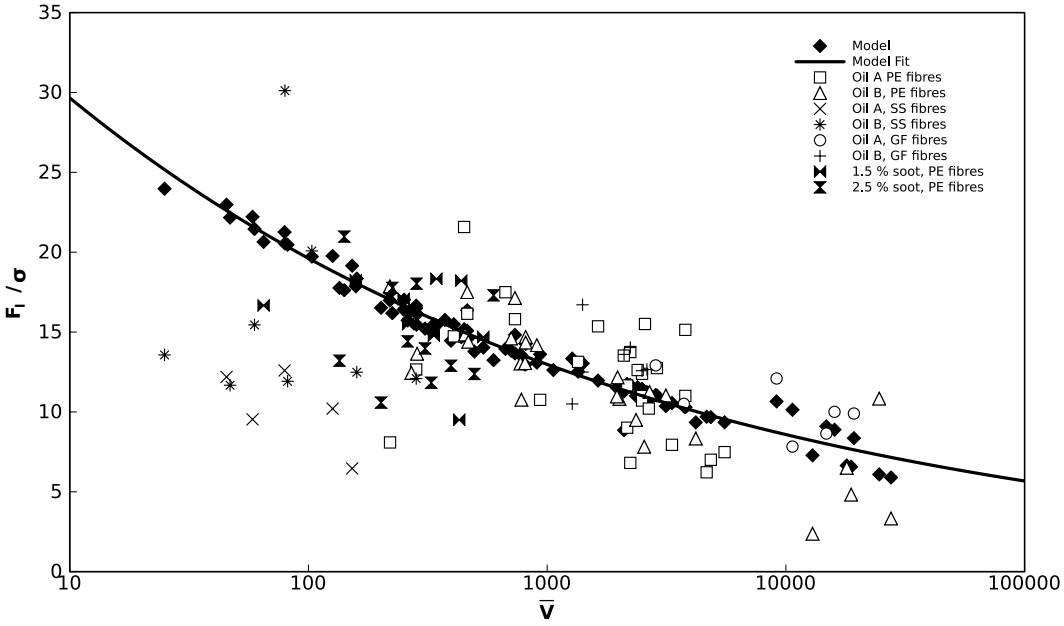

Figure 8.10: Measured and modelled static forces for coalesced droplets on oleophillic fibres

$$\frac{F_l}{\sigma} = 44.8458\,\overline{V}^{-0.1795}, \tag{8.6}$$

and has an R^2 of 0.95.

There is some variation between the modelled data and the power law fit, this is due to the different contact angles that occur on the fibre materials and over different fibre diameters.

Figure 8.10 demonstrates that all the measurements of the droplets on oleophillic fibres can be plotted on the same axes, using dimensionless terms. It also has shown that the measured data agree well with the model fit curve. Therefore, as an alternative to evaluating the model, the model-fit curve is offered as a way of determining the force required to move a coalesced liquid droplet from its stationary position on the fibre directly. The model-fit curve is shown alone in Figure 8.11.

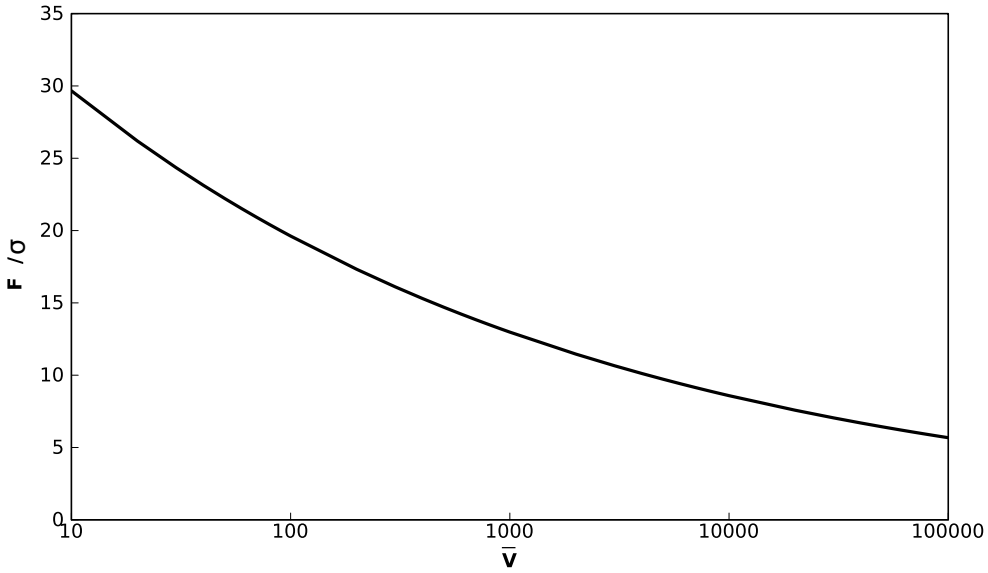

Figure 8.11: The power law fit to the modelled values for the whole data set (Equation 8.6)

8.4 Conclusion

Chapter 8 has extended the application of the theoretical model (Equation 6.19), originally presented in Chapter 6. Here the model has been applied to different fibre materials as well as coalesced droplets of sooty oil. It has been shown that the model may be applied to all of the major materials used to make filter fibres, and that it works well across a range of realistic fibre diameters.

Also presented, was a graph describing a power law fit to all the model data, thus providing an alternative to the model, as the latter must be evaluated numerically. It should be possible to determine the force required to move a coalesced droplet of a liquid that wets a fibre directly from Figure 8.11 (or Equation 8.6), provided the droplet volume is known. It should however be remembered that the surface roughness of the fibre will influence the force; so for fibres with a high degree of surface roughness the model/power law fit should be applied with caution.

9 Development and Validation of a Computational Fluid Dynamics (CFD) Model for Fibrous Filtration - incorporating micro-scale droplet-fibre dynamics

9.1 Introduction

The basic principles of computational fluid dynamics (CFD) were described in Section 2.8. In terms of fibrous filtration of liquid aerosols, CFD offers a method of modelling filter behaviour which will not suffer from the drawbacks of the macro-scale empirical models, described in Section 2.5. This is because instead of calculating parameters from empirical fits, CFD will simulate the behaviour based on the fundamental physics of fluids. This will obviously be far more computationally intensive, but if properly developed, will avoid issues associated with transition points between stages, as the filter will be simulated in operation and so these transitions will happen because of the behaviour of the (simulated) collected oil and not rely on some empirical factor.

This will however require that the CFD solver is able to realistically model particle tracking, particle capture, droplet coalescence and break up and liquid transport within the filter. Also, a means of validating the solver with regard to each of these factors will be required.

The OpenFOAM CFD package (Silicon Graphics Inc. Sunnyvale, USA) was selected for this work, as it is free, open-source and therefore easily modifiable/editable. It comes with a robust Lagrangian tracking algorithm, which is essential for this work. Additionally, the user is less restrained in the use of different packages and solvers and can couple different solvers such that work can be done without the need for it to be anticipated by the software

developers. OpenFOAM is also advantageous over commercial packages as it allows the user into the code so that, they can see exactly what is being implemented and how.

This chapter will examine:

- Particle capture in OpenFOAM
- Plateau-Rayleigh instability in OpenFOAM
- Droplet motion in OpenFOAM.

9.2 Solver Development

Thus far, by building on standard OpenFOAM solvers, the particle tracking and particle capture components of the solver have been developed (King et al., 2010). In the initial development of the solver, solid particles were considered. These particles were assumed not to interact with one another or to influence the fluid flow, though they themselves may be affected by the fluid flow. This initial version of the solver is called *dustParticleFoam* and was used for the validation of particle capture, before coupling with the volume-of-fluid solver and particle collision was implemented.

9.2.1 Particles

Each particle is individually tracked through the flow field until it is collected or exits the geometry. The particle tracking is done within a Lagrangian frame of reference, with the integration of particle position and velocity done explicitly at least once per time-step (King and Mullins, 2011). In order to accurately model the motion of particles, the forces acting on the particles had to be incorporated. The starting point for this was the standard OpenFOAM solver *icoLagrangianFoam*, which utilises a particle tracking algorithm. Equations describing the buoyancy, drag and thermal diffusive

forces had to be implemented to create the new solver *dustParticleFoam*.

The buoyancy forces, F_b, are described by,

$$F_t = \frac{\pi d_p^3}{6} (\rho_p - \rho_g) g, \tag{9.1}$$

where ρ_g in these simulations is simply the density of air and ρ_p is the density of the particle, which will be the density of the oil (i.e. the particles are really liquid droplets).

The drag forces, F_d, are described by,

$$F_d = \frac{18\mu}{\rho_p d_p^2} \frac{C_D}{24} Re, \tag{9.2}$$

where C_D is the drag coefficient, determined using the model of Haider and Levenspiel (1989) with,

$$C_D = \frac{24}{Re} \left(1 + 0.1806 Re^{0.6459}\right) + \frac{0.4251}{1 + \frac{6880.95}{Re}}. \tag{9.3}$$

For small particles (like the ones encountered in oil-mists) thermal diffusion (Brownian motion) is significant. The force then acting on the particle due to thermal diffusion, F_k is described by,

$$F_k = \mathbf{G} \left(\frac{\pi S_0}{\Delta t}\right)^{\frac{1}{2}}, \tag{9.4}$$

where $\boldsymbol{G}$ is a vector whose components are independent zero-mean, unit variance Gaussian random numbers (Ounis et al., 1990).

The components of the Brownian force for particles are white noise processes, with spectral intensities described by,

$$S_{ni,j} = S_0 \delta_{i,j}, \tag{9.5}$$

(Ounis et al., 1990). With, S_0, defined as,

$$S_0 = 216 \frac{\nu k_B T}{\pi^2 \rho_g d_p^5 \left(\frac{\rho_p}{\rho_g}\right)^2 C_C}, \tag{9.6}$$

where ν is the kinematic viscosity, k_B is the Boltzmann constant and T is the reference temperature (set as 293.15K). Here the value of the Cunningham correction factor, C_C is,

$$C_C = 1 + \frac{2\lambda}{d_p}\left(1.257 + 0.4exp\left(-0.55\left(\frac{d_p}{\lambda}\right)\right)\right), \tag{9.7}$$

with the mean free path, λ, determined using,

$$\lambda = 0.385\left(\frac{\rho_p d_p k_B T}{\mu^2 \pi^2}\right)^{\frac{1}{2}}. \tag{9.8}$$

Note that the expression given here for the Cunningham correction factor is different to that given in Chapter 2 as for the purposes of determining the Brownian force, it is solely small particles that are of interest. Hence the use of Equation 9.7 which is specifically for micron-scale particles.

9.2.2 Particle Tracking

One of the reasons for selecting the OpenFOAM CFD package was that it contains a robust particle tracking algorithm. This is the algorithm of Macpherson et al. (2009), discussed in Section 2.8.3. The algorithm itself is presented and discussed in detail by Macpherson et al. (2009) in their work, but will be mentioned here to aid in the description of the solver. For every particle then, the following steps are evaluated;

1. The fluid and flow properties are evaluated for the current cell location

by interpolation.

2. The forces acting on the particle are evaluated.

3. The trajectory of the particle is determined, based on the amount of time left in the current time step.

4. The intersection of the particle's trajectory with a cell face is determined.

   (a) If the calculated trajectory intersects a boundary face, a flag is set (which indicates which boundary has been intersected, and will allow the 'fate' of the particle to be accounted for) and no further movement of the particle is considered.

   (b) If the calculated trajectory intersect an internal face, then the particle will be transferred to the neighbouring cell, the portion of the trajectory completed (the distance from the particle's original position to the new cell) is subtracted from the remaining time, and the process is restarted from step 1.

   (c) If the calculated trajectory does not intersect a face, the particle's position is updated and the next particle is tracked, beginning at step 1.

The geometries used in this work contain a cyclic boundary, therefore in the case of the calculated trajectory intersecting a face on a cyclic boundary, there will be a modification of step 4a. These faces will be treated like internal faces and the particle will be transferred to the corresponding cell on the opposite boundary (e.g. if a particle's trajectory intersects a face on the left hand boundary, it will be moved to a cell in the corresponding position on the right hand boundary).

9.2.3 Fluids

The volume-of-fluid (VOF) method (described in Section 2.8.3) is utilised for the simulation of liquid in the solver. In OpenFOAM the VOF method is

incorporated into the standard solver, *interFoam*. The solver that is being developed is result of the coupling of *dustParticleFoam* with *interFoam*. This solver is known as *twoPhaseOilParticleFoam* and is used for the simulation of droplet fibre systems.

In addition to the momentum and continuity equations (see Equations 2.80, 2.81, 2.82 and 2.2) the VOF method involves a transport equation for the volume fraction of on phase (the oil in the case of coalescing filters), which includes interface compression;

$$\frac{\delta\alpha}{\delta t} + \bigtriangledown \bullet (\mathbf{U}\alpha_l) + \bigtriangledown \bullet [U_r\alpha_l (1 - \alpha_l)] = S_\alpha, \tag{9.9}$$

with U_r being the compression velocity, α_l the fluid volume fraction and S_α a phase fraction source term. Note that the compression velocity corresponds to the difference between the liquid and gas velocities and is not related to compressible flows (Berberovic et al., 2009).

The solver *twoPhaseOilParticleFoam* has been developed as a three-dimensional unsteady solver that utilises the Multidimensional Universal Limiter with Explicit Solution (MULES) algorithm for the transport equation (Equation 9.9) and the Pressure Implicit with Splitting of Operators (PISO) algorithm (described in Section 2.8.3) to solve for the coupled pressure-velocity fields (King and Mullins, 2011).

9.2.4 Particle Collision

In *twoPhaseOilParticleFoam* particle collisions are calculated once during each particle time step. As previously mentioned, *dustParticleFoam* does not consider the interactions of particles with one another. A simple algorithm is implemented to check for collision between particles. For each cell, a list of particles and their positions is generated. The positions of all the particles in the cell (and those in the neighbouring cells) are then compared and any particles that are closer than the sum of their individual radii are

considered to have collided. Remembering that the particles here are liquid droplets, the angle of collision is not required as all collided particles will merge and particles deflecting of one another do not need to be considered.

Particles that collide are deleted from the simulation or marked as deleted (so that they will not be considered further in the simulation, but will be recorded for the purposes of post-processing) and replaced by a new particle with a diameter determined from the combined mass of the colliding particles. The position and momentum of these new particles are determined by taking the mass weighted average of the position and momentum of the original particles (King and Mullins, 2011).

The particle collision algorithm is implemented after the particles have been moved by the particle tracking algorithm. The new particles (resulting form collisions) are then generated and considered by the particle tracking algorithm, beginning at step 1.

9.2.5 Particle Collection

In *dustParticleFoam* and therefore in *twoPhaseOilParticleFoam* a particle is collected if its' trajectory passes within one particle radius of a boundary or intersects the boundary. Given the use of cyclic boundaries (see Section 9.3), the only areas that particles may be collected is at the outlet or on the fibres. This is the extent to which *dustParticleFoam* operates, thus making it an ideal means of validating particle capture (see Section 9.4). In order to simulate filter behaviour the collection of particles, by other particles and already collected oil must be considered.

The collection of a particle by another particle is simply a collision and is handled by the solver *twoPhaseOilParticleFoam* as described in Section 9.2.4. This solver also handles the collection of particles by oil, (which has been previously collected on the fibres), by considering the volume fraction of the cell. If the fluid volume fraction, α_l, in a cell is greater than 0.5, then any

particle in that cell is considered collected by the oil. Where the value of 0.5 was chosen as a basis upon which to identify cells containing the liquid-gas (oil-air) interface.

Any particle collected by the oil is marked as deleted (and therefore no longer considered in the simulation). To preserve continuity, the mass of the collected particle must be incorporated into the transport equation (Equation 9.9). This is achieved by adjusting the volume fraction of the cell to include the volume of the collected droplet. As the particle is an oil droplet, which is collected by the same oil which is already in the cell, the densities are obviously the same and therefore by conserving volume the mass is being conserved also. The adjusted volume fraction of the cell is then,

$$\alpha_l = \frac{\pi d_p^3}{6} \frac{1}{V_{cell}}, \tag{9.10}$$

where V_{cell} is the volume of the cell (King and Mullins, 2011).

Additionally, the momentum must also be conserved so a source term is added to momentum equation, to account for the momentum of the collected (deleted) particle. The momentum source term is then,

$$S_m = \rho_p u_p, \tag{9.11}$$

where u_p is the velocity of the particle, when it was collected.

9.2.6 Conversion from Particles to a Volume of Fluid

In order for the behaviour of a coalescing filter to be simulated, the solver must be able to transition form the tracking of individual particles to a volume of fluid treatment without relying on a fluid volume already in place. This will always be case when a clean filter is considered at the start of a simulation. The transition from Lagrangian tracking of individual particles

to a VOF method is achieved in *twoPhaseOilParticleFoam* by considering the ratio of particle volume to cell volume. If the value of the ratio reaches a value of 1 (i.e. the cell is full of fluid) then the particles are deleted and the adjusted volume fraction and momentum source term are calculated as described in Section 9.2.5 and added to the transport and momentum equations respectively.

This ability for the solver to transition from particle tracking to VOF allows the coalescence of collected particles to be simulated.

9.3 Geometry and Mesh Preparation

The geometries and meshes used in this work were prepared using the standard OpenFOAM tools. All meshes were initially constructed using a *blockMeshDict* dictionary file to define a basic geometry (often a cube) and to divide the geometry into cells and define the inlet and outlet. The fibres and fibre arrangements were prepared using Blender (a graphics rendering tool available from www.blender.org) to prepare stereo-lithography (stl) files, which were then imported and meshed within the geometry using the *snappyHexMesh* utility.

Initial simulation and validation work was carried out on simple geometries; either a single fibre or 4 fibres in a grid pattern, situated in a cube or square prism. Figure 9.1 shows an example of a grid pattern mesh used in the simulation and validation of the solver *dustParticleFoam*, the fibre diameters are 10 μm and the geometry is a 100 x 100 x 100 μm cube.

Given that the geometries contain curved surfaces (i.e fibres) the mesh needed to be examined for skewed cells (which may cause the simulations to become unstable, and affect convergence). Of particular interest will be the areas of the grid pattern geometry where the fibres cross over one another. This may be checked visually (see Figure 9.2), of by use of the *checkMesh* commands in OpenFOAM.

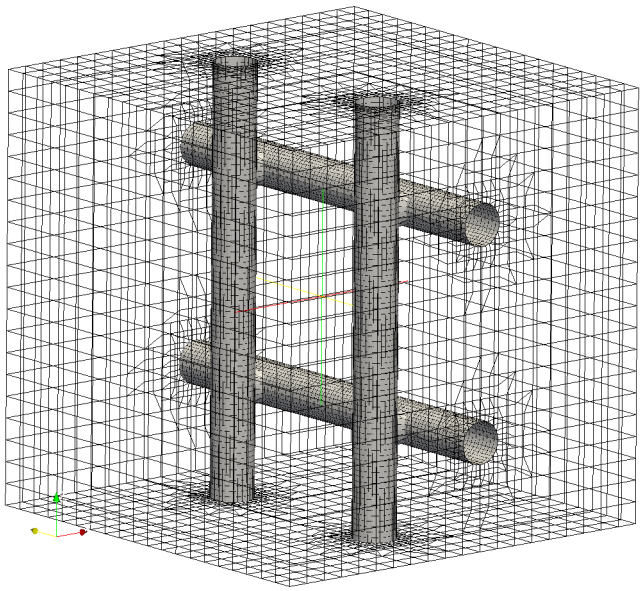

Figure 9.1: An example of a mesh containing 4 fibres arranged in a grid pattern, as used in the simulation/validation of particle capture

As can be seen in Figure 9.2 there is a small area where the overlapping fibres are meshed together. This 'bridge' in the mesh could have been reduced by additional mesh refinement steps. However the mesh cells that would have existed would have become more and more skewed as a result of continued refinement. This would have resulted in a large number of very small, highly skewed cells, which would have affected the stability of the simulation. Given that these areas were smaller in diameter than the fibres, the flow and particle motion simulations were not significantly affected. Additionally, any potential increase in accuracy would have been offset by the reduced stability of the calculation.

All meshes were set up with a defined inlet and outlet, such that flow is in the direction parallel to the x-axis. Additionally, the remaining walls were set up with cyclic boundaries, with the top and bottom walls paired and the

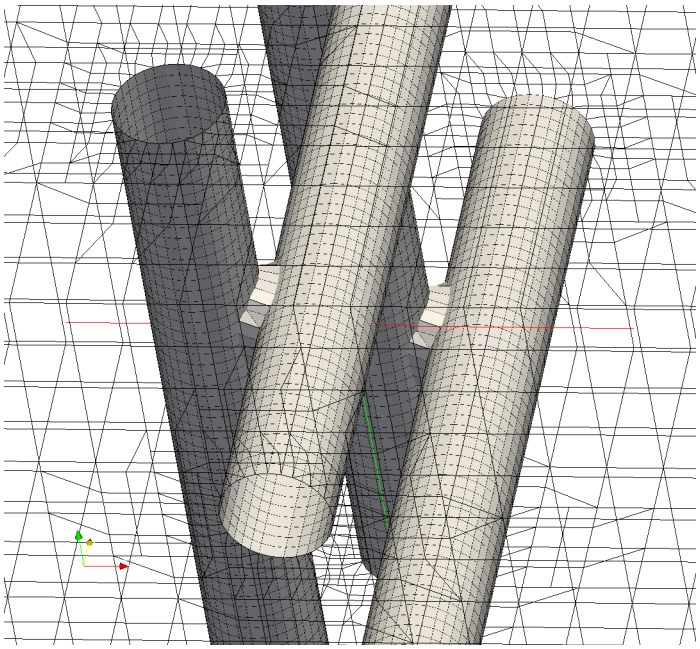

Figure 9.2: A close-up view of the mesh shown in Figure 9.1 showing the mesh where fibres cross over

left and right walls paired. This allowed the number of particles to be preserved so that all particles entering the geometry, would either leave via the outlet or be captured by the fibres. With these cyclic templates any particle that 'hit' the top, bottom, left or right wall would exit and then re-enter the geometry from the opposite wall. This also represents a more physically realistic system as the geometry size is much less than that of an actual filter. Therefore if we consider a small section of a filter, it is likely that there will be particles entering from adjacent sections and exiting to adjacent sections. This also has the potential to reduce simulation times, as only a small section and not the whole filter needs to be simulated. When realistic filter geometries were simulated however, the simulation had to utilise a geometry with the same thickness (depth) as the real filter.

9.4 Examination of Particle Capture

The capture of particles using the solver *dustParticleFoam* was examined by comparing the results of simulations with the efficiencies predicted using the single fibre efficiency theory. To achieve this a geometry has to be prepared, for which the single fibre efficiency is known to be accurate. For this purpose a regular mesh geometry will be used consisting of four fibres forming a grid pattern (see Figure 9.1). Equally important is the selection of the appropriate single fibre efficiency equations, which have been discussed in Section 2.5.3.

9.4.1 Approach

The solver *dustParticleFoam* was tested over a range of droplet diameters and the capture efficiency compared to that predicted by the SFE theory for a filter of the same parameters as that simulated. For the filter systems examined in this work the significant capture mechanisms are those of diffusion, interception and impaction. Given the choice of the grid pattern geometry (see Figure 9.1) the most appropriate SFE equation for capture by diffusion is Equation 2.38, with the coefficient, A, used as 2.7, which as mentioned in Section 2.5.3 is the value used for a regular screen or mesh.

For particle capture via impaction Equation 2.32 was used, as this expression has been used by a number of authors since 1969 and has remained consistent. Additionally the value of N_R is less than 0.4 for all cases and so there is no ambiguity about whether or not the expression is appropriate or reliable. For particle capture by interception, the simplified equation of Lee and Liu (1982) (Equation 2.29) was used. The simplified expression was chosen as the value of N_R is small and the values given by Equation 2.29 do not differ significantly form the values given by 2.28.

An additional term for the combined effects of diffusion and interception was included in the form of Equation 2.52, as for all particles larger than 200 nm in diameter it was found to give a value of the same order of magnitude as that of the other capture mechanisms and therefore is significant. The total

single fibre efficiency was then calculated using Equation 2.53 and omitting the gravity term. The total efficiency was then found using Equation 2.59; with the thickness of the filter set as the depth of the geometry (100 μm) and the packing density determined by diving the volume of the fibres by the volume of the cube ($\alpha = 0.0314$).

The simulations were run with a single injection of particles at the commencement of the simulation and were allowed to run for 0.003 s, which was the time required to allow all of the particles to be either be collected or exit the geometry. The simulations were run with an injection of 10000 particles and an injection area of similar size to the inlet face, located a small distance within the geometry from the this face.

9.4.2 Results and Discussion

An example of the simulation of the motion and capture of particles is shown in Figure 9.3. Figure 9.3a shows the geometry at t = 0 (i.e. before the injection of particles), Figure 9.3b shows the simulation after 0.00002 s, where the particles have been injected. Figure 9.3c shows the particles as they move within the flow filed, which has begun to be distorted by the presence of the fibres after 0.0002 s. Figure 9.3d shows the simulation after 0.00032 s, when about half the particles have passed the fibres. Figure 9.3e shows the simulation after 0.00074 s, when the particles have passed the fibres and Figure 9.3f shows the simulation after 0.0026 s, when all the particles have exited the geometry or have been captured.

Initial simulations conducted showed that particle capture was dependent on the size of the mesh used. This effect was explored by altering the size of the mesh in the *blockMeshDict* file. A series of meshes were prepared, all using the grid pattern geometry, with cell sizes ranging from 5 μm to 1.667 μm. Simulations were then run on each mesh using particle diameters of 50 to

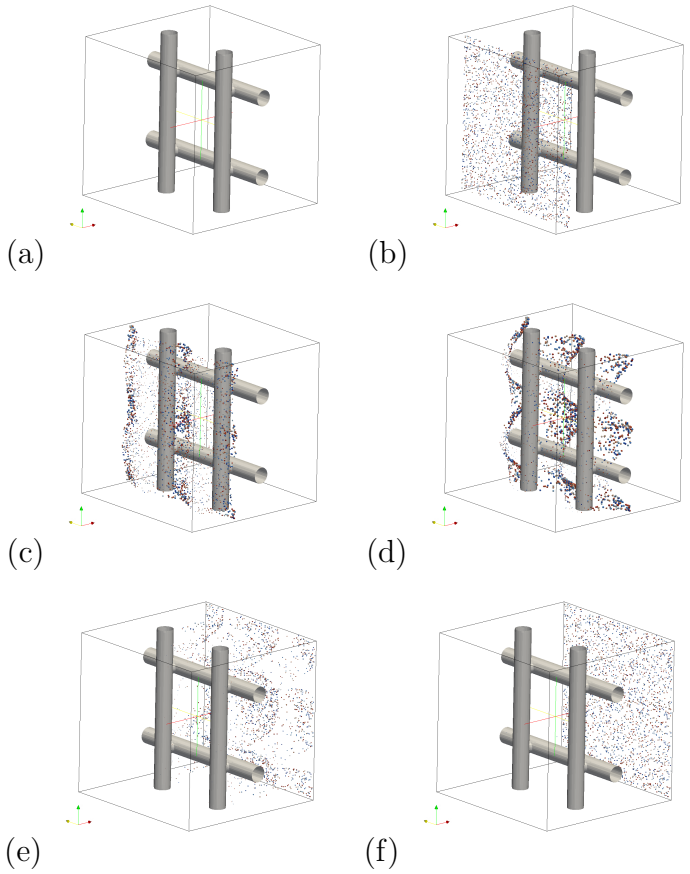

Figure 9.3: A series of images showing the movement of particles through the geometry (the number of particles has been reduced to aid visibility)

1000 nm. The simulated capture efficiencies (simply the number of particles that are collected by the fibres divided by the total number injected) are shown in Figure 9.4, with the SFE theory predicted efficiencies.

As shown in Figure 9.4, the coarser meshes tend to over predict capture efficiency for all particle diameters, but form the same shaped curve as the SFE theory predicted values. Essentially the simulated results appear as though they could be described by a translation of the SFE theory predicted curve. As the mesh used becomes finer the values for the small particles (where diffusion is the main capture mechanism in place) approach the predicted

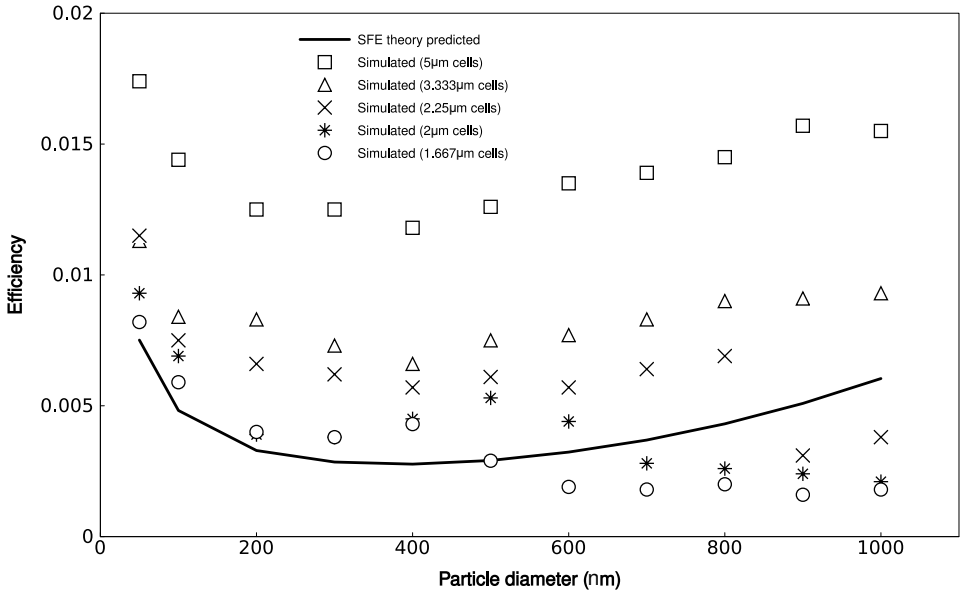

Figure 9.4: Simulated η_T values using different mesh sizes, compared to SFE theory predicted efficiencies

values. For particles less than 500 nm in diameter the agreement between the simulated and predicted values is very good for the finest mesh. However, the simulated capture efficiencies for the larger particles (where interception is dominant) are less than the predicted efficiencies when finer meshes are used. A few simulations were run on even finer meshes, which resulted in a greater deviation from the SFE predicted efficiencies. Additionally, as the mesh used become finer the calculation time increases significantly. It is then perhaps better in to use the coarser mesh, as the results will better over the whole range of particle diameters and the computational efficiency will be relatively high.

The mesh dependency has an additional effect on the larger particles. Whereas for particles of diameters smaller than 600 nm the simulated efficiency approaches the SFE predicted efficiency, the simulated efficiencies for larger particles do not and the shape of the curve deviates from the shape of the typical capture efficiency curve. This is due to an issue with the way the

particles are treated. Particles are tracked as a point mass, located at the centre of the particle; therefore the centre of the particle may be located in one cell, but part of the outer surface of the particle could be in a neighbouring cell. As the cell size is reduced (which is the obvious result of using a finer mesh) the size of the larger particles become closer to the size of the cell. Hence it becomes increasingly likely that a particle may be located in two or three (potentially more) different cells. This is not an issue for the tracking algorithm, but it can make it difficult for the solver to determine that a particle has been (should be) captured.

The reason for the deviation in the shape of the efficiency curve is then due to a particle passing a fibre, close enough to be captured (i.e. within 1 particle radius) where the solver does not recognise the particle as being captured as the centre of the particle is in a cell which is not immediately adjacent to the fibre. This problem may be avoided by using a coarser mesh, which has cell sizes that are larger than the largest particle being simulated. This would allow the efficiency plot to maintain the correct shape though would mean that capture efficiency was over-predicted by a factor of approximately 2.3. Alternatively if particles smaller than 600 nm in diameter are used then use of a finer mesh will give simulated efficiencies that agree well with the SFE theory predicted efficiencies.

There is also a time-step dependency in the simulation of Brownian motion. This is evident from examination of Equation 9.4, which includes the time-step in the denominator of the power term. Equation 9.4 is essentially a random walk equation, where the step size is the size of the time-step being used in the simulation. Figure 9.5 shows two potential paths of a particle; the large time-step illustrates the trajectory resulting from a single time-step, the smaller time-step shows the same distance being traversed, but in a series of smaller time-steps. Considering the two paths it becomes evident that a smaller time-step will result in a desultory route, as opposed to the simple route resulting from the large time-step. Therefore in the presence of a nearby fibre, a smaller time-step would, by the nature of its effect on the

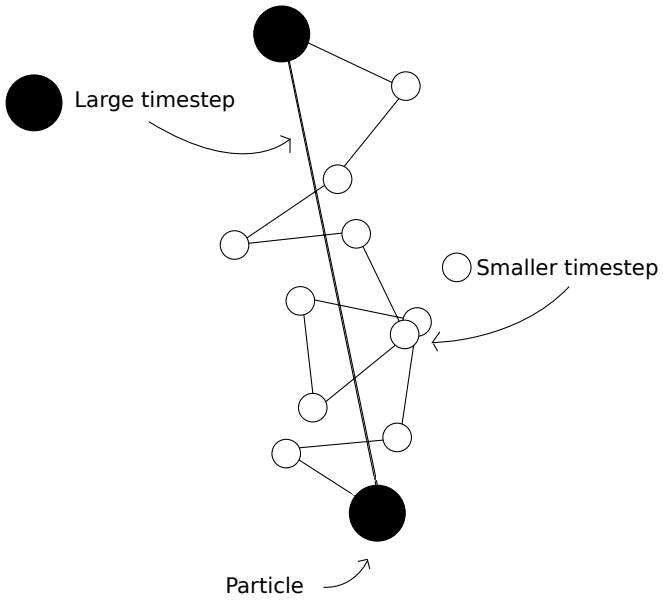

Figure 9.5: Possible particle trajectories, due to Brownian motion, at different time-step sizes

particle trajectory, increase the probability of the particle passing with on particle radius of the the fibre and being collected.
The effect of this time-step dependency are illustrated in Figure 9.6, where the capture efficiencies of small particles are simulated using two different mesh sizes. It is clear that the finest mesh, provides accurate simulation of the capture of particles between 50 and 100 nm in diameter. Which given the results shown in Figure 9.4 is expected. However for smaller particles there is an obvious over-prediction of capture efficiencies, shown in the simultaneous on both mesh sizes. This is where the timestep issues manifest. In order to maintain stability in the simulations of particle sizes less than 50 nm, the size of the timestep must be reduced. This reduction in time-step size leads to an increase in the predicted capture efficiency.

As demonstrated, for particles between 50 and 500 nm, a finer mesh allows accurate prediction of capture efficiency, outside this range however, there is an overprediction of the capture of smaller particles and an underprediction of the capture of larger particles. In terms of a mass-based efficiency or mash loading of the filter, the over prediction of the capture of small particles is

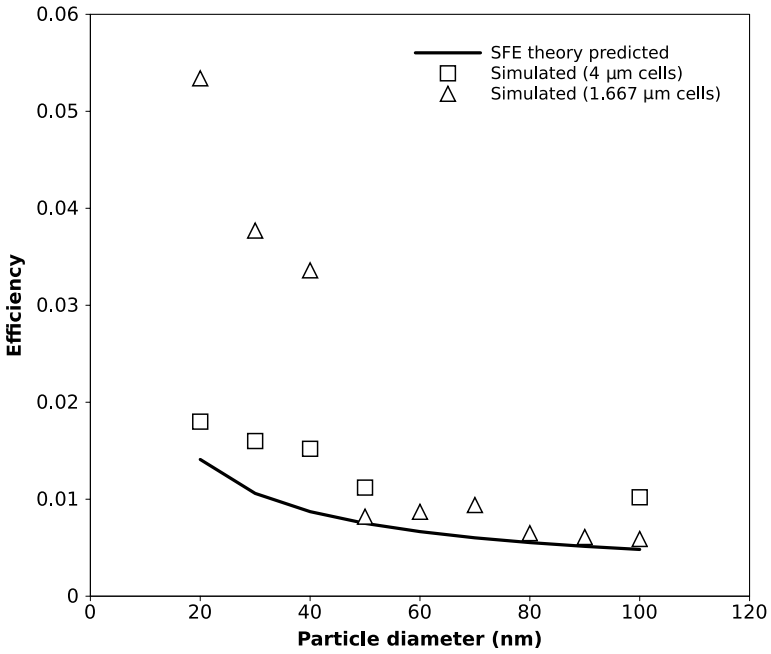

Figure 9.6: Simulated efficiency η_T of small particle collection, compared to SFE theory predicted efficiencies

perhaps insignificant considering the mass of a small (say 10 nm) particle in relation to a larger (e.g. 500 nm) particle. The main issue facing the simulation is the capture of the larger particles (which will be significant in terms of mass loading), though this issue could potentially be resolved via use of an algorithm which searches the cells surrounding a particle.

9.5 Examination of Plateau-Rayleigh Instability

The development of the solver *dustParticleFoam* has dealt with the Lagrangian tracking of particles, and has been validated using the Single Fibre Efficiency theory. Additionally this solver has successfully been coupled with a Volume of Fluid (VOF) solver in *twoPhaseOilParticleFoam*. So in this state the solver is able to handle the tracking of discrete particles and the collection of these particles by surfaces as well as volumes of fluid (i.e. large droplets). However, in order to model the behaviour of a coalescing filter, the solver needs to accurately model the collection of discrete particles (oil droplets) by

fibres, the spreading of these droplets over the fibre surface, film formation and the subsequent break up of the film by Plateau-Rayleigh instability.

Given that Plateau-Rayleigh instability is the mechanism responsible for the presence of coalesced droplets in oleophillic filter media, the ability to model it accurately is important in any attempt to model filter behaviour. The ability of OpenFOAM to simulate handle this can be examined by simulating the behaviour of a liquid film on a cylinder in the absence of a flow field. Section 2.4 has shown that there is a maximum allowable film thickness that can be reached before the film breaks up, thus it should be possible to validate/calibrate the way Plateau-Rayleigh instability is implemented in OpenFOAM.

9.5.1 Approach

A mesh was generated in the manner described in Section 9.3 over a single 10 μm diameter fibre (cylinder) located centrally and oriented vertically within a 100 μm x 100 μm x 100 μm cube. A fluid column was placed around the fibre by using a field setting utility, implemented via the command line or through the use of a dictionary file. An example of a *funkySetFieldsDict* file is given in Appendix A, this would give a film around the fibre, with a thickness of 5 μm. The flow field of this film would be (0,0,0); i.e it is stationary.

This 5 μm film would be a very thick film by coalescing filter standards and in reality would never be able to form. It is useful however as it is known that it will be unstable and break up. Simulation of this system in OpenFOAM does lead to film break up. After 0.0007 seconds the liquid column was no longer present and instead there was a large centrally located droplet. Also droplet feet could be seen above and below the droplet. However the droplet was not axisymmetric as would be the case in reality and so some manipulation was required.

The transport models implemented in OpenFOAM allow for the contact angles for the two-phase interface to be defined. Using the *dynamicAlphaContactAngle* model the behaviour of *alpha1* at the fibre boundary may be set. An example of this is shown in Appendix B, where the values of the parameters *theta0*, *uTheta*, *thetaA* and *thetaR* must be defined. The value of *theta0*, the static contact angle, was selected based on the properties of the oil being simulated and using literature values or the values measured in Chapter 6. The values of *thetaA* and *thetaR* (the limiting advancing and receding contact angles, respectively) were set to 1.047 and 0.01 radians. These values are not the dynamic contact angle of the system, but limiting ranges for the simulation and were chosen to give the system a wide permissible range and also to avoid negative numbers and zeros, which may cause the calculation to encounter an error.

In order to test the modelling of the Plateau-Rayleigh instability the thickness of the film was varied each simulation to see if the break up of the film would occur. The maximum possible film thickness for a given system can be determined using Equation 2.18. Therefore by simulating film thicknesses either side of this maximum value the effectiveness of OpenFOAM in simulating the Plateau-Rayleigh instability can be determined.

9.5.2 Results and Discussion

Initial simulations of liquid film break-up in the cube geometry, illustrated the break-up of the film, however the droplets appears to grow unrealistically large on the upper and lower boundaries of the geometry. This is possibly the result of the cyclic boundary conditions influencing the simulation. Also this geometry only allowed a fibre length of 100 μm, which is perhaps too short to properly allow the Plateau-Rayleigh instability to develop. To assess and remove any such effects a number of square prism shaped geometries were used, allowing fibre lengths of 175, 225 and 500 μm to be simulated. At these fibre lengths the break-up of the liquid film was examined both with and without the cyclic boundary conditions. At these longer fibre lengths,

Table 9.1: Film thicknesses and observed break-up, without flow field

h_t (μm)	Break-up	Notes
1	no	unstable*
1.1	no	unstable*
1.2	no	unstable*
1.3	no	unstable*
1.4	yes	stable (2)*
1.5	yes	stable (2)*
1.6	yes	stable (2)*
1.7	yes	stable (2)*
1.8	yes	stable (2)*
1.9	yes	stable (2)*
2	yes	stable (2)*
3	yes	stable (2)*
5	yes	stable (2)*

unstable* - the film does not break up into droplets
stable(2)* - the film breaks up into 2 axisymmetric droplets

the cyclic boundaries appeared to have no effect on the film break-up, and so were maintained.

According to Equation 2.18, the thickest film that should exist on a 10 micron diameter fibre is 2.07 μm. Therefore film thicknesses around this value were examined. The results of the simulations run, without the presence of a flow field, are given in Table 9.1. These simulations proved to be quite unstable, which often resulted in them falling over due to floating point exceptions (i.e. the calculations began to oscillate until the point where an illegal mathematical operation was attempted). The simulations therefore had to be carefully controlled this was achieved by the use of an adjustable time-step size and setting the maximum Courant number to 0.2. Also under-relaxation was utilised by placing relaxation factors of 0.8 and 0.3 on the initial estimates of p and U respectively.

The results in Table 9.1 show that the simulated break-up occurs at a lower value of h_t than predicted by Equation 2.18. This however is permissible,

Table 9.2: Film thicknesses and observed break-up, with flow field (u_0= 0.1 m/s)

h_t (μm)	Break-up	Notes
1	no	unstable*
1.1	no	unstable*
1.2	no	unstable*
1.3	no	unstable*
1.4	yes	stable (2)*
1.5	yes	stable (2)*
1.6	yes	stable (2)*
1.7	yes	stable (2)*
1.8	yes	stable (2)*
1.9	yes	stable (2)*
2	yes	stable (2)*
2.1	yes	stable (2)*

unstable* - the film does not break up into droplets
stable(2)* - the film breaks up into 2 axisymmetric droplets

as the value obtained from Equation 2.18 represents a maximum allowable film thickness. Therefore it is clear that the solver will not allow a physically unrealisable film to exist on the fibre.

Given that the simulations of filters will involve flow, the break up of liquid columns was also simulated in the presence of a flow field, with an inlet velocity of 0.1 m/s. These results are summarised in Table 9.2.

The results in Table 9.2 show the simulated break up of the liquid film in the presence of flow. Comparison with Table 9.1 reveals that the maximum film thickness that the solver will allow is ultimately no different in the presence of a flow field; however the break-up of the film does occur earlier in the simulation, in the presence of flow. Additionally, the droplet positioning on the fibre is different in the presence of flow.

Figure 9.7 shows the break-up of a 2 μm thick film on a 10 μm diameter fibre. Figure 9.7a shows the initial film (i.e. at t = 0 s), which simply

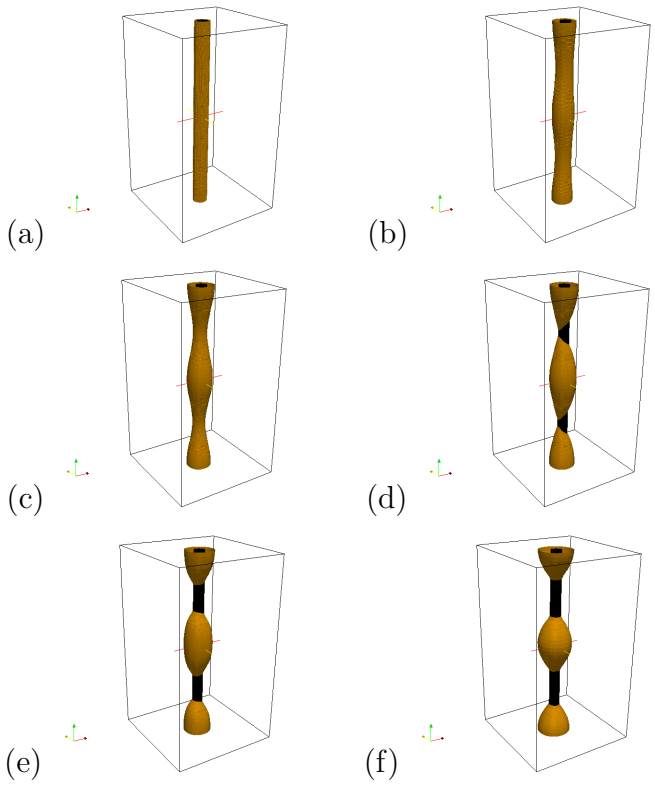

Figure 9.7: A series of images showing the simulation of the break-up of a liquid film under the influence of Plateau-Rayleigh instability and a flow field

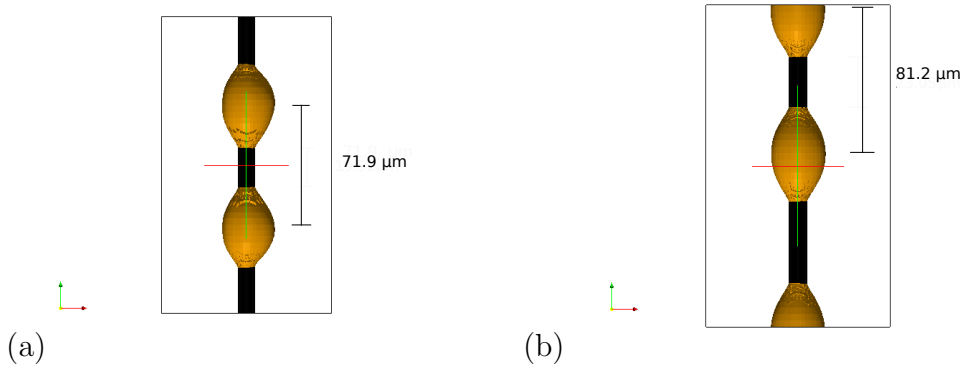

Figure 9.8: The space between droplets formed by the simulation of the break up of a 2 μm film via the Plateau-Rayleigh instability, in absence of flow, (a), and in the presence of flow, (b)

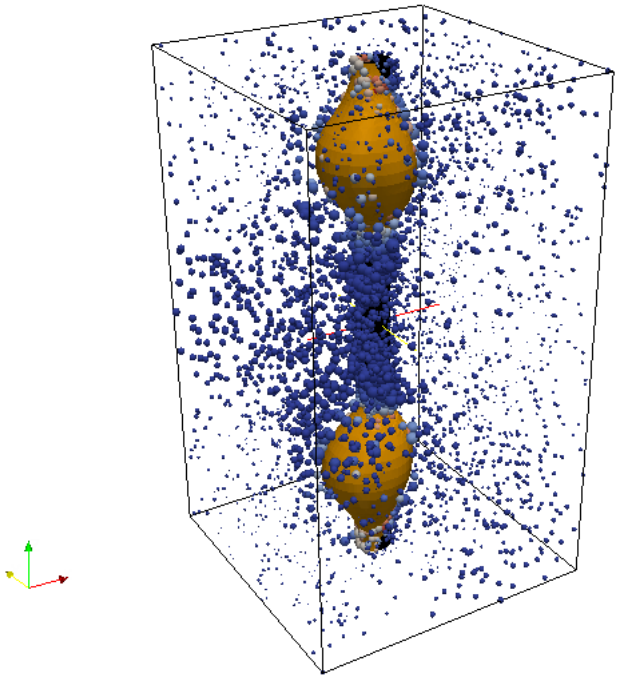

Figure 9.9: Simulation of the break-up of a liquid film after 0.00046 s; in the presence of flow, with particles (the size of the particles has been exaggerated to aid visibility)

displays the liquid film placed on the fibre using the *funkySetFields* utility. Figure 9.7b shows the film at $t = 0.00078$ s, which has begun to undulate and no longer appears completely cylindrical. Figures 9.7c, d and e show the fairly rapid formation of axisymmetric droplets at $t = 0.000845$, 0.00086 and 0.00087 s, respectively. Figure 9.7f shows a distinct centrally located axisymmetric droplet at $t = 0.00092$ s, with droplets immediately above and below extending out of the geometry.

The simulation of the break-up of a liquid film into an array of droplets via the Plateau-Rayleigh instability can be further validated using the observation of Quere (1999), where the droplet spacing was found to (usually) correspond to the length of the predominating wavelength. This wavelength as determined by Quere (1999), is $2\pi\sqrt{2}r$, and therefore on a 10 μm diameter fibre the average droplet spacing will be 44.43 μm. This however, relies on

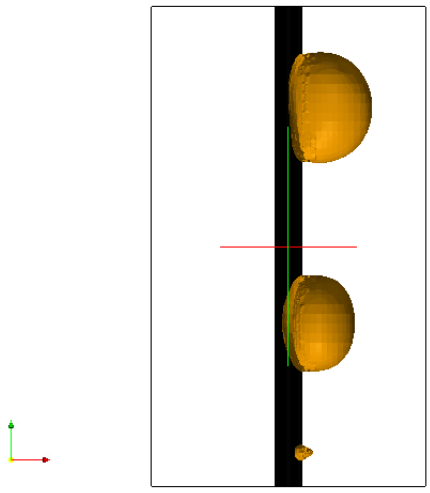

Figure 9.10: Simulation showing the 'clamshell' shaped droplets which result when the fibre boundary conditions are changed

$h_t << r_f$, which is incorrect in our case since we have a 2 μm film on a 5 μm radius fibre. As is shown in 9.8 we can measure droplet spacing from our results. Here the droplet spacing can be seen to be greater in the presence of flow, which is likely related to the earlier film break up. Mean droplet spacing for our system was found to be 71.9 $\pm$ 5 μm for u=0 and 81.2 $\pm$ 5 μm for u=0.1, with no significant difference observed for higher values of u.

The droplet spacing was found to be consistent, regardless of fibre length and is not influenced by the presence (or absence) of cyclic boundary conditions. However, given the difference between the simulated and theoretical droplet spacing on this fibre diameter, it was decided to explore the simulated droplet spacing further. 9.11 shows the simulated (VOF) and theoretical (Quere (1999) theory) droplet spacing resulting from the break-up of a film of thickness h_t on a number of fibre diameters. It can be seen that good agreement between theory and simulation exists between 15 and 20 μm and near 30 μm. Some deviation occurs above and below these values. This indicates that the break-up of a liquid film into a droplet array can be simulated

reasonably well.

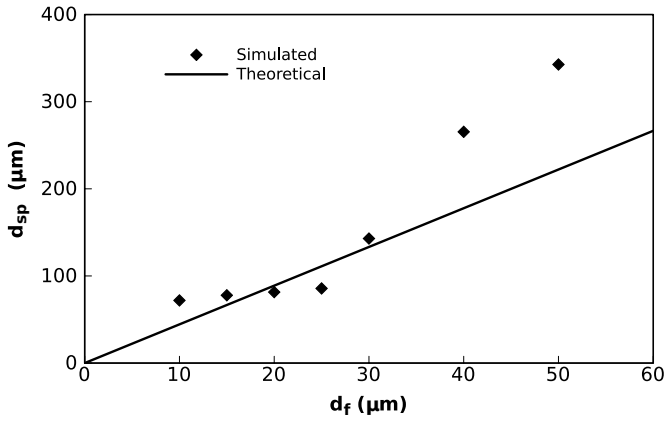

Figure 9.11: Simulated and theoretical (Quere, 1999) droplet spacing, resulting from the break-up of a liquid film of thickness h_t on different fibre diameters

To completely demonstrate the implementation of Plateau-Rayleigh instability a film that is just below the maximum thickness, as determined in Table 9.2 was examined while collecting particles to see if the film will grow in thickness and subsequently break-up due to the collection of particles. The same simulation was also run starting with a clean fibre and allowing it to collect droplets until the formation of axisymmetric coalesced droplets occurred. Figure 9.9 shows the simulation of the system starting with a film just below the maximum thickness after = 0.00046 s; where the film has broken up and the droplets may be seen.

This section has involved axisymmetric droplets, as these are the droplets that result from the break-up of liquid films. It should be mentioned, however, that 'clamshell' shaped droplets can also be simulated by altering the boundary conditions on the fibre. These 'clamshell' shaped droplets can be seen in Figure 9.10, where the contact angle for the liquid-fibre interface has been set to 110°.

9.6 Examination of droplet motion

The simulated coalesced droplets on the fibres should move along the fibres in the same way as observed in filtration experiments conducted on mist filters and their fibres. Additionally, when a coalesced droplet begins to move along a fibre it should be due to the flow forces acting on the droplet. In Chapter 6, the force required to move a coalesced liquid droplet has been measured and modelled, which provides a basis for comparison. The forces acting on a coalesced droplet and moving it should be the same (taking into account the relevant measurement and simulation errors).

9.6.1 Approach

During the validation of the implementation of the Plateau-Rayleigh instability, the movement of coalesced droplets along the fibre was observed. Therefore similar cases to those in Section 9.5 will be used. The simulations will commence with the liquid film, as starting with an unloaded fibre will require very long simulation times, and will therefore simulate the break-up of the film and the movement of the resultant droplets on the fibre. By varying the thickness of the liquid film, the size of the droplets can be manipulated. Different velocities can be used to vary the drag forces acting on the droplets. These simulations were run using film thicknesses of 1.5, 1.8 and 2 μm and velocities of 0.1, 0.2 and 0.3 m/s.

The forces acting on the droplets can be determined by extracting the viscous stresses acting on the gas-liquid interface from the simulation. This was performed using a short script which determines the surface normals at the two-phase interface and then evaluates the viscous stresses. These are evaluated over the whole liquid surface and multiplied by the liquid viscosity to determine the force. As this will determine the force acting over the whole interface, the resulting values will need to be divided by the number of droplets. As these droplets have been formed by the break-up of a liquid film by Plateau-Rayleigh instability, they will be of the same size, so the force determined will be accurate.

9.6.2 Results and Discussion

Initial simulations were run, in the same manner as in Section 9.5, using a 2 μm film. During the simulation, the film breaks-up into droplets and the droplets are moved about axially by the flow. After approximately 0.0007 s, the droplets can be seen to move along the fibre. In most simulations a droplet would start moving down the fibre and when it approached a neighbouring droplet, this droplet would move up towards the droplet already in motion. An example of this is shown in Figure 9.12. This is same way droplets were seen to merge during measurements with the AFM and was described in Section 5.3.

In Chapter 6, a theoretical model was introduced which described the force required to move a droplet along a fibre. In this model a term describing the displacement of the mass centre of the droplet away form the centre of the fibre was provided. As this term, r, was increased it was found, both theoretically and experimentally, to decrease the force required to move a droplet. This effect should then be present in the simulated system.

The presence/influence of r in the simulations was examined by varying the flow velocity acting on the system. When there is no flow (i.e. a velocity of 0), r is 0, however as the velocity is increased the value of r also increases.

A droplet that does not drain at a velocity of 0.1 m/s, may drain at a velocity of 0.2 m/s. This is due to the combined effects of increased force acting on the droplet and the effect of r. As when r increases the force required to move the droplet also decreases and therefore drainage can occur; this effect was demonstrated in Chapter 6.

At 0.1 m/s the droplet appears slightly displaced, with a small value of r. The droplet maintains its position on the fibre and eventually drains, or remains in its position. At 0.2 m/s, the value of r is slightly larger and the droplet drains down the fibre much more readily. Hence less force is required

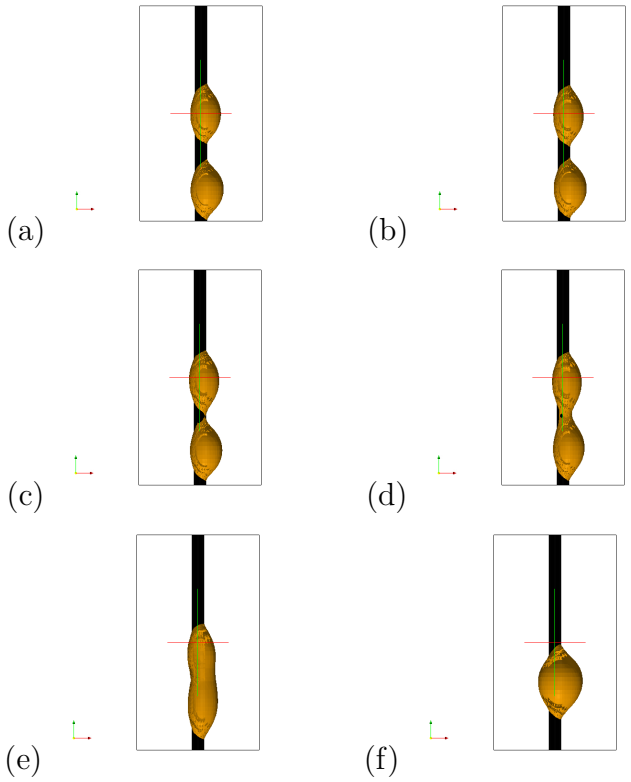

Figure 9.12: A series of images showing the movement of a coalesced droplet down a fibre under the influence of flow, and the merging of this droplet with the droplet immediately below

in order to get the droplet to move. The values of r at different flow velocities are shown in Table 9.3.

The force acting on a droplet in a simulation may be readily compared to the force predicted by the theoretical model. The model is simply evaluated using the dimensions of the simulated droplet, which can be measured from an image of the droplet, rendered during the post-processing of the simulation. The forces acting on the liquid surface, are evaluated at each written timestep, the force required to move a droplet is then the force acting on the droplet at the timestep where it first starts to move down the fibre. Given that the force acting on the liquid interface is the one calculated, this value will need to be divided by the number of droplets present to determine the

Table 9.3: The average value of r at different velocities

u (m/s)	r (μm)
0.1	6.01
0.2	7.37
0.3	9.38

force acting on an individual drop. As the droplets are formed by the break up of the liquid film under Plateau-Rayleigh instability they will be of equal size.

The forces acting on the liquid droplets are shown in Figure 9.13, using the same axes as used in Chapter 6. In this figure the force values predicted by the theoretical model are also provided for comparison.

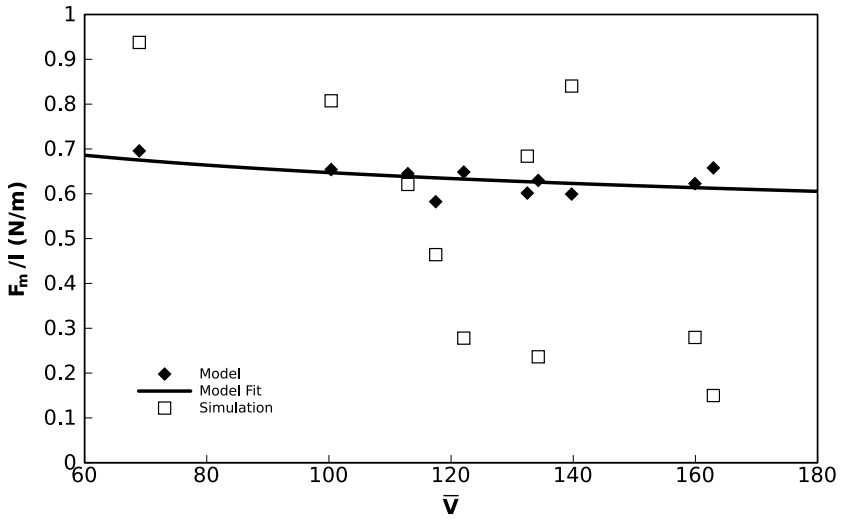

Figure 9.13: Simulated and modelled forces required to move a liquid drop along an oleophillic fibre

The agreement between the modelled and simulated values is not as good as that between the measured and modelled values in Chapter 6. This is expected however, as discretisation and iteration errors may be associated with the simulation. Also, there will be an error associated with the droplet

size, as the droplet image that is measured has a boundary defined by a user input volume fraction.

The simulated droplets then behave in a similar way to the coalesced droplets that were measured in Chapters 6 and 8.

9.7 Solver Testing using Realistic Filter Geometries

It has been demonstrated that the solver in its current form is capable of simulating the mechanisms of droplet capture, liquid coalescence, the break up of liquid films and the movement of coalesced liquid droplets. The final validation test required is that it can resolve all these processes when they are occurring together in a geometry composed of multiple, randomly arranged fibres.

9.7.1 Approach

A realistic filter geometry was prepared using a custom python script, which generates a geometry based on user input fibre diameter and packing density. This geometry was then meshed in the same way as described in Section 9.3. This geometry represents a $2 \times 2 \times 2$ mm cubic section of a fibrous filter. As the geometry is no longer symmetrical, the cyclic boundary conditions are no longer used. The simulation was then run, starting with the clean (unloaded) fibres being exposed to aerosol at a constant mass flow rate. Given the size of the simulation it was necessary to run the simulation in parallel over a number of CPUs.

9.7.2 Results and Discussion

The simulation demonstrates the mechanisms of droplet capture, liquid coalescence, the break up of liquid films and the movement of coalesced liquid droplets, all occurring together within a filter and therefore shows that the solver is appropriate for use in the simulation of fibrous filters. Figure 9.14,

shows evidence of all of the mechanisms in play. There exist smaller axisymmetric droplets which have resulted from liquid film break-up. Larger coalesced droplets which have resulted from the merging and movement of smaller droplets. The collection of particles can be shown to function correctly as not only is there liquid present on the fibres, but all the coalesced droplets are of different sizes, illustrating that the collection of aerosol 'particles' is continually taking place throughout the simulation.

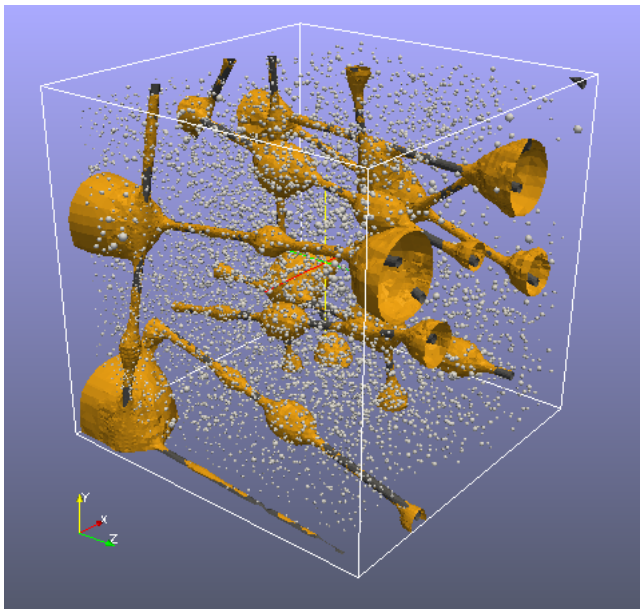

Figure 9.14: Simulation of a small portion of a filter. 'Particles' are being collected and larger coalesced droplets exist, some of which have commenced moving along the fibre(s) (the size of the 'particles' has been exaggerated to aid visibility)

9.8 Conclusion

This Chapter has presented a CFD solver that can be used to simulate the behaviour of droplet-fibre systems, such as those in coalescing filters. The solver has been validated by examining the processes that take place individually, using either a single fibre or a simplified geometry, and then all together. The solver is able to simulate droplet capture, liquid coalescence,

the break-up of liquid films due to Plateau-Rayleigh instability and the movement of coalesced liquid droplets on the fibre.

There is some mesh dependence in relation to the capture of droplets, as illustrated by Figure 9.4. However, this can be controlled by the selection of an appropriate mesh size. Simulation errors must also be considered, as well as the errors with the theory itself, as they are based on semi-empirical expressions.

Overall, the solver has been demonstrated to work well (i.e. it can model the system in a physically realistically manner). The main consideration when it comes to application to 'real world filters' will be the time taken to complete the simulation. As mentioned previously however, this time only needs to be shorter than the time required to test a filter in the laboratory in order for it to be practical. The simulations can also be run over multiple cpus in parallel, which will significantly shorten the calculation time.

10 Conclusions

This work has presented an alternative approach to modelling mist filters; where filters have been studied on a smaller, simpler scale. This approach avoids some of the challenges associated with the complex geometry of fibrous filters and represents a more fundamental approach. Using this approach it has been possible to examine the behaviour of coalesced liquid droplets on fibres. Additionally, it has been shown that fibrous filters may be modelled using capillary theory.

In Chapter 4, a capillary based model was developed to predict the equilibrium saturation of a fibrous filter. It was shown that the predicted saturations agreed well with the measured saturation values, particularly for the glass-fibre filters. This model was however found to be limited to filters with thicknesses of less than 5mm. Provided measurements similar to those in Chapter 4 are conducted it should be possible to determine the correction factor for other filters. This would then mean that the capillary model could be used to determine the saturation of an on-line filter, based on its pressure drop, without the need to remove the filter and weigh it.

Chapter 5, presented the development of a method to determine the force required to move a droplet along a fibre. It was found that it the force could be measured using a specially prepared colloid probe by carefully engaging it on the droplet. It was found that provided an appropriate sphere size is used on the colloidal probe, both axisymmetric and 'clamshell' shaped droplets of different sizes could be measured.

A theoretical model has been presented which can be used to predict the force required to move a liquid droplet along a fibre. This model was initially validated in Chapter 6 and then further validated in Chapter 8, when it was applied to droplets on different fibre materials. These measurements also revealed that the force is influenced by the surface roughness of the fibres. Generally the measured forces agree more closely with the model predicted

forces when the fibre surfaces are smoother.

The model also includes a term, r, designating the distance the droplet's mass centre has been displaced from the axisymmetric rest position on the fibre. This can occur in a filter when a coalesced droplet may be moved by airflow forces. This displacement will reduce the force required to move the droplet and as such higher filtration velocities are likely to result in the droplets draining earlier (at a smaller size).

Measurements were also conducted on oleophobic fibres. These proved more difficult to measure due to the probe-fibre interactions and also the (very) rough fibre surface that resulted from the coating procedure. The measured forces were, however able to be modelled using Bayesian regression models. It was possible to adapt the theoretical model for the 'clamshell' shaped droplets, however this required some assumptions to be made. The agreement between the measured values and the modelled values were relatively close for glycerol, however for motor oil and DEHS a significant discrepancy was found, likely due to the effects of contact line pinning. This work further illustrated the significance of the roughness of the fibre surface.

In general, it was found that the force required to move a liquid droplet, was greater for droplets on oleophillic fibres than droplets on oleophobic fibres. However, given the effect of surface roughness, this difference may or may not be significant. This suggests that the improved drainage properties predicted for oleophobic filters may not be fully realised unless smooth oleophobic fibres can be obtained.

The CFD solver presented has been shown to conform to physical reality. It can simulate the break-up of liquid films, and the movement of coalesced droplets. The droplet/particle capture code (discrete particle tracking) could be improved, however, as shown, if an appropriate mesh size is used, the underprediction of the capture of particles by interception can be eliminated. There remains a slight issue with over prediction of capture of small parti-

cles subject to Brownian motion, though given the relative masses of such droplets, any effects on overall mass-based simulation results will be negligible.

In conclusion, this work has presented a capillary-based model to allow the prediction of the equilibrium saturation of a filter, thereby presenting an alternative to existing empirically derived models. It has also detailed the development of a method to measure the force required to move a droplet along a fibre and presented the results of those measurements. This resulted in both a validated theoretical model and a simple relationship which can be used to determine the force required to move a liquid droplet based on a reduced volume. This work has also presented a CFD solver which can be used to run simulations on mist filters, thus presenting an alternative to whole scale filter testing.

References

Adamson, A. and Gast, A. (1997) Physical Chemistry of Surfaces John Wiley & Sons, New York, USA 6th edition

Agranovski, I. and Braddock, R. (1998a) *Filtration of Liquid Aerosols on Nonwettable Fibrous Filters* AIChE Journal **44**(12) pp. 2784–2790

Agranovski, I. and Braddock, R. (1998b) *Filtration of Liquid Aerosols on Wettable Fibrous Filters* AIChE Journal **44**(12) pp. 2775–2783

Agranovski, I., Myojo, T., Braddock, R., and Jarvis, D. (2001) *Combined Wettable/Nonwettable Filter for Mist Purification* Chemical Engineering & Technology **24** pp. 287–292

Agranovski, I., R.D., B., Jarvis, D., and Myojo, T. (2002) *Inclined Wettable Filter for Mist Purification* Chemical Engineering Journal **89** pp. 229–238

Agranovski, I. and Shapiro, M. (2001) *Clogging of Wet Filters by Dust Particle* Journal of Aerosol Science **32** pp. 1009–1020

Agranovski, I. and Whitcombe, J. (2000) *Utilisation of wet fibrous media for filtration of sticky aerosol particles* Journal of Aerosol Science **31**((Supplement 1)) p. S204

Agranovski, I. and Whitcombe, J. (2001) *Case Study on the Practical Use of Wettable Filters in the Removal of Sub-Micron Particles* Chemical Engineering /& Technology **24**(5) pp. 513–517

Bacri, J., Frenois, C., Perzynshi, R., and Salin, D. (1988) *Magnetic Drop-Sheath Wetting Transition of a Ferrofluid on a Wire* Revue De Physique Applique **23**(6) pp. 1017–1022

Bauer, C. and Dietrich, S. (2000) *Shapes, contact angles and lin tensions of droplets on cylinders* Physical Review E **62**(2) pp. 2428–2438

Benzi, M. (2002) *Preconditioning Techniques for Large Linear Systems: A Survey* Journal of Computational Physics **182**(2) pp. 417–477

Berberovic, E., van Hinsberg, N., Jakirlic, S., Roisman, I., and Tropea, C. (2009) *Drop impacr onto a liquid layer of finite thickness: Dynamics of cavity evolution* Physical Review E **79**(3) pp. 036306–1–036306–15

Berry, D., Ikegami, M., and Jobe, B. (1989) *Lung Perfusion and Aerosol Distributions in Preterm Ventilated Lambs* Pediatric Pulmonology **6**(3) pp. 147–152

Best, N., Cowles, M., and Vines, S. (1995) *CODA: Convergence diagnosis and output analysis software for Gibbs sampling output, Version 0.3*

Bhushan, B., Israelachvili, J., and Landman, U. (1995) *Nanotribology: friction, wear and lubrication at the atomic scale* Nature **374**(6523) pp. 607–616

Binnig, G., Quate, D., and Gerber, C. (1986) *Atomic Force Microscopy* Physical Review Letters **56**(9) pp. 930–933

Binnig, G., Rohrer, H., Gerber, C., and Weibel, E. (1981) *Tunneling through a controllable vacuum gap* Applied Physics Letters **40**(2) pp. 178–180

Bird, R., Stewart, W., and Lightfoot, E. (2007) Transport Phenomena John WIley & Sons, New York, USA second edition

Bredin, A., Larcher, A., and Mullins, B. J. (2011) *Thermogravimetric analysis of carbon black and engine-soot - Towards a more robust oil analysis method* Tribology International **44**(12) pp. 1642–1650

Brochard, F. (1986) *Spreading of liquid drops on thin cylinders: The "manchon/droplet" transition* The Journal of Chemical Physics **84**(8) pp. 4664–4672

Brown, R. (1993) Air Filtration: An Integrated Approach to the Theory and Applications of Fibrous Filters Pergamon Press, Oxford

Cannara, R., Eglin, M., and Carpick, R. (2006) *Lateral force calibration in atomic force microscopy: A new lateral force calibration method and*

general guidelines for optimization Review of Scientific Instruments **77** pp. 053701–1–053701–11

Carroll, B. J. (1976) *The accurate measurement of contact angle, phase contact areas, drop volume, and Laplace excess pressure in drop-on-fiber systems* Journal of Colloid and Interface Science **57**(3) pp. 488 – 495

Carroll, B. J. (1984) *The equilibrium of liquid drops on smooth and rough circular cylinders* Journal of Colloid and Interface Science **97**(1) pp. 195 – 200

Carroll, B. J. (1986) *Equilibrium Conformations of liquid Drops on Thin Cylinders under forces of Capillarity. A Theory for the Roll-up Process* Langmuir **2** pp. 248–250

Chapman, A., Saad, Y., and Wigton, L. (2000) *High-order ILU preconditioners for CFD problems* International Journal for Numerical Methods in Fluids **33**(6) pp. 767–788

Charvet, A., Gonthier, Y., Bernis, A., and Gonze, E. (2008) *Filtration of liquid aerosols with a horizontal fibrous filter* Chemical Engineering Research and Design **86**(6) pp. 569–576

Charvet, A., Gonthier, Y., Gonze, E., and Bernis, A. (2010) *Experimental and modelled efficiencies during the filtration of a liquid aerosol with a fibrous media* Chemical Engineering Science **65**(5) pp. 1875–1886

Chen, C. Y. (1955) *Filtration of Aerosols by Fibrous Media* Chemical Reviews **55**(3) pp. 595–623

Chen, X.-Q. and Pereira, J. (1999) *A new particle-locating method accounting for source distribution and particle-field interpolation for hybrid modeling of strongly coupled two-phase flows in arbitrary coordinates* Numerical Heat Transfer, Part B **35**(1) pp. 41–63

Cheng, Y., Yamada, Y., and Yeh, H. (1990) *Diffusion Deposition on Model Fibrous Filters with Intermediate Porosity* Aerosol Science and Technology **12**(2) pp. 286–299

Cheng, Y. and Yeh, H. (1980) *Theory of a screen-type diffusion battery* Journal of Aerosol Science **11**(3) pp. 313–320

Chorda, R., Blasco, J., and Fueyo, N. (2002) *An efficient particle-locating algorithm for application in arbitrary 2D and 3D grids* International Journal of Multiphase Flow **28**(x) pp. 1565–1580

Cleveland, J., Manne, S., and Bocek, D.and Hansma, P. (1993) *A nondestructive method for determining the spring constant of cantilevers for scanning force microscopy* Review of Scientific Instruments **64** pp. 403–405

Contal, P., Simao, J., Thomas, D., Frising, T., Callé, S., Appert-Collin, J. C., and Bémer, D. (2004) *Clogging of fibre filters by submicron droplets. Phenomena and influence of operating conditions* Journal of Aerosol Science **35**(2) pp. 263 – 278

Cooper, S. and Leith, D. (1998) *Evaporation of Metalworking Fluid Mist in Laboratory and Industrial Mist Collectors* American Industrial Hygiene Association Journal **59**(1) pp. 45–51

Courant, R., Friedrichs, K., and Lewy, H. (1928) *Über die partillen differenzengleichungen der mathematischen physik* Mathematische Annalen **100**(1) pp. 32–74

Cumpson, P., Hedley, J., and Clifford, C. (2005) *Microelectromechanical device for lateral force calibration in the atomic force microscope: Lateral electrical nanobalance* Journal of Vacuum Science & Technology B **23**(5) pp. 1992–1997

Davies, C. (1952) *The Separation of Airborne Dust Particles* Proceedings of the Institute of Mechanical Engineers B **1**(-) pp. 185–198

Davies, C. (1973) Air Filtration Academic Press, London

Dawar, S. and Chase, G. (2008) *Drag correlation for axial motion of drops on fibers* Separation and Purification Technology **66**(-) pp. 6–13

deGennes (1985) *Wetting: statics and dynamics* Reviews of Modern Physics **57**(3) pp. 827–863

Derjaguin, B. and Churaev, N. (1974) *Structural Component of Disjoining Pressure* Journal of Colloid and Interface Science **49**(2) pp. 249–255

Feiler, A. ad Attard, P. and Larson, I. (2000) *Calibration of the torsional spring constant and the lateral photodiode response of frictional force microscopes* Review of Scientific Instruments **71**(7) pp. 2746–2750

Ferziger, J. and Peric, M. (2002) Computational Methods for Fluid Dynamics Springer-Verlag, Berlin, Germany third edition

Fotovati, S., Tafreshi, H., and Pourdeyhimi, B. (2010) *Influence of fiber orientation distribution on performance of aerosol filtration media* Chemical Engineering Science **65**(18) pp. 5285–5293

Frising, T., Gujisait, V., Thomas, D., Call, S., Bmer, D., Contal, P., and Leclerc, D. (2004) *Filtration of solid and liquid aerosol mixtures: Pressure drop evolution ans influence of solid/liquid ratio* Filtration & Separation **41**(2) pp. 36 – 36

Frising, T., Thomas, D., Bmer, D., and Contal, P. (2005) *Clogging of fibrous filters by liquid aerosol particles: Experimental and phenomenological modelling study* Chemical Engineering Science **60**(10) pp. 2751 – 2762

Gelman, A., Carlin, J., Stern, H., and Rubin, D. (2004) Bayesian Data Analysis Chapman & Hall/CRC, Florida, USA second edition

Gougeon, R., Boulaud, D., and Renoux, A. (1994) *15.P.01 Theoretical and experimental study of fibrous filters loading with liquid aerosols in the inertial regime* Journal of Aerosol Science **25**(Supplement 1) pp. 189 – 190

Green, C., Lioe, H., Cleveland, J., Proksch, R., Mulvaney, P., and Sader, J. (2004) *Normal and torsional spring constants of atomic force microscope cantilevers* Review of Scientific Instruments **75**(6) pp. 1988–1996

Green, C. and Sader, J. (2002) *Torsional frequency response of cantilever beams immersed in viscous fluids with applications to the atomic force microscope* Journal of Applied Physics **92**(10) pp. 6262–6274

Gunter, K. L. and Sutherland, J. W. (1999) *An experimental investigation into the effect of process conditions on the mass concentration of cutting fluid mist in turning* Journal of Cleaner Production **7**(5) pp. 341–350

Haider, A. and Levenspiel, O. (1989) *Drag Coefficient and Terminal Velocity of Spherical and Nonspherical Particles* Powder Technology **58**(1) pp. 63–70

Hansma, P., Elings, V., Marti, O., and Bracker, C. (1988) *Scanning Tunneling Microscopy and Atomic Force Microscopy: Application to Biology and Technology* Science **242**(4876)

Happel, J. (1959) *Viscous Flow Relative to Arrays of Cylinders* AIChE Journal **5**(2) pp. 174–177

Herminghaus, S., Pompe, T., and Fery, A. (2000) *Scanning force microscopy investigation of liquid structures and its applicationto fundamental wetting research* Journal of Adhesion Science and Technology **14**(4) pp. 1767–1782

Hinds, W. (1999) Aerosol Technology - Properties, Behaviour and Measurement of Airborne Partices John Wiley & Sons, New York second edition

Hirt, C. and Nichols, B. (1981) *Volume of Fluid (VOF) Method for the Dynamics of Free Boundaries* Journal of Computational Physics **39**(1) pp. 201–225

Hosseini, S. and Tafreshi, H. (2010) *Modeling particle filtration in disordered 2-D domains: A comparison with cell model* Separation and Purification Technology **74**(2) pp. 160–169

Hutten, I. (2007) Handbook of Nonwoven Filter Media Butterworth-Heinemann, Oxford first edition

Hyvaluoma, J, ., Raiskinmaki P, ., Jasberg A, ., Koponen A, ., Kataja M, ., and Timonen J, . (2006) *Simulation of liquid penetration in paper* Physical Review E **73**(-) pp. 1–8

Issa, R. (1986) *Solution of the Implicitly Discretised Fluid Flow Equations by Operator-Splitting* Journal of Computational Physics **62**(1) pp. 40–65

Jaganathan, S., Tafreshi, H., and Pourdeyhimi, B. (2008a) *On the pressure drop prediction of filter media composed of fibers with bimodl diameter distributions* Powder Technology **181**(1) pp. 89–95

Jaganathan, S., Tafreshi, H., and Pourdeyhimi, B. (2008b) *A realistic approach for modeling permeability of fibrous media: 3-D imaging coupled with CFD simulation* Chemical Engineering Science **63**(1) pp. 244–252

Jaganathan, S., Tafreshi, H., and Pourdeyhimi, B. (2009) *A realistic modeling of fluid infiltration in thin fibrous sheets* Journal of Applied Physics **105**(11) p. 8

Jagdheesh, R., Pathiraj, B., Karatay, E., Romer, G., and Huis in't Veld, A. (2011) *Laser-Induced Nanoscale Superhydrophobic Structures on Metal Surfaces* Langmuir **27** pp. 8464–8469

Khan, A., Philip, J., and Hess, P. (2004) *Young's modulus of silicon nitride used in scanning force microscope cantilevers* Journal of Applied Physics **95**(4) pp. 1667–1672

King, A. and Mullins, B. J. (2011) *A New Computational Fluid Dynamics Solver to Simulate Capture, Coalesecnce and Drainage in Coalescing Filter Media* American Filtration and Separations Society, 24th Annual Conference, Louisville, USA

King, A., Mullins, B. J., and Lowe, A. (2010) *Discrete particle tracing in fluid flows for particulate filter simulations* 6th Australasin Congress on Applied Mechanics, Perth, Australia

Kuwabara, S. (1959) *The Forces Experienced by Randomly Distributed Parallel Circular Cylinders or Spheres in a Viscous Flow at Small Reynolds Numbers* Journal of the Physical Society of Japan **14**(4) pp. 527–532

Lamb, H. (1932) Hydrodynamics Cambridge University Press, Cambridge, UK

Lee, H. and Owens, J. (2011) *Motion of liquid droplets on a superhydrophobic oleophobic surface* Journal of Material Science **46** pp. 69–76

Lee, H., Willis, C., and Stone, C. (2011) *Modeling and preparation of a superoleophobic non-woven fabric* Journal of Material Science **46** pp. 3907–3913

Lee, K. W. and Liu, B. Y. H. (1981) *Experimental Study of Aerosol Filtration by Fibrous Filters* Aerosol Science and Technology **1**(1) pp. 35 – 46

Lee, K. W. and Liu, B. Y. H. (1982) *Theoretical Study of Aerosol Filtration by Fibrous Filters* Aerosol Science and Technology **1**(2) pp. 147 – 161

Lehmann, M. and Kasper, G. (2002) *CFD Simulations of Single Fiber Particle Loading* Particle Loading and Kinetics of Filtration in Fibrous Filters, International Workshop, Karlsruhe, Germany

Lehmann, M. J., Hardy, E. H., Meyer, J., and Kasper, G. (2005) *MRI as a key tool for understanding and modeling the filtration kinetics of fibrous media* Magnetic Resonance Imaging **23**(2) pp. 341 – 342 proceedings of the Seventh International Conference on Recent Advances in MR Applications to Porous Media

Leite, F. and Herrmann, P. (2005) *Application of atomic force spectroscopy (AFS) to studies of adhesion phenomena: a review* in Drelich, J. and Mittal, K. (Editors), Atomic Force Microscopy in Adhesion Studies pp. 3–43 VSP, Boston

Letts, G. M., Raynor, P. C., and Schumann, R. L. (2003) *Selecting fiber materials to improve mist filters* Journal of Aerosol Science **34**(11) pp. 1481 – 1492

Li, B., Ji, Z., and Yang, X. (2009) *Evaluation of gas-liquid separation performance of natural gas filters* Petroleum Science **6**(4) pp. 438–444

Liew, T. and Conder, J. (1985) *Fine mist filtration by wet filters–I. Liquid saturation and flow resistance of fibrous filters* Journal of Aerosol Science **16**(6) pp. 497 – 509

Liu, B. Y. H. and Rubow, K. (1990) *Effficiency, pressure drop and figure of merit of high efficiency fibrous and membrane filter media* Fifth World Filtration Congress, Nice, France

Liu, E., Blanpain, B., and Celis, J. (1996) *Calibration procedures for frictional measurements with a lateral force microscope* Wear **192**(1-2) pp. 141–150

Macpherson, G., Nordin, N., and Weller, H. (2009) *Particle tracking in unstructured, arbitrary polyhedral meshes for use in CFD and molecular dynamics* Communications in Numerical Methods in Engineering **25**(3) pp. 263–273

Manne, S., Hansma, P., Massie, J., Elings, V., and Gewirth, A. (1991) *Atomic-Resolution Electrochemistry with the Atomic Force Microscope: Copper Deposition on Gold* Science **251**(4990) pp. 183–186

Marmur, A. (2004) *The Lotus Effect: Superhydrophobicity and Metastability* Langmuir **20** pp. 3517–3519

Marmur, A. and Cohen, R. (1997) *Characterization of porous media by the kinetics of liquid penetration: The vertical capillaries model* Journal of Colloid and Interface Science **189**(2) pp. 299–304

Marti, O., Drake, B., and Hansma, P. (1987) *Atomic force microscopy of liquid-covered surfaces: Atomic resolution images* Applied Physics Letters **51**(7) pp. 484–486

McHale, G., Kb, N. A., Newton, M. I., and Rowan, S. M. (1997) *Wetting of a High-Energy Fiber Surface* Journal of Colloid and Interface Science **186**(2) pp. 453–461

McHale, G., Newton, M., and Carroll, B. J. (2001) *The Shape and Stability of Small Liquid Drops on Fibers* Oil & Gas Science and Technology **56**(1) pp. 47–54

McHale, G. and Newton, M. I. (2002) *Global geometry and the equilibrium shapes of liquid drops on fibers* Colloids and Surfaces A: Physicochemical and Engineering Aspects **206**(1-3) pp. 79 – 86

Meijerink, J. and van der Vorst, H. (1977) *An Iterative Solution Method for Linear Systems of Which the Coefficient Matrix is a Symmetric M-Matrix* Mathematics of Computation **31**(137) pp. 148–162

Meurk, A., Larson, I., and Bergstrom, L. (1998) *Tribological Properties of Iron Powder Subjected to Various Surface Treatments* in Materials Research Society Symposium Proceedings volume 522

Meyer, G. and Amer, N. (1988) *Novel optical approach to atomic force microscopy* Applied Physics Letters **53**(12) pp. 1045–1047

Mullins, B. J., Agranovski, I. E., and Braddock, R. D. (2004) *Simultaneous capture of two types of aerosol (water/oil and solid/water) on fibrous filters* Journal of Aerosol Science **35**(Supplement 2) pp. 1239–1240

Mullins, B. J. and Braddock, R. D. (2011) *Capillary Rise in Porous, Fibrous Media During Liquid Immersion* International Journal of Heat and Mass Transfer **Submitted**

Mullins, B. J., Braddock, R. D., and Agranovski, I. E. (2003) *Fibre Wetting Processes in Wet Filtration* in MODSIM Townsville

Mullins, B. J., Braddock, R. D., Agranovski, I. E., and Cropp, R. A. (2006) *Observation and modelling of barrel droplets on vertical fibres subjected to gravitational and drag forces* Journal of Colloid and Interface Science **300**(2) pp. 704 – 712

Mullins, B. J., Braddock, R. D., Agranovski, I. E., Cropp, R. A., and O'Leary, R. A. (2005) *Observation and modelling of clamshell droplets on vertical*

fibres subjected to gravitational and drag forces Journal of Colloid and Interface Science **284**(1) pp. 245 – 254

Mullins, B. J., Braddock, R. D., and Kasper, G. (2007a) *Capillarity in fibrous filter media: Relationship to filter properties* Chemical Engineering Science **62**(22) pp. 6191 – 6198

Mullins, B. J. and Kasper, G. (2006) *Comment on: Clogging of fibrous filters by liquid aerosol particles: Experimental and phenomenological modelling study by Frising et al.* Chemical Engineering Science **61**(18) pp. 6223 – 6227

Mullins, B. J., Pfrang, A., Braddock, R. D., Schimmel, T., and Kasper, G. (2007b) *Detachment of liquid droplets from fibres–Experimental and theoretical evaluation of detachment force due to interfacial tension effects* Journal of Colloid and Interface Science **312**(2) pp. 333 – 340

Neumeister, J. and Ducker, W. (1994) *Lateral, normal, and longitudinal spring constants of atomic force microscopy cantilevers* Review of Scientific Instruments **65**(8) pp. 2527–2531

Niemark, A. (1999) *Thermodynamic equilibrium and stability of liquid films and droplets on fibers* Journal of Adhesion Science and Technology **13**(10) pp. 1137–1154

Ogletree, D., Carpick, R., and Salmeron, M. (1996) *Calibration of frictional forces in atomic force microscopy* Review of Scientific Instruments **67**(9) pp. 3298–3306

Ohnesorge, F. and Binnig, G. (1993) *True Atomic Resolution by Atomic Force Microscopy Through Repulsive and Attractive Forces* Science **260** pp. 1451–1456

Ounis, H., Ahmadi, G., and McLaughlin (1990) *Brownian Diffusion of Submicrometer Particles in the Viscous Sublayer* Journal of Colloid and Interface Science **143**(1) pp. 266–277

Palacio, M. and Bhushan, B. (2010) *Normal and Lateral Force Calibration Techniques for AFM Cantilevers* Critical Reviews in Solid State and Materials Sciences **35** pp. 73–104

Patankar, S. and Spalding, D. (1972) *A calculation procedure for heat, mass and momentum transfer in three-dimensional parabolic flows* International Journal of Heat and Mass Transfer **15**(10) pp. 1787–1806

Payet, S. (1991) Filtration stationnaire et dynamique des aerosols liquides submicroniques Ph.D. thesis Universite Paris XII

Payet, S., Boulaud, D., Madelaine, G., and Renoux, A. (1992) *Penetration and pressure drop of a HEPA filter during loading with submicron liquid particles* Journal of Aerosol Science **23**(7) pp. 723 – 735

Plateau, J. (1873) Statique experimentale et theorique des liquids soumis aux seules forces moleculaire volume 2 Gauthiers-Villars, Paris

Pohanish, R. (Editor) (2002) Sittig's Handbook of Toxic and Hazardous Substances and Carcinogens volume 2 William Andrew Publishing, Norwich, New York, USA fourth edition

Qian, F., Zhang, J., and Huang, Z. (2009) *Effects of the Operating Conditions and Geometry Parameter on the Fibrous Filter* Chemical Engineering Technology **32**(5) pp. 789–797

Quere, D. (1999) *Fluid Coating on a Fiber* Annual Review of Fluid Mechanics **31**(-) pp. 347–384

Quere, D., Di Meglio, J.-M., and Brochard-Wyart, F. (1988) *Wetting of fibers: theory and experiments* Revue De Physique Applique **23**(-) pp. 1023–1030

Rayleigh, L. (1892) *On the Instability of a Cylinder of Viscous Liquid under Capillary Force* Philosophical Magazine **34**(207) pp. 145–154

Raynor, P. C. and Leith, D. (2000) *The Influence of Accumulated Liquid on Fibrous Filter Performance* Journal of Aerosol Science **31**(1) pp. 19 – 34

Rebouillat, S., Letellier, B., and Steffenino, B. (1999) *Wettability of single fibres - beyond the contact angle approach* International Journal of Adhesion & Adhesives **19** pp. 303–314

Roe, R.-J. (1975) *Wetting of fine wires and fibers by a liquid film* Journal of Colloid and Interface Science **50**(1) pp. 70 – 79

Ryu, J., Choi, J., Hahn, B., Park, D., Yoon, W., and Kim, K. (2007) *Fabrication and ferroelectric properties of highly dense lead-free piezoelectric* $(K_{0.5}Na_{0.5})NbO_3$ *thick films by aerosol deposition* Applied Physics Letters **90** pp. 152901–1–152901–3

Sader, J. (1995) *Parallel beam approximation for V-shaped atomic force microscope cantilevers* Review of Scientific Instruments **66**(9) pp. 4583–4587

Sader, J., Chon, J., and Mulvaney, P. (1999) *Calibration of rectangular atomic force microscope cantilevers* Review of Scientific Instruments **70**(10) pp. 3967–3969

Semal, S., Blake, T., Geskin, V., de Ruijter, M., Castelein, G., and De Connick, J. (1999) *Influence of Surface Roughness on Wetting Dynamics* Langmuir **15** pp. 8756–8770

Seveno, D., Valiant, A., Rioboo, R., Adao, H., Conti, J., and De Connick, J. (2009) *Dynamics of Wetting Revisited* Langmuir **25** pp. 13034–13044

Sheehan, P. and Lieber, C. (1996) *Nanotribology and Nanofabrication of MoO3 Structures by Atomic Force Microscopy* Science **272**(5265) pp. 1158–1161

Stechkina, I. B. (1966) *Diffusion precipitation of aerosols in fibre filters* Doklady Academii Nauk SSSR **167** p. 1329

Stechkina, I. B., Kirsch, A. A., and Fuchs, A. (1969) *Studies on Fibrous Aerosol Filters - IV Calculation of Aerosol Deposition in Model Filters in the Range of Maximum Penetration* Annals of Occupational Hygiene **12**(-) pp. 1–8

Sutherland, K. (2008) Filters and Filtration Handbook Butterworth-Heinemann, Oxford fifth edition

Tafreshi, H., Rahman, M., Jaganathan, S., Wang, Q., and Pourdeyhimi, B. (2009) *Analytical expressions for predicting permeability of bimodal fibrous porous media* Chemical Engineering Science **64**(6) pp. 1154–1159

Thornburg, J. and Leith, D. (2000) *Size Distribution of Mist Generated During Metal Machining* Applied Occupational and Environmental Hygiene **15**(8) pp. 618 – 628

Versteeg, H. and Malalasekera, W. (2007) An Intoduction to Computational Fluid Dynamics The Finite Volume Method Pearson Prentice Hall, Essex, UK second edition

Vila, M., Caceres, D., and Prieto, C. (2003) *Mechanical properties of sputtered silicon nitride thin films* Journal of Applied Physics **94**(12) pp. 7868–7873

Wagner, H. (1990) *Spreading of liquid droplets on cylindrical surfaces: Accurate determination of contact angle* Journal of Applied Physics **67**(3) pp. 1352–1355

White, C. (1946) *The Drag of Cylinders in Fluids at Slow Speeds* Proceedings of the Royal Society of London A **186** pp. 472–479

Wickramasinghe, H. K. (2000) *Progress in scanning probe microscopy* Acta Materialia **48**(1) pp. 347 – 358

Yamaki, J.-I. and Katayama, Y. (1975) *New Method of Determining Contact Angle between Monofilament and Liquid* Journal of Applied Polymer Science **19** pp. 2897–2909

Yarin, A. and Oron, A. (1993) *Capillary instability of thin liquid film on a cylinder* The Physics of Fluids A **5**(1) pp. 91–98

Yeh, H.-C. and Liu, B. Y. H. (1974) *Aerosol filtration by fibrous filters–II. experimental* Journal of Aerosol Science **5**(2) pp. 205–217

Yuan, Y. and Lenhoff, A. M. (2003) *Measurement of mobility of adsorbed colloids by lateral force microscopy* Journal of Colloid and Interface Science **267**(2) pp. 352 – 359

Zhong, Q., Inniss, D., Kjoller, K., and Elings, V. (1993) *Fractured polymer/silica fiber surface studied by tapping mode atomic force microscopy* Surface Science **290**(1-2) pp. L688 – L692

Zhou, Q. and Leschziner, M. (1999) *An imporved particle-locating algorithm for Eulerian-Lagrangian computations of two-phase flows in general coordinates* International Journal of Multiphase Flow **25**(5) pp. 813–825

Every reasonable effort has been made to acknowledge the owners of copyright material. I would be pleased to hear from any copyright owner who has been omitted or incorrectly acknowledged.

Appendix A

A field setting utility dictionary file, defining a liquid column is shown below. The liquid column is implemented around the fibre, thereby creating a film with a 5 μm thickness.

```
/*--------------------------------*- C++ -*----------------------------------*\
| =========                 |                                                 |
| \\      /  F ield         | OpenFOAM: The Open Source CFD Toolbox           |
|  \\    /   O peration     | Version:  1.7.1                                 |
|   \\  /    A nd           | Web:      www.OpenFOAM.com                      |
|    \\/     M anipulation  |                                                 |
\*---------------------------------------------------------------------------*/
FoamFile
{
    version     2.0;
    format      ascii;
    class       dictionary;
    location    "system";
    object      funkySetFields;
}
// * * * * * * * * * * * * * * * * * * * * * * * * * * * * * * * * * * * * * //

expressions
 (
      column
      {
            field alpha1;
            expression "1";
            condition "pow(pos().x-0,2) + pow(pos().y-0,2) < pow(10e-6,2)";
        }
      columnVel
      {
            field U;
            expression "vector (0,0,0)";
            condition "pow(pos().x-0,2) + pow(pos().y-0,2) < pow(10e-6,2)";
      }

 );




// ************************************************************************* //
```

Appendix B

An excerpt from the *alpha1* file showing the parameters used for the boundary field on the fibre is shown below.

```
fibre
    {
        type            dynamicAlphaContactAngle;
         theta0          18;
         uTheta          1;
         thetaA          60;
         thetaR          5;
//         limit          none;
//         limit          alpha;
         limit           gradient;
//         limit          zeroGradient;
        value           uniform 0;
    }
```